



HAL
open science

Emulation of PGCM calculations using the Eigenvector continuation method

Antoine Roux

► **To cite this version:**

Antoine Roux. Emulation of PGCM calculations using the Eigenvector continuation method. Nuclear Theory [nucl-th]. Université Paris-Saclay, 2024. English. NNT: 2024UPASP114 . tel-04815246

HAL Id: tel-04815246

<https://theses.hal.science/tel-04815246v1>

Submitted on 2 Dec 2024

HAL is a multi-disciplinary open access archive for the deposit and dissemination of scientific research documents, whether they are published or not. The documents may come from teaching and research institutions in France or abroad, or from public or private research centers.

L'archive ouverte pluridisciplinaire **HAL**, est destinée au dépôt et à la diffusion de documents scientifiques de niveau recherche, publiés ou non, émanant des établissements d'enseignement et de recherche français ou étrangers, des laboratoires publics ou privés.

Emulation of PGCM calculations using the eigenvector continuation method

*Émulation de calculs PGCM avec la méthode
Eigenvector continuation*

Thèse de doctorat de l'université Paris-Saclay

École doctorale n° 576, Particules, Hadrons, Énergie, Noyau,
Instrumentation, Imagerie, Cosmos et Simulation, PHENIICS
Spécialité de doctorat : Physique nucléaire
Graduate school : Physique
Réfèrent : Faculté des sciences d'Orsay

Thèse préparée dans l'unité de recherche **Laboratoire Matière sous Conditions
Extrêmes (Université Paris-Saclay, CEA)**,
sous la direction de **Thomas DUGUET**, Ingénieur de recherche, Professeur,
le co-encadrement de **Jean-Paul EBRAN**, Ingénieur de recherche,
le co-encadrement de **Vittorio SOMÀ**, Ingénieur de recherche,
et le co-encadrement de **Mikael FROSINI**, Ingénieur de recherche

Thèse soutenue à Paris-Saclay, le 15 Octobre 2024, par

Antoine ROUX

Composition du jury

Membres du jury avec voix délibérative

Elias KHAN
Professeur, Université Paris-Saclay
Luís ROBLEDO
Professeur, Universidad Autónoma de Madrid
Michael BENDER
Directeur de recherche, CNRS, IP2I, Lyon
Alessandro PASTORE
Chargé de recherche, CEA Cadarache
Nadezda SMIRNOVA
Professeure, Université de Bordeaux

Président du jury
Rapporteur & Examineur
Rapporteur & Examineur
Examineur
Examinatrice

Titre : Émulation de calculs PGCM avec la méthode Eigenvector Continuation

Mots clés : Structure nucléaire théorique, techniques à N corps, Eigenvector Continuation, émulateurs

Résumé : Le noyau atomique, système quantique de nucléons en interaction, constitue un problème difficile à résoudre exactement. Pour contourner cette difficulté, des méthodes de résolution approchées ont été introduites, comme la Projected Generator Coordinate Method (PGCM). La force de la PGCM est de construire un espace de faible dimension, motivé par des considérations physiques, dans lequel trouver une solution approchée est facile. Cependant, le coût numérique du calcul d'un espace PGCM rend cette méthode mal adaptée pour une étude statistique de sensibilité des observables nucléaires vis-à-vis des paramètres du modèle d'interaction, laquelle nécessite un grand nombre de calculs PGCM. Afin de rendre ce type d'études possibles, cette thèse explore la notion d'émulateur PGCM. Dans ce travail, une combinaison de PGCM avec la méthode Eigenvector Continuation (EC) est construite et étudiée. Cette combinaison (l'émulateur PGCM-EC) tire parti des ressemblances formelles entre PGCM et EC, et sur-

tout de la possibilité de décomposer l'hamiltonien comme combinaison linéaire de termes indépendants des paramètres du modèle d'interaction. Cette dernière propriété permet de concentrer la plus grande partie du coût numérique sur le calcul de quantités indépendantes des paramètres de l'interaction (les kernels élémentaires), et ainsi rend possible l'émulation massive de calculs PGCM, au prix d'avoir en amont effectué le calcul très lourd des kernels élémentaires. Les limites de cet émulateur sont aussi étudiées, en introduisant notamment la notion de sur-entraînement, qui provient précisément du fait que la PGCM est une méthode non-exacte de résolution du problème à N-corps nucléaire. Cette thèse démontre au final qu'il est possible d'émuler des millions de calculs PGCM avec une erreur ne dépassant pas 3% sur la spectroscopie collective des noyaux, et avec un faible coût numérique représentant une fraction de 1% du coût des millions de calculs PGCM.

Title : Emulation of PGCM calculations using the eigenvector continuation method

Keywords : Theoretical nuclear structure, many-body methods, Eigenvector Continuation, emulators

Abstract : An atomic nucleus is a quantum system of interacting nucleons and constitutes a problem difficult to solve exactly. For this reason, a diversity of approximate resolution methods has been designed, and Projected Generator Coordinate Method (PGCM) is one of them. The strong point of PGCM is to construct a physically inspired small dimensional space, in which an approximate solution of the nuclear many-body problem is easily found. However the numerical cost of PGCM space computation make this method inadapted for sensibility analysis of nuclear observables with respect to parametrisation of the interaction model, this analysis requiring an huge number of PGCM computations. In order to make this type of study possible, this thesis explore the concept of PGCM emulator. In this work, a combination of PGCM with Eigenvector Continuation (EC) is constructed and studied. This combination (the

PGCM-EC emulator) takes advantage of mathematical similarities between PGCM and EC, and above all of the decomposition of the hamiltonian as a linear combination of parameter-independent terms. The latter property is used to concentrate the heavier numerical cost in the computation of parameter-independent quantities (the elementary kernels), and open the feasibility of massive PGCM emulations, the price being having first-handedly computed the costly elementary kernels. Limits of the emulator are also explored, by introducing the concept of over-training, which is exactly a consequence of the aproximateness of a PGCM computation. Eventually this thesis demonstrates the possibility to emulate millions of PGCM computations with an error on collective spectroscopy less than 3%, and with a low numerical cost fraction of 1% of the million PGCM calculations cost.

Synthèse

Le domaine de la structure nucléaire théorique s'occupe de modéliser les noyaux atomiques de façon à pouvoir calculer leurs propriétés mesurables. Le cadre théorique général pour une telle étude est la mécanique quantique à plusieurs corps (approche dites de seconde quantification). Afin d'avoir une description cohérente et prédictive des noyaux, l'approche dite ab-initio vise à décrire de façon unifiée et systématiquement améliorable les noyaux atomiques. Dans cette approche, l'interaction repose actuellement sur un modèle du type Théorie Effective des Champs Chirale (Chiral EFT) reposant sur la Chromodynamique Quantique (QCD). L'interaction forte au sein des noyau régie par la QCD dont les degré de liberté fondamentaux sont les quarks et les gluons est remplacée par une théorie effective (valable aux échelles d'énergies de la physique nucléaire) avec comme degrés de liberté effectifs les nucléons et les pions. L'interaction entre nucléons est ancrée dans la QCD par une expansion chirale de l'interaction, et les différents termes de cette expansion sont ordonné via le Weinberg power counting. Cela rend possible une résolution ordre par ordre de l'équation de Schrodinger, le but étant de résoudre cette équation avec la meilleure précision possible et en contrôlant l'erreur sur la solution approchée. L'approche ab-initio privilégie les méthode dite de corrélation-expansion afin de résoudre l'équation de Schrodinger. Ces méthodes sont basées sur une partition de l'hamiltonien en une partie non-perturbée et une partie résiduelle; à la partie non-perturbée correspond une équation aux valeurs propres 'facile à résoudre' donnant les états dit non-perturbés. Enfin, la solution complète est exprimée en terme d'un 'wave operator' agissant sur l'état non-perturbé. Cet opérateur pouvant être traité non-perturbativement ou perturbativement. Dans cette thèse on utilise la Méthode de la Coordonnée Génératrice Projetée (PGCM) qui peut être vue comme l'ordre non perturbé de la PGCM-PT qui est une méthode de corrélation expansion basée sur un traitement perturbatif du wave operator. L'approche PGCM ab-initio a prouvé sa capacité à reproduire la spectroscopie collective (rotation et vibration) de basse énergie, et bien qu'étant non convergée pour les énergies de liaison, l'addition des perturbations via PGCM-PT restaure les corrélations manquantes sur les énergies de liaison. Parmi les diverses sources d'erreur provenant de l'approche ab-initio, celle qui nous occupe dans cette thèse est l'erreur provenant des paramètres de l'interaction, et les question motivant la thèse sont les suivantes: Quelles observables déterminent le plus les paramètres de l'interaction ? Et : comment propager les erreur du fit jusqu'au observables ? Les outils standard pour répondre à ces questions proviennent des domaines des analyses de sensibilité et des propagations d'erreurs. Cependant de telles techniques sont à l'heure actuelle inutilisable dans le cadre de la PGCM, cela provient du coût numérique trop élevé d'un calcul PGCM. Une idée pour contourner la difficulté est d'utiliser un émulateur, le but de cette thèse est de construire un tel émulateur et d'en étudier le performances et limites. D'un point de vue général, le but d'un émulateur est de reproduire un calcul cible appelé le simulateur (dans le contexte de cette thèse le simulateur est la PGCM). L'intérêt de l'émulateur est de reproduire fidèlement le simulateur tout en ayant un coût numérique négligeable relativement au simulateur. Ainsi, l'analyse de sensibilité devient possible au niveau de l'émulateur. Dans cette thèse l'émulateur choisi repose sur la méthode 'Eigenvector Continuation' (EC), qui est précisément un moyen général d'émuler les propriétés spectrales (vecteurs propres et valeurs propres) d'un hamiltonien ayant une dépendance paramétrique. Cette technique a prouvé son efficacité dans une multitude de problèmes de physique (nucléaire) comme par exemple les transitions de phase, et

la diffusion. Dans cette thèse je décris l'algorithme permettant l'émulation de la PGCM avec la méthode EC. L'algorithme tire parti d'une hypothèse sur la structure de l'interaction, qui est supposée admettre une décomposition en une somme d'opérateurs indépendants des paramètres multipliés par une fonction des paramètres. Cette hypothèse implique une grande réduction de complexité, dont la plus grande part est transférée au calcul de quantités indépendantes des paramètres (les kernels hors diagonaux généralisés). L'émulateur ainsi obtenu est testé sur un modèle simplifié (brisure de la seule symétrie de rotation, pas de projection, interaction de Brink-Boecker, ...) et appliqué à un noyau de Neon 20. Ce modèle d'étude démontre que l'émulateur PGCM-EC donne une reproduction satisfaisante des observables suivantes : énergies absolues (0.1% d'erreur), énergies d'excitation (5 % d'erreur), et rayon chargé (0.2% d'erreur). Je décris en détail les limites de cet émulateur, notamment les sur (sous) entraînement provenant de la spécificité de l'émulateur (de nature variationnelle). Ces notions sont étudiées avec soin et caractérisées géométriquement par la définition d'une distance entre sous-espaces vectoriels, qui permet de quantifier la qualité de l'émulation de l'espace PGCM cible par l'espace d'entraînement. On met en évidence une corrélation entre cette distance entre espaces et la performance de l'émulateur. Pour des études futures, il serait intéressant de construire une version modifiée de l'émulateur ne souffrant pas du sur entraînement. Même sans cette version modifiée, l'émulateur actuel peut modulo des modifications mineures permettre des études de spectroscopie PGCM à grande échelle pour des interactions ab-initio et EDF tout en propageant les incertitudes sur les paramètres d'interaction.

Remerciements

Notre seul espoir est de tout reprogrammer.

Code Lyoko, *Un monde sans danger*
F. Keller, Y. Amar et J. Lamassonne.

En tout premier je tiens à te remercier Thomas, c'est grâce à ton exigence (et ta patience) que je suis venu à bout de cette thèse; avec toi j'ai pu faire l'expérience pleine et entière de la recherche scientifique. Merci Jean-Paul pour les belles discussions de physique et pour les séances intenses de débogage du code sur les champs. Merci Mikael pour ton aide précieuse en optimisation de code.

Ensuite je remercie chaleureusement les rapporteurs et membres du jury pour m'avoir accordé le titre de docteur.

Je remercie également les collègues des laboratoires (Bruyère + Saclay) ainsi que toute l'équipe des stagiaires, doctorants et post-doctorants. Un grand merci à Sophie, Gilbert, Noel, Nathalie, David, Cyrille, Stéphane, Vittorio, Luis, Alice, Paul, Enzo, Paul, Philippe, Juna, Owen, Mathilde, David, Cyril, Baptiste, Geoffrey, Lysandra, Victor, Gael, Angela, Alberto, Benjamin, Andrea, Gianluca, Stavros, ...

Spéciale dédicace à Paul Carpentier pour son enthousiasme et pour toutes les discussions de maths, et encore désolé pour la preuve qui n'en finissait pas sur les équations différentielles.

Spéciale dédicace à Enzo pour son humour, et pour avoir tenté de m'expliquer ce qu'est un orbifold.

Spéciale dédicace à Luis pour tous les bons moments, et pour les livres de SF.

Thank you Mike Oldfield for the good music (fueled the writing of the code and manuscript).

Enfin, je remercie du fond du coeur ma famille, et Anne-Laure.

Viroflay, le 4 novembre 2024

Contents

| | |
|--|-----------|
| Introduction | 15 |
| 1 Projected Generator Coordinate Method | 19 |
| 1.1 Nuclear hamiltonian | 20 |
| 1.2 PGCM state | 21 |
| 1.3 Hill-Wheeler-Griffin equation | 21 |
| 1.4 Constrained Hartree-Fock-Bogoliubov states | 22 |
| 1.4.1 Bogoliubov state | 22 |
| 1.4.2 Hartree-Fock-Bogoliubov equations | 22 |
| 1.5 Off-diagonal reduced Hamiltonian overlap | 23 |
| 1.5.1 Off-diagonal one-body density matrices | 23 |
| 1.5.2 Off-diagonal Wick theorem | 24 |
| 1.5.3 Off-diagonal one-body fields | 25 |
| 1.6 PGCM subspace | 25 |
| 1.7 Orthonormal basis and effective dimension | 26 |
| 1.8 Solving the Hill-Wheeler-Griffin equation | 26 |
| 2 PGCM-EC | 29 |
| 2.1 Eigenvector continuation technique | 29 |
| 2.1.1 Principle | 29 |
| 2.1.2 Over training | 31 |
| 2.2 Emulating the PGCM with EC | 31 |
| 2.3 PGCM-EC emulator algorithm | 32 |
| 2.3.1 Building blocks of the algorithm | 33 |
| 3 Interaction | 39 |
| 3.1 Gogny pseudo-potential | 40 |
| 3.2 Basis functions | 41 |
| 3.2.1 Orthonormality relations | 42 |
| 3.2.2 Talman coefficients | 42 |
| 3.2.3 Moshinsky coefficients | 42 |
| 3.3 Calculation of matrix elements | 43 |
| 3.3.1 Central term | 43 |
| 3.3.2 Coulomb term | 44 |
| 3.3.3 Two-body center of mass correction | 44 |
| 3.3.4 Density term | 45 |
| 3.3.5 Spin-orbit term | 46 |

| | | |
|----------|--|-----------|
| 4 | PGCM-EC model study | 47 |
| 4.1 | Brink-Boeker potential | 47 |
| 4.2 | GCM setting | 50 |
| 4.3 | Latin hypercube sampling | 51 |
| 4.4 | Cost function | 51 |
| 4.5 | PGCM-EC setting | 52 |
| 4.5.1 | Parameter space | 52 |
| 4.5.2 | Set of HF states | 52 |
| 4.5.3 | Set of kernels | 52 |
| 4.6 | Brute-force learning | 53 |
| 5 | PGCM-EC model results | 55 |
| 5.1 | Training on excited states | 55 |
| 5.2 | Optimisation | 57 |
| 5.3 | Matter radius | 59 |
| 5.4 | Over training | 59 |
| 5.5 | Conclusions | 62 |
| 6 | Subspace distances | 65 |
| 6.1 | Metric | 65 |
| 6.1.1 | Definitions | 65 |
| 6.2 | Parameters distance | 66 |
| 6.2.1 | Parameter distance | 66 |
| 6.3 | Subspaces distance | 66 |
| 6.3.1 | Identical dimensions | 67 |
| 6.3.2 | Different dimensions | 69 |
| 6.3.3 | Limit cases | 71 |
| 6.4 | Numerical tests | 71 |
| 6.4.1 | Inclusion and orthogonality | 71 |
| 6.4.2 | Distances between GCM subspaces | 72 |
| 6.4.3 | Distance to training subspace | 73 |
| 7 | Training regimes in PGCM-EC | 79 |
| 7.1 | Error versus distance to training subspace | 79 |
| 7.2 | Training regimes | 81 |
| 7.3 | Conclusions | 81 |
| 8 | Conclusions | 85 |
| | Conclusions | 85 |
| I | Appendices | 89 |
| A | Symmetry group | 91 |
| A.1 | Unitary representation | 91 |
| A.2 | Projection operators | 92 |
| B | Hill-Wheeler-Griffin equation | 93 |

| | |
|---|------------|
| <i>Contents</i> | 13 |
| C Talman coefficients and integral relations | 95 |
| C.1 Talman coefficients | 95 |
| C.1.1 Integral relations | 96 |
| D Moshinsky coefficients | 97 |
| E Spherical change of coordinates | 99 |
| F Recurrence relations for basis functions | 101 |
| F.1 Recurrence relations for Hermite and Laguerre polynomials | 101 |
| F.2 Axial part | 102 |
| F.3 Perpendicular part | 102 |
| G Gogny matrix elements and fields | 103 |
| G.1 Central term | 103 |
| G.2 Coulomb term | 104 |
| G.3 Center of mass term | 106 |
| G.4 Density term | 107 |
| G.4.1 Density field | 107 |
| G.4.2 Rearrangment field | 107 |
| G.5 Spin-orbit term | 108 |

Introduction

Nuclear theory is the field of physics devoted to the theoretical study of atomic nuclei and their measurable properties. As of today, such theoretical description is still an open challenge. The most promising route for a unified theory at low energy relies on effective (field) theories (EFT) where N point-like neutrons and Z point-like protons interact via models of two-nucleon interactions, three-nucleon interactions. . . rooted into the underlying gauge theory of the strong force, i.e. quantum chromodynamics (QCD). In this context, the complexity of *ab initio* calculations arises from

1. the systematic construction of inter-nucleon interaction models;
2. the presence of many-body interaction terms due to neglecting nucleons' internal structure;
3. the non-perturbative character of inter-nucleon interactions;
4. the exponential growth of the A-body Hilbert space's dimension making (quasi-)exact solutions of A-body Schroedinger's equation only available up to $A = 3$ (16).

Despite this complexity, *ab initio* nuclear theory has made spectacular progress over the last 15 years to address the above challenges. First, novel generations of inter-nucleon interactions rooted into QCD were built within the frame of chiral effective field theory (χ -EFT). Such nuclear interactions are typically made more amenable to an efficient solving of the A-body Schrodinger equation via a similarity renormalisation group (SRG) transformation [1]. Second, several so-called expansion techniques [2], i.e. self-Consistent Greens' functions (SCGF) theory [3, 4, 5, 6], coupled cluster theory (CC) [7, 8, 9, 10, 11, 12], many-body perturbation theory (MBPT) [13, 14, 15, 16, 17, 18, 19, 20, 21, 22], the in-medium similarity renormalization group (IMSRG) [23, 24, 25, 26, 27, 28, 29, 30] have been designed and implemented to solve the A-body problem at polynomial cost with system's size. Because these methods operate via an expansion of the exact solution to be truncated, many-body uncertainties can be assessed systematically by going through successive truncation orders. While the zero-order term of most of the above methods corresponds to a single Slater determinant or Bogoliubov state, an advanced perturbation theory based on a projected generator coordinate method unperturbed state (PGCM-PT) [21, 31, 32] has been designed recently in order to already capture strong static correlations via the unperturbed state while satisfying symmetries.

The projected generator coordinate method (PGCM) [33] is a versatile method to study low-lying collective rotational and vibrational excitations based on phenomenological energy density functionals (EDFs) [34, 35, 36]¹. Recently, the PGCM has been shown to be well suited to study neutrino-less double beta decay [42, 43]² and giant resonances [44, 45, 46]. The PGCM explicitly accounts for so-called strong (i.e. *static*) correlations via the mixing of symmetry-breaking Slater determinants or Bogoliubov vacua along with the subsequent restoration of the broken symmetries through the application of a (set of) projection operator(s). In spite of constituting only the zero-order contribution to PGCM-PT [47], excitation energies

¹The PGCM is also employed as a low-cost alternative to shell-model diagonalization in valence-space calculations [37, 38, 39, 40, 41].

²These calculations combine PGCM and IMSRG approaches.

of low-lying collective states were shown to be already well converged at zero-order i.e. at the PGCM level, due the fine-tuned cancellation of *dynamical correlations* in such energy differences [48]. As such, the PGCM can be used to good approximation as a standalone method to investigate collective excitations in nuclei [49, 44, 45, 46].

Ab initio calculations based on many-body expansion methods come with several uncertainty sources

1. Bases representation
 - (a) One-body, two-body and three-body basis truncations
2. Hamiltonian modelling
 - (a) Chiral EFT truncation order
 - (b) Truncated SRG transformation
 - (c) Low energy constants (LECs) determination
3. Many-body solution
 - (a) Nature of the, e.g. PGCM, unperturbed state
 - (b) Truncated, e.g. PGCM-PT, expansion

In present days, it is considered crucial to accompany theoretical predictions with uncertainty quantification. Many efforts are currently being made to address the above uncertainty sources. In this context, the present work focuses on a single source associated with the determination of the LECs parameterizing the Hamiltonian (2(c)) via a fit on a set of experimental data. The goal is typically to either perform a sensitivity analysis with respect to the LECs of many-body observables computed via the PGCM or to propagate the statistical uncertainties associated with the fitted LECs to the same many-body observables.

Performing such a statistical analysis typically requires to run a very large number of PGCM simulations associated with many realization of the parameter values, a cost that grows exponentially with model complexity, i.e. the number of parameters entering the interaction. While a single PGCM calculation is inexpensive compared to the PGCM-PT corrections computed on top to deliver a high-accuracy solution to Schroedinger's equation, it can still typically correspond to a costly simulation that cannot easily be repeated a million times. To circumvent this difficulty, one can bypass the heavy simulations by designing an accurate enough *emulator* at a small fraction of the simulator cost. The emulator is typically constructed by training it over a small number of heavy simulations. Eventually, one can emulate thousands or millions of simulations at a negligible cost.

In this context, the present thesis focuses on the construction of a PGCM emulator based on the so-called eigenvector continuation (EC) method [50, 51]. The EC belongs to the larger class of reduced basis methods (RBM) [52] and has already been applied successfully to many different nuclear structure and reaction problems over the past few years [53, 54, 55, 56, 57, 58, 59, 60, 61, 62, 63]. While the PGCM formalism is ideally suited to applying EC to it, the very reason of its success, i.e. the use of a physically-motivated low-dimensional subspace of the full Hilbert space, is rather in tension with EC. The goal of the present work is thus to quantify the performances and limits of the PGCM-EC emulator as well as to further understand the origins of these limits. Doing so, this thesis paves the way for future sensitivity analysis of/uncertainty propagation to collective nuclear excitations within the PGCM and for a further extension to emulate even more costly PGCM-PT simulations.

The manuscript is organized as follows. Chapter 1 lays down the PGCM formalism and the notations in use, with an emphasis on the interaction parameter dependencies that need to be made explicit in view of formulating the PGCM-EC in chapter 2. This chapter details the algorithm employed to implement the PGCM-EC emulator and discusses the possible over-training of the emulator. In view of applying the

PGCM-EC on the basis of Brink-Boeker interaction, complete formulas for the matrix elements and one-body mean-fields of the Gogny effective interaction are provided in Chap. 3 and in associated appendices. In Chap. 4, the specific numerical setting of the study is specified whereas the associated results are gathered in Chap. 5 where the performance of the PGCM-EC emulator is characterized. In Chap. 6, the notion of distance between two subspaces of the Hilbert space is introduced and numerically studied in order to understand the observed lower bound on the error attained by the PGCM-EC emulator in Chap. 5. In the next chapter, i.e. Chap. 7, this distance is used to characterize the fact that the PGCM-EC emulator experiences three different regimes as a function of the number of training points: an under-training regime, an optimal-training regime and an over-training regime. Conclusions of the present work are eventually provided in Chap. 8.

Chapter 1

Projected Generator Coordinate Method

Contents

| | |
|---|-----------|
| 1.1 Nuclear hamiltonian | 20 |
| 1.2 PGCM state | 21 |
| 1.3 Hill-Wheeler-Griffin equation | 21 |
| 1.4 Constrained Hartree-Fock-Bogoliubov states | 22 |
| 1.4.1 Bogoliubov state | 22 |
| 1.4.2 Hartree-Fock-Bogoliubov equations | 22 |
| 1.5 Off-diagonal reduced Hamiltonian overlap | 23 |
| 1.5.1 Off-diagonal one-body density matrices | 23 |
| 1.5.2 Off-diagonal Wick theorem | 24 |
| 1.5.3 Off-diagonal one-body fields | 25 |
| 1.6 PGCM subspace | 25 |
| 1.7 Orthonormal basis and effective dimension | 26 |
| 1.8 Solving the Hill-Wheeler-Griffin equation | 26 |

In this chapter, the projected generator coordinate method (PGCM) formalism is introduced. A PGCM state represents the zero-order contribution to a perturbative series built on top of it coined as PGCM-PT [47] that formally delivers exact solutions of the nuclear many-body problem. By truncating this series, systematically improvable solutions of A-body Schrodinger's equation can be obtained that are particularly suited to access collective nuclear excitations. It happens that excitation energies of low-lying collective states are already well converged at zero-order i.e. at the PGCM level, due to the fine-tuned cancellation of dynamical correlations in such energy differences [48]. In this context, the thesis explores the possibility to accurately emulate PGCM simulations that are quantitatively relevant to the description of rotational and vibrational excitations [49, 44, 45, 46], leaving the possible emulation of PGCM-PT simulations to a future investigation.

1.1 Nuclear hamiltonian

Considering an arbitrary orthonormal basis $\{a_\alpha, a_\alpha^\dagger\}$ of the one-body Hilbert space \mathcal{H}_1 ¹, the nuclear Hamiltonian reads as

$$\begin{aligned}
H^\lambda &\equiv T + V^\lambda + W^\lambda \\
&\equiv \frac{1}{(1!)^2} \sum_{\alpha\beta} t_{\alpha\beta} a_\alpha^\dagger a_\alpha \\
&\quad + \frac{1}{(2!)^2} \sum_{\alpha\beta\gamma\delta} \bar{v}_{\alpha\beta\gamma\delta}^\lambda a_\alpha^\dagger a_\beta^\dagger a_\delta a_\gamma \\
&\quad + \frac{1}{(3!)^2} \sum_{\alpha\beta\gamma\delta\epsilon\zeta} \bar{w}_{\alpha\beta\gamma\delta\epsilon\zeta}^\lambda a_\alpha^\dagger a_\beta^\dagger a_\gamma^\dagger a_\zeta a_\epsilon a_\delta,
\end{aligned} \tag{1.2}$$

where T denotes the kinetic energy operator. Matrix elements $\bar{v}_{\alpha\beta\gamma\delta}^\lambda$ ($\bar{w}_{\alpha\beta\gamma\delta\epsilon\zeta}^\lambda$) of the two-nucleon (three-nucleon) interaction are antisymmetric with respect to their first two (three) and last two (three) indices. In Eq. (1.2), the dependence of the Hamiltonian (i.e. interactions) on the set of parameters

$$\lambda \equiv (\lambda^1, \lambda^2, \dots, \lambda^{n_p}) \in \mathbb{R}^{n_p}, \tag{1.3}$$

has been made explicit given the key role this dependence plays in the present work. As a matter of fact, the dependence on the interaction parameters is explicitly propagated to all algebraic formulas appearing in the present manuscript.

The main objective of nuclear many-body theory is to access the eigenstates and eigenenergies of H^λ

$$H^\lambda |\Psi_\mu^\sigma(\lambda)\rangle = E_\mu^{\tilde{\sigma}}(\lambda) |\Psi_\mu^\sigma(\lambda)\rangle, \tag{1.4}$$

where μ denotes a principal quantum number while $\sigma \equiv (JM\Pi NZ) \equiv (\tilde{\sigma}M)$ collects the set of symmetry quantum numbers labelling the many-body states: J and M denote the total angular momentum and its projection in the laboratory frame, respectively, while Π refers to the parity and $N(Z)$ to the neutron (proton) number. The M -independence of the eigenenergies $E_\mu^{\tilde{\sigma}}(\lambda)$ and the symmetry quantum numbers labeling the states relate to the symmetry group of the Hamiltonian²

$$G_H \equiv \{R(\theta), \theta \in D_G\}, \tag{1.5}$$

of volume v_G , where denotes $R(\theta)$ a unitary representation of the symmetry transformations on Fock space \mathcal{F} parameterized by the angle θ . The subscript $\tilde{\sigma}$ introduced above labels the irreducible representations (IRREPs) of G_H carrying dimension $d_{\tilde{\sigma}}$ and spanned by a set of states distinguished by the quantum number $1 \leq M \leq d_{\tilde{\sigma}}$.

¹In practice, one works with the finite-dimensional subspace $\tilde{\mathcal{H}}_1$ of \mathcal{H}_1 of dimension $\dim \tilde{\mathcal{H}}_1 \equiv n^{\dim} \equiv n_1^{\dim}$ such that the resulting A -body Hilbert space has dimension

$$\dim \tilde{\mathcal{H}}_A \equiv n_A^{\dim} = \binom{n^{\dim}}{A}. \tag{1.1}$$

Eventually, the truncated Fock space has dimension $\dim \tilde{\mathcal{F}} = 2^{n^{\dim}}$.

²The symmetry group G_H is independent of λ .

1.2 PGCM state

Given a set of non-orthogonal Bogoliubov states $B_{n_q}^\lambda \equiv \{|\Phi^\lambda(q)\rangle; q \in S\}$ differing by the value of the (possibly multidimensional) collective coordinate $q \in \{q_1, q_2, \dots, q_{n_q}\} \equiv S$, the PGCM state is written as [33]

$$|\Theta_a^{\sigma\lambda}\rangle \equiv \sum_{q \in S} f_a^{\sigma\lambda}(q) P_{M0}^{\tilde{\sigma}} |\Phi^\lambda(q)\rangle, \quad (1.6)$$

where $f_a^{\sigma\lambda}(q)$ are unknown mixing coefficients to be determined. In Eq. (1.6), the operator $P_{M0}^{\tilde{\sigma}}$ collects the projection operators onto good symmetry quantum numbers, i.e. angular momentum and its third projection, neutron and proton numbers as well as parity³

$$P_{M0}^{\tilde{\sigma}} \equiv \frac{d_{\tilde{\sigma}}}{v_G} \int_{D_G} d\theta D_{M0}^{\tilde{\sigma}*}(\theta) R(\theta) \quad (1.7)$$

where $D_{M0}^{\tilde{\sigma}}(\theta)$ denotes the irreducible representations of G_H . The notation θ effectively captures all the rotation angles $(\Omega, \phi_p, \phi_n, \phi_\pi)$ characterizing the symmetry transformations in G_H . See App. A for more details regarding the symmetry group, the associated quantum numbers and the symmetry projector.

Introducing the rotated state as

$$|\Phi^\lambda(q; \theta)\rangle \equiv R(\theta) |\Phi^\lambda(q)\rangle, \quad (1.8)$$

which is itself a Bogoliubov state by virtue of Thouless theorem [64], the PGCM state eventually reads as

$$|\Theta_a^{\sigma\lambda}\rangle = \frac{d_{\tilde{\sigma}}}{v_G} \sum_q f_a^{\sigma\lambda}(q) \sum_\theta D_{M0}^{\tilde{\sigma}*}(\theta) |\Phi^\lambda(q; \theta)\rangle, \quad (1.9)$$

where the integral over θ has been appropriately discretized.

1.3 Hill-Wheeler-Griffin equation

The unknown coefficients $f_a^{\sigma\lambda}(q)$ appearing in Eq. (1.9) are determined via the application of Ritz' variational principle

$$\frac{\delta}{\delta f_a^{\sigma\lambda}(q)} \frac{\langle \Theta_a^{\sigma\lambda} | H^\lambda | \Theta_a^{\sigma\lambda} \rangle}{\langle \Theta_a^{\sigma\lambda} | \Theta_a^{\sigma\lambda} \rangle} = 0, \quad (1.10)$$

that eventually leads to solving Hill-Wheeler-Griffin's (HWG) equation (see App. B)

$$\sum_{q'} \left[\langle \Phi^\lambda(q) | H^\lambda P_{00}^{\tilde{\sigma}} | \Phi^\lambda(q') \rangle - E_a^{\tilde{\sigma}\lambda} \langle \Phi^\lambda(q) | P_{00}^{\tilde{\sigma}} | \Phi^\lambda(q') \rangle \right] f_a^{\tilde{\sigma}\lambda}(q') = 0, \quad (1.11)$$

which also delivers the PGCM energy $E_a^{\tilde{\sigma}\lambda}$. In order to solve the HWG equation, the *projected norm and Hamiltonian kernels*

$$N_{qq'}^{\tilde{\sigma}\lambda} \equiv \langle \Phi^\lambda(q) | P_{00}^{\tilde{\sigma}} | \Phi^\lambda(q') \rangle, \quad (1.12)$$

$$H_{qq'}^{\tilde{\sigma}\lambda} \equiv \langle \Phi^\lambda(q) | H^\lambda P_{00}^{\tilde{\sigma}} | \Phi^\lambda(q') \rangle, \quad (1.13)$$

³The present work is concerned with deformed Bogoliubov states remaining invariant under spatial rotation around a given symmetry axis. Extending the formulation to the case where $|\Phi^\lambda(q)\rangle$ does not display such a symmetry poses no formal difficulty but requires a more general projection operator P^σ ; see App. A for details.

must be evaluated. Expanding the projection operator, these kernels read as

$$N_{qq'}^{\tilde{\sigma}\lambda} = \frac{d_{\tilde{\sigma}}^2}{v_G^2} \sum_{\theta} D_{00}^{\tilde{\sigma}*}(\theta) \langle \Phi^{\lambda}(q) | \Phi^{\lambda}(q'; \theta) \rangle, \quad (1.14a)$$

$$H_{qq'}^{\tilde{\sigma}\lambda} = \frac{d_{\tilde{\sigma}}^2}{v_G^2} \sum_{\theta} D_{00}^{\tilde{\sigma}*}(\theta) \langle \Phi^{\lambda}(q) | H^{\lambda} | \Phi^{\lambda}(q'; \theta) \rangle, \quad (1.14b)$$

where the building blocks appear to be the *off-diagonal norm overlap* and the *off-diagonal reduced Hamiltonian overlap*, respectively defined as

$$N^{\lambda}(q, q'; \theta) \equiv \langle \Phi^{\lambda}(q) | \Phi^{\lambda}(q'; \theta) \rangle, \quad (1.15a)$$

$$h^{\lambda}(q, q'; \theta) \equiv \frac{\langle \Phi^{\lambda}(q) | H^{\lambda} | \Phi^{\lambda}(q'; \theta) \rangle}{\langle \Phi^{\lambda}(q) | \Phi^{\lambda}(q'; \theta) \rangle}. \quad (1.15b)$$

1.4 Constrained Hartree-Fock-Bogoliubov states

1.4.1 Bogoliubov state

A Bogoliubov state $|\Phi^{\lambda}(q)\rangle$ is defined as the vacuum

$$\beta_k(q; \lambda) |\Phi^{\lambda}(q)\rangle = 0 \quad \forall k, \quad (1.16)$$

of a set of quasi-particle operators $\{\beta^{\dagger}(q; \lambda), \beta(q; \lambda)\}$ connected to the set of particle operators $\{a^{\dagger}, a\}$ via a unitary Bogoliubov transformation [33]

$$\begin{pmatrix} \beta(q; \lambda) \\ \beta^{\dagger}(q; \lambda) \end{pmatrix} = \mathcal{W}^{\lambda\dagger}(q) \begin{pmatrix} a \\ a^{\dagger} \end{pmatrix}, \quad (1.17)$$

with

$$\mathcal{W}^{\lambda}(q) \equiv \begin{pmatrix} U^{\lambda}(q) & V^{\lambda*}(q) \\ V^{\lambda}(q) & U^{\lambda*}(q) \end{pmatrix}. \quad (1.18)$$

The unitary character of the Bogoliubov transformation implies that canonical anti-commutation rules valid for particle operators extend to quasi-particle ones

$$\{\beta_k^{\dagger}(q; \lambda), \beta_l^{\dagger}(q; \lambda)\} = 0, \quad (1.19a)$$

$$\{\beta_k(q; \lambda), \beta_l(q; \lambda)\} = 0, \quad (1.19b)$$

$$\{\beta_k(q; \lambda), \beta_l^{\dagger}(q; \lambda)\} = \delta_{kl}. \quad (1.19c)$$

1.4.2 Hartree-Fock-Bogoliubov equations

Given a set of *constraining operators* Q , the states belonging to the set $B_{n_q}^{\lambda} \equiv \{|\Phi^{\lambda}(q)\rangle; q \in S\}$ are obtained by solving n_q times *constrained* Hartree-Fock-Bogoliubov (HFB) equations

$$\begin{pmatrix} h^{\lambda}(q) & \Delta^{\lambda}(q) \\ -\Delta^{*\lambda}(q) & -h^{*\lambda}(q) \end{pmatrix} \begin{pmatrix} U^{\lambda}(q) \\ V^{\lambda}(q) \end{pmatrix} = E(q) \begin{pmatrix} U^{\lambda}(q) \\ V^{\lambda}(q) \end{pmatrix}. \quad (1.20)$$

obtained by applying Ritz' variational under constraints within the manifold of Bogoliubov states.

In Eq. (1.20), the one-body HFB fields

$$h^\lambda(q) \equiv \frac{\partial R^\lambda(q)}{\partial \rho^{*\lambda}(q)}, \quad (1.21a)$$

$$\Delta^\lambda(q) \equiv \frac{\partial R^\lambda(q)}{\partial \kappa^{*\lambda}(q)}, \quad (1.21b)$$

are obtained from the Routhian

$$R^\lambda(q) \equiv \langle \Phi^\lambda(q) | H^\lambda - \lambda_A (A - \mathbf{A}) - \lambda(q) (Q - q) | \Phi^\lambda(q) \rangle, \quad (1.22)$$

where the *diagonal one-body density matrices* of the Bogoliubov state $|\Phi^\lambda(q)\rangle$ are given by

$$\begin{aligned} \rho_{\alpha\beta}^{qq0\lambda} &\equiv \frac{\langle \Phi^\lambda(q) | a_\beta^\dagger a_\alpha | \Phi^\lambda(q) \rangle}{\langle \Phi^\lambda(q) | \Phi^\lambda(q) \rangle} \\ &= V^{\lambda*}(q) V^{\lambda T}(q), \end{aligned} \quad (1.23a)$$

$$\begin{aligned} \kappa_{\alpha\beta}^{qq0\lambda} &\equiv \frac{\langle \Phi^\lambda(q) | a_\beta a_\alpha | \Phi^\lambda(q) \rangle}{\langle \Phi^\lambda(q) | \Phi^\lambda(q) \rangle} \\ &= V^{\lambda*}(q) U^{\lambda T}(q). \end{aligned} \quad (1.23b)$$

In Eq. (1.22), the Lagrange multipliers λ_A and λ_q are chosen to ensure that the average particle number and the generator coordinate satisfy

$$\langle \Phi^\lambda(q) | A | \Phi^\lambda(q) \rangle = A, \quad (1.24a)$$

$$\langle \Phi^\lambda(q) | Q | \Phi^\lambda(q) \rangle = q, \quad (1.24b)$$

while solving Eq. (1.20).

1.5 Off-diagonal reduced Hamiltonian overlap

Knowing that the states entering $B_{n_q}^\lambda \equiv \{|\Phi^\lambda(q)\rangle; q \in S\}$ are Bogoliubov states, $N^\lambda(q, q'; \theta)$ and $h^\lambda(q, q'; \theta)$ can be evaluated exactly, i.e. while the former can be computed as a Pfaffian [65] or via an integral approach [66], the latter can be obtained via the off-diagonal Wick theorem [67, 68] as is now briefly recalled.

1.5.1 Off-diagonal one-body density matrices

Given the two Bogoliubov states $|\Phi^\lambda(q)\rangle$ and $|\Phi^\lambda(q'; \theta)\rangle$, there are four one-body off-diagonal elementary contractions generalizing the diagonal ones introduced in Eq. (1.23) according to

$$\begin{aligned} \mathcal{R}^\lambda(q, q'; \theta) &\equiv \begin{pmatrix} \frac{\langle \Phi^\lambda(q) | a_\beta^\dagger a_\alpha | \Phi^\lambda(q'; \theta) \rangle}{\langle \Phi^\lambda(q) | \Phi^\lambda(q'; \theta) \rangle} & \frac{\langle \Phi^\lambda(q) | a_\beta a_\alpha | \Phi^\lambda(q'; \theta) \rangle}{\langle \Phi^\lambda(q) | \Phi^\lambda(q'; \theta) \rangle} \\ \frac{\langle \Phi^\lambda(q) | a_\beta^\dagger a_\alpha^\dagger | \Phi^\lambda(q'; \theta) \rangle}{\langle \Phi^\lambda(q) | \Phi^\lambda(q'; \theta) \rangle} & \frac{\langle \Phi^\lambda(q) | a_\beta a_\alpha^\dagger | \Phi^\lambda(q'; \theta) \rangle}{\langle \Phi^\lambda(q) | \Phi^\lambda(q'; \theta) \rangle} \end{pmatrix} \\ &\equiv \begin{pmatrix} +\rho_{\alpha\beta}^{qq'\theta\lambda} & +\kappa_{\alpha\beta}^{qq'\theta\lambda} \\ -\bar{\kappa}_{\alpha\beta}^{qq'\theta\lambda*} & -\sigma_{\alpha\beta}^{qq'\theta\lambda*} \end{pmatrix}. \end{aligned} \quad (1.25)$$

The diagonal case is recovered from Eq. (1.25) for $(q'; \theta) = (q; 0)$ according to

$$\begin{aligned} \mathcal{R}^\lambda(p, q; \theta) &\equiv \begin{pmatrix} +\rho_{\alpha\beta}^{qq0\lambda} & +\kappa_{\alpha\beta}^{qq0\lambda} \\ -\bar{\kappa}_{\alpha\beta}^{qq0\lambda*} & -\sigma_{\alpha\beta}^{qq0\lambda*} \end{pmatrix} \\ &\equiv \begin{pmatrix} [V^{\lambda*}(q)V^{\lambda T}(q)]_{\alpha\beta} & [V^{\lambda*}(q)U^{\lambda T}(q)]_{\alpha\beta} \\ [U^{\lambda*}(q)V^{\lambda T}(q)]_{\alpha\beta} & [U^{\lambda*}(q)U^{\lambda T}(q)]_{\alpha\beta} \end{pmatrix}. \end{aligned} \quad (1.26)$$

The four off-diagonal one-body density matrices can eventually be expressed in terms of the diagonal ones according to [67, 33, 68]

$$\rho_{\alpha\beta}^{qq'\theta\lambda} = \rho_{\alpha\beta}^{qq0\lambda} + [U^\lambda(q)z^\lambda(q, q'; \theta)V^{\lambda T}(q)]_{\alpha\beta} \quad (1.27a)$$

$$\kappa_{\alpha\beta}^{qq'\theta\lambda} = \kappa_{\alpha\beta}^{qq0\lambda} + [U^\lambda(q)z^\lambda(q, q'; \theta)U^{\lambda T}(q)]_{\alpha\beta} \quad (1.27b)$$

$$\bar{\kappa}_{\alpha\beta}^{qq'\theta\lambda*} = \bar{\kappa}_{\alpha\beta}^{qq0\lambda*} - [V^\lambda(q)z^\lambda(q, q'; \theta)V^{\lambda T}(q)]_{\alpha\beta} \quad (1.27c)$$

$$\sigma_{\alpha\beta}^{qq'\theta\lambda*} = \sigma_{\alpha\beta}^{qq0\lambda*} - [V^\lambda(q)z^\lambda(q, q'; \theta)U^{\lambda T}(q)]_{\alpha\beta} \quad (1.27d)$$

where the skew-symmetric Thouless matrix

$$z^\lambda(q, q'; \theta) \equiv A^{\lambda*}(q, q'; \theta)B^{\lambda*-1}(q, q'; \theta), \quad (1.28)$$

is expressed in terms of the two matrices making up the Bogoliubov transformation connecting the two sets of quasi-particle operators associated with $|\Phi^\lambda(q)\rangle$ and $|\Phi^\lambda(q'; \theta)\rangle$

$$A^\lambda(q, q'; \theta) \equiv V^{\lambda T}(q)r(\theta)U^\lambda(q') + U^{\lambda T}(q)r^*(\theta)V^\lambda(q'), \quad (1.29a)$$

$$B^\lambda(q, q'; \theta) \equiv U^{\lambda\dagger}(q)r(\theta)U^\lambda(q') + V^{\lambda\dagger}(q)r^*(\theta)V^\lambda(q'), \quad (1.29b)$$

where $r(\theta)$ is the matrix representation of the operator $R(\theta)$ on the one-body Hilbert space \mathcal{H}_1 .

1.5.2 Off-diagonal Wick theorem

Assuming that $\langle \Phi^\lambda(q) | \Phi^\lambda(q'; \theta) \rangle \neq 0$, the off-diagonal reduced Hamiltonian overlap can be expressed, by virtue of the off-diagonal Wick theorem [67, 68], in terms of the off-diagonal one-body density matrices introduced above according to

$$\begin{aligned} h^\lambda(q, q'; \theta) &= \sum_{\alpha\beta} t_{\alpha\beta} \rho_{\beta\alpha}^{qq'\theta\lambda} \\ &+ \frac{1}{2} \sum_{\alpha\beta\gamma\delta} \bar{v}_{\alpha\beta\gamma\delta}^\lambda \rho_{\gamma\alpha}^{qq'\theta\lambda} \rho_{\delta\beta}^{qq'\theta\lambda} + \frac{1}{4} \sum_{\alpha\beta\gamma\delta} \bar{v}_{\alpha\beta\gamma\delta}^\lambda \bar{\kappa}_{\alpha\beta}^{qq'\theta\lambda} \kappa_{\gamma\delta}^{qq'\theta\lambda} \\ &+ \frac{1}{6} \sum_{\alpha\beta\gamma\delta\epsilon\zeta} \bar{w}_{\alpha\beta\gamma\delta\epsilon\zeta}^\lambda \rho_{\delta\alpha}^{qq'\theta\lambda} \rho_{\epsilon\beta}^{qq'\theta\lambda} \rho_{\zeta\gamma}^{qq'\theta\lambda} + \frac{1}{4} \sum_{\alpha\beta\gamma\delta\epsilon\zeta} \bar{w}_{\alpha\beta\gamma\delta\epsilon\zeta}^\lambda \rho_{\delta\alpha}^{qq'\theta\lambda} \bar{\kappa}_{\beta\gamma}^{qq'\theta\lambda} \kappa_{\epsilon\zeta}^{qq'\theta\lambda} \\ &+ \dots \end{aligned} \quad (1.30)$$

1.5.3 Off-diagonal one-body fields

Further introducing the two *off-diagonal one-body fields* generalizing their diagonal counterparts appearing in Eq. (1.21)

$$\begin{aligned}
h_{\alpha\gamma}^{qq'\theta\lambda} &\equiv t_{\alpha\gamma} + \frac{1}{2} \sum_{\beta\delta} \bar{v}_{\alpha\beta\gamma\delta}^{\lambda} \rho_{\delta\beta}^{qq'\theta\lambda} \\
&+ \frac{1}{6} \sum_{\beta\delta\epsilon\zeta} \bar{w}_{\alpha\beta\delta\gamma\epsilon\zeta}^{\lambda} \rho_{\epsilon\beta}^{qq'\theta\lambda} \rho_{\zeta\delta}^{qq'\theta\lambda} \\
&+ \frac{1}{4} \sum_{\beta\delta\epsilon\zeta} \bar{w}_{\alpha\beta\delta\gamma\epsilon\zeta}^{\lambda} \bar{\kappa}_{\beta\delta}^{qq'\theta\lambda} \kappa_{\epsilon\zeta}^{qq'\theta\lambda} \\
&+ \dots,
\end{aligned} \tag{1.31}$$

and

$$\begin{aligned}
\Delta_{\alpha\gamma}^{qq'\theta\lambda} &\equiv \frac{1}{4} \sum_{\beta\delta} \bar{v}_{\alpha\gamma\beta\delta}^{\lambda} \kappa_{\beta\delta}^{qq'\theta\lambda} \\
&+ \frac{1}{4} \sum_{\beta\delta\epsilon\zeta} \bar{w}_{\beta\alpha\gamma\delta\epsilon\zeta}^{\lambda} \rho_{\delta\beta}^{qq'\theta\lambda} \kappa_{\epsilon\zeta}^{qq'\theta\lambda} \\
&+ \dots,
\end{aligned} \tag{1.32}$$

the off-diagonal reduced Hamiltonian overlap can finally be expressed as

$$h^{\lambda}(q, q'; \theta) = \sum_{\alpha\gamma} h_{\alpha\gamma}^{qq'\theta\lambda} \rho_{\gamma\alpha}^{qq'\theta\lambda} + \Delta_{\alpha\gamma}^{qq'\theta\lambda} \bar{\kappa}_{\alpha\gamma}^{qq'\theta\lambda}. \tag{1.33}$$

1.6 PGCM subspace

To summarize, given the parameter $\lambda \in \mathbb{R}^{n_p}$ and the (set of) hermitian operator(s) Q , the n_q non-orthogonal Bogoliubov states

$$B_{n_q}^{\lambda} \equiv \{ |\Phi^{\lambda}(q)\rangle ; q = 1, \dots, n_q \}, \tag{1.34}$$

are used to generate, via the restoration of symmetries after variation through the application of the projector $P_{M0}^{\tilde{\sigma}}$, the new set associated with the irreducible representation $\tilde{\sigma}$ of the symmetry group

$$\text{PB}_{n_q}^{\sigma\lambda} \equiv \{ P_{M0}^{\tilde{\sigma}} |\Phi^{\lambda}(q)\rangle ; q = 1, \dots, n_q \}. \tag{1.35}$$

The set $\text{PB}_{n_q}^{\sigma\lambda}$ constitutes the starting point of the PGCM calculation realized for the Hamiltonian H^{λ} . Correspondingly, one introduces the *PGCM subspace* as⁴

$$E_{n_q}^{\sigma\lambda} \equiv \text{Span}\{\text{PB}_{n_q}^{\sigma\lambda}\}. \tag{1.36}$$

For reasons that will become clear later on, considering the n_t different PGCM subspaces obtained following the above protocole for parameter values belonging to so-called *training set*

$$L_{n_t} \equiv \{ \lambda_1, \lambda_2, \dots, \lambda_{n_t} \}, \tag{1.37}$$

⁴In case the calculation is limited to the GCM, everything that follows can be applied at the prize of removing the projector $P_{M0}^{\tilde{\sigma}}$, i.e. going back to the set $B_{n_q}^{\lambda}$. Correspondingly, the labels P , M , K and $\tilde{\sigma}$ must be removed from all the expressions below, and $d_{\tilde{\sigma}}$ put to 1.

the *super* set

$$\mathbf{PB}_{n_q}^{\sigma L_{n_t}} \equiv \bigcup_{\lambda \in L_{n_t}} \mathbf{PB}_{n_q}^{\sigma \lambda} . \quad (1.38)$$

spanning the *training* PGCM subspace

$$\mathbf{E}_{n_q}^{\sigma L_{n_t}} \equiv \text{Span}\{\mathbf{PB}_{n_q}^{\sigma L_{n_t}}\}, \quad (1.39)$$

is introduced.

1.7 Orthonormal basis and effective dimension

The PGCM subspace $\mathbf{E}_{n_q}^{\sigma \lambda}$ being spanned by a finite number of non-orthogonal projected Bogoliubov states, it is useful to extract an orthonormal basis along with its (effective) dimension. To do so, the hermitian matrix associated with the projected norm kernel $N_{qq'}^{\sigma \lambda}$ is diagonalized according to

$$N^{\sigma \lambda} U^{\sigma \lambda} = S^{\sigma \lambda} U^{\sigma \lambda} , \quad (1.40)$$

where the diagonal matrix $S^{\sigma \lambda} = \text{diag}(s_1^{\sigma \lambda}, \dots, s_{n_q}^{\sigma \lambda})$ contains the n_q eigenvalues of $N^{\sigma \lambda}$ arranged in descending order and where $U^{\sigma \lambda}$ is a $n_q \times n_q$ unitary matrix, whose columns are eigenvectors of $N^{\sigma \lambda}$.

The matrix $N^{\sigma \lambda}$ being positive semi-definite, the eigenvalues satisfy

$$s_1^{\sigma \lambda} \geq s_2^{\sigma \lambda} \geq \dots \geq s_{r^{\sigma \lambda}}^{\sigma \lambda} > 0 = s_{r^{\sigma \lambda}+1}^{\sigma \lambda} = \dots = s_{n_q}^{\sigma \lambda} , \quad (1.41)$$

such that, due to potential linear redundancies between vectors in $\mathbf{PB}_{n_q}^{\sigma \lambda}$, eigenvalues are strictly zero beyond a certain rank $r^{\sigma \lambda}$. Furthermore, quasi-linear redundancies typically generate very small eigenvalues that need to be truncated below a chosen threshold $\epsilon^{\sigma \lambda}$ to allow numerically stable linear algebra operations. This eventually leads to keeping $\check{r}^{\sigma \lambda} \leq r^{\sigma \lambda}$ eigenvalues to define the *effective* range of $N^{\sigma \lambda}$.

Eventually, the set of states

$$|\Xi_i^{\sigma \lambda}\rangle \equiv \sum_{q=1}^{n_q} \frac{U_{qi}^{\sigma \lambda}}{\sqrt{s_i^{\sigma \lambda}}} P_{M0}^{\sigma} |\Phi^\lambda(q)\rangle , \quad (1.42)$$

for $i = 1, \dots, \check{r}^{\sigma \lambda}$ form an orthonormal basis of the working approximation to $\mathbf{E}_{n_q}^{\sigma \lambda}$. In the end, while $r^{\sigma \lambda}$ constitutes the dimension of $\mathbf{E}_{n_q}^{\sigma \lambda}$ in exact arithmetics, the truncation according to $\epsilon^{\sigma \lambda}$ delivers

$$n_{\check{r}^{\sigma \lambda}}^{\text{dim}} \equiv \check{r}^{\sigma \lambda} , \quad (1.43)$$

as the *effective* dimension of the working approximation to $\mathbf{E}_{n_q}^{\sigma \lambda}$.

1.8 Solving the Hill-Wheeler-Griffin equation

In order to solve the HWG equation, the projected hamiltonian kernels are transformed to the eigenbasis defined in Eq. (1.42) such that, for $1 \leq i, j \leq \check{r}^{\sigma \lambda}$,

$$\tilde{H}_{ij}^{\sigma \lambda} \equiv \langle \Xi_i^{\sigma \lambda} | H^\lambda | \Xi_j^{\sigma \lambda} \rangle \quad (1.44a)$$

$$= \sum_{q=1}^{n_q} \sum_{q'=1}^{n_q} \frac{U_{qi}^{\sigma \lambda} U_{q'j}^{\sigma \lambda}}{\sqrt{s_i^{\sigma \lambda} s_j^{\sigma \lambda}}} H_{qq'}^{\sigma \lambda} , \quad (1.44b)$$

thus forming the hermitian matrix to be diagonalized⁵, i.e. for arbitrary $1 \leq i \leq \check{r}^{\sigma\lambda}$ the HWG equation becomes

$$\sum_{j=1}^{\check{r}^{\sigma\lambda}} \tilde{H}_{ij}^{\sigma\lambda} X_{ja}^{\sigma\lambda} = E_a^{\sigma\lambda} X_{ia}^{\sigma\lambda}. \quad (1.45)$$

The PGCM states solutions of Eq. (1.45) can thus be written as

$$|\Theta_a^{\sigma\lambda}\rangle = \sum_{i=1}^{\check{r}^{\sigma\lambda}} X_{ia}^{\sigma\lambda} |\Xi_i^{\sigma\lambda}\rangle \quad (1.46a)$$

$$= \sum_{q=1}^{n_q} \left(\sum_{i=1}^{\check{r}^{\sigma\lambda}} X_{ia}^{\sigma\lambda} \frac{U_{qi}^{\sigma\lambda}}{\sqrt{S_i^{\sigma\lambda}}} \right) P_{M0}^{\sigma} |\Phi^\lambda(q)\rangle \quad (1.46b)$$

$$\equiv \sum_{q=1}^{n_q} f_a^{\sigma\lambda}(q) P_{M0}^{\sigma} |\Phi^\lambda(q)\rangle, \quad (1.46c)$$

such that the unknown PGCM state coefficients are solved according to

$$f_a^{\sigma\lambda}(q) = \sum_{i=1}^{\check{r}^{\sigma\lambda}} X_{ia}^{\sigma\lambda} \frac{U_{qi}^{\sigma\lambda}}{\sqrt{S_i^{\sigma\lambda}}}. \quad (1.47)$$

⁵Note that in Eq. (1.44a), the hermitian matrix is M -independent because of symmetry restoration.

Chapter 2

PGCM-EC

Contents

| | |
|---|-----------|
| 2.1 Eigenvector continuation technique | 29 |
| 2.1.1 Principle | 29 |
| 2.1.2 Over training | 31 |
| 2.2 Emulating the PGCM with EC | 31 |
| 2.3 PGCM-EC emulator algorithm | 32 |
| 2.3.1 Building blocks of the algorithm | 33 |

The goal of the present work is to use the eigenvector continuation (EC) technique [51, 50, 69, 52] to emulate (typically) millions of PGCM simulations at low computation cost. The objective is eventually to be able to perform sensitivity analyses on the interaction parameters and propagate their uncertainties to many-body observables. While absolute energies obtained from the PGCM are of interest in the EDF context, ab initio PGCM calculations focus on excitation energies of collective states and on the electromagnetic transitions linking them for reasons explained earlier on.

The present work concentrates on the ability of the EC to emulate a large number of PGCM simulations based on an appropriately chosen training set. To do so, absolute energies and radii of low-lying vibrational states in ^{20}Ne , along with associated excitation energies, computed from a simple Brink-Boecker effective interaction (see Sec. 4.1) are employed to validate the PGCM-EC emulators, as explained in Chap. 4. In order to be in position to perform such a study, the EC emulation of PGCM simulations, i.e. the formulation of the so-called PGCM-EC approach, is first detailed in the present chapter.

2.1 Eigenvector continuation technique

2.1.1 Principle

Let us consider the $n_T \equiv n_t n_a$ A-body solutions of Eq. (1.4)

$$T_{n_t n_a}^\sigma \equiv \left\{ |\Psi_0^\sigma(\lambda_1)\rangle, |\Psi_1^\sigma(\lambda_1)\rangle, \dots, |\Psi_{n_a-1}^\sigma(\lambda_1)\rangle, \dots, |\Psi_0^\sigma(\lambda_{n_t})\rangle, \dots, |\Psi_{n_a-1}^\sigma(\lambda_{n_t})\rangle \right\}, \quad (2.1)$$

obtained for n_t different parameter values belonging to the *training parameter set*

$$L_{n_t} \equiv \left\{ \lambda_1, \lambda_2, \dots, \lambda_{n_t} \right\}, \quad (2.2)$$

and including in each case the n_a lowest eigenstates belonging to a given IRREP. The set $T_{n_t n_a}^\sigma$ is referred to as the *training vector set*.

The EC technique is based on the fact that an eigenvector $|\Psi_\mu^\sigma(\lambda)\rangle$ of H^λ for an arbitrary parameter value λ is confined, to good approximation, to the low-dimensional subspace spanned by an appropriately chosen training set T_{n_t, n_a}^σ [51, 50, 69], i.e. $|\Psi_\mu^\sigma(\lambda)\rangle$ can be well approximated by a linear combination of the solutions $\{|\Psi_a^\sigma(\lambda_i)\rangle; 1 \leq i \leq n_t, 0 \leq a \leq n_a - 1\}$ obtained for the *snapshots* (i.e. training parameters) $\lambda_1, \dots, \lambda_{n_t}$

$$|\Psi_\mu^\sigma(\lambda)\rangle \approx \sum_{i=1}^{n_t} \sum_{a=0}^{n_a-1} g_{\mu ia}^{\bar{\sigma}\lambda} |\Psi_a^\sigma(\lambda_i)\rangle, \quad (2.3)$$

where the coefficients $g_{\mu ia}^{\bar{\sigma}\lambda}$ are to be variationally optimized. This is achieved by solving the secular equation corresponding to the diagonalization of H^λ in a low-dimensional non-orthogonal basis, i.e. for $i = 1, \dots, n_t$ and $a = 0, \dots, n_a - 1$

$$\sum_{j=1}^{n_t} \sum_{b=0}^{n_a-1} \langle \Psi_a^\sigma(\lambda_i) | H^\lambda | \Psi_b^\sigma(\lambda_j) \rangle g_{\mu jb}^{\bar{\sigma}\lambda} = \mathcal{E}_\mu^{\bar{\sigma}\lambda} \sum_{j=1}^{n_t} \sum_{b=0}^{n_a-1} \langle \Psi_a^\sigma(\lambda_i) | \Psi_b^\sigma(\lambda_j) \rangle g_{\mu jb}^{\bar{\sigma}\lambda}, \quad (2.4)$$

where $\mathcal{E}_\mu^{\bar{\sigma}\lambda}$ delivers an approximation to the target eigenvalue $E_\mu^{\bar{\sigma}}(\lambda)$. Equation (2.4) is formally similar to a HWG equation based on the norm kernel $\langle \Psi_a^\sigma(\lambda_i) | \Psi_b^\sigma(\lambda_j) \rangle$ and the Hamiltonian kernel $\langle \Psi_a^\sigma(\lambda_i) | H^\lambda | \Psi_b^\sigma(\lambda_j) \rangle$ involving the training vectors. Through Eq. (2.4), EC acts as an *emulator* of the exact A-body Schrodinger equation (1.4).

While solving a low-dimensional diagonalization problem (Eq. (2.4)) is extremely advantageous compared to solving Eq. (1.4) for H^λ , the cost of computing the $n_T(n_T + 1)/2$ Hamiltonian kernels can become prohibitive whenever repeating the process for a very large number of λ values, as is the case in the present application. In this context, the EC technique offers an extraordinary leverage whenever the Hamiltonian can be decomposed as a linear combination

$$H^\lambda = \sum_{k=1}^{n_p} f_k(\lambda) \check{H}_k, \quad (2.5)$$

where the n_p operators \check{H}_k are λ -independent and where $\{f_k(\lambda); k = 1, \dots, n_p\}$ denotes a set of functions of the original n_p parameters¹. Such an hypothesis is for example valid for the Gogny interaction (see Eq. (3.1)), provided the ranges (μ_1, μ_2) of the two gaussian functions are kept fixed, for the Brink-Boecker interaction (see Sec. 4.1) under the same hypothesis and for (most of the parameter dependence of) χ EFT Hamiltonians [53].

Assuming that Eq. (2.5) is satisfied, each Hamiltonian kernel entering Eq. (2.4) decomposes according to

$$\langle \Psi_a^\sigma(\lambda_i) | H^\lambda | \Psi_b^\sigma(\lambda_j) \rangle = \sum_{k=1}^{n_p} f_k(\lambda) \langle \Psi_a^\sigma(\lambda_i) | \check{H}_k | \Psi_b^\sigma(\lambda_j) \rangle. \quad (2.6)$$

such that Eq. (2.4) can be solved for an *arbitrary number* of λ realisations at the price of computing *only once* the $n_p \times n_T(n_T + 1)/2$ Hamiltonian kernels $\langle \Psi_i^\sigma | \check{H}_k | \Psi_j^\sigma \rangle$. This is extremely advantageous as the number of emulations becomes very large, i.e. $\gg n_p$.

¹For simplicity, the number of terms in Eq. (2.5) is assumed to be the same as the number of original parameters. If not, one can anyway redefine a set of n_p pertinent parameters via the functions $\{f_k(\lambda); k = 1, \dots, n_p\}$.

2.1.2 Over training

An interesting point concerns the result delivered by the EC emulator when applied to a training parameter, e.g. λ_1 . Considering the trial coefficients $g_{cjb}^{\tilde{\sigma}\lambda_1\text{trial}} = \delta_{j1}\delta_{bc}$, one obtains for $i = 1, \dots, n_t$ and $a = 0, \dots, n_a - 1$

$$\begin{aligned}
\sum_{j=1}^{n_t} \sum_{b=0}^{n_a-1} \langle \Psi_a^\sigma(\lambda_i) | H^{\lambda_1} | \Psi_b^\sigma(\lambda_j) \rangle g_{ajb}^{\tilde{\sigma}\lambda_1\text{trial}} &= \langle \Psi_a^\sigma(\lambda_i) | H^{\lambda_1} | \Psi_c^\sigma(\lambda_1) \rangle \\
&= E_c^{\tilde{\sigma}}(\lambda_1) \langle \Psi_a^\sigma(\lambda_i) | \Psi_c^\sigma(\lambda_1) \rangle \\
&= E_c^{\tilde{\sigma}}(\lambda_1) \sum_{j=1}^{n_t} \sum_{b=0}^{n_a-1} \langle \Psi_a^\sigma(\lambda_i) | \Psi_b^\sigma(\lambda_j) \rangle g_{ajb}^{\tilde{\sigma}\lambda_1\text{trial}}
\end{aligned} \tag{2.7}$$

which satisfies Eq. (2.4), i.e. the trial vector $|\Psi_c^\sigma(\lambda_1)\rangle$ is indeed a solution² of the emulator for the exact energy $\mathcal{E}_c^{\tilde{\sigma}\lambda_1} = E_c^{\tilde{\sigma}}(\lambda_1)$. Eventually, the above proves that, as long as the training vectors are exact solutions of Schrodinger's equation, the emulator employed with the corresponding Hamiltonian sends back the corresponding eigenvectors and eigenenergies.

In practice, however, EC is applied on the basis of *approximate* solutions of Schrodinger's equation delivered by a certain *simulator* one wishes to emulate. In this case, the above proof does not hold anymore such that the eigenenergies delivered by the emulator are accompanied with an error, *even* when employed for a training parameter. In particular, the emulated *ground-state* energy associated with a given training value will be *lower* than the reference value originally delivered by the simulator. Indeed, the EC ansatz in Eq. (2.3) can only variationally improve the approximate solution delivered by the simulator such that one speaks about an intrinsic *over training* of the emulator in such a case.

It is thus mandatory to first quantify the intrinsic over training of the emulator given that one can expect the associated error to be a lower bound of the error accessible when emulating solutions that are not in $T_{n_t n_a}^\sigma$, which is eventually the goal of the emulator.

2.2 Emulating the PGCM with EC

Eigenvector continuation is now specified to emulate PGCM calculations, i.e. the PGCM simulator is to be approximated at low computational cost by the PGCM-EC emulator. In this context, the training vectors are PGCM states (see Eq. (1.6)) corresponding to a given $\sigma = (\tilde{\sigma}, M)$

$$|\Theta_a^{\sigma\lambda_i}\rangle = \sum_{q \in \mathcal{S}} f_a^{\tilde{\sigma}\lambda_i}(q) P_{M0}^{\tilde{\sigma}} |\Phi^{\lambda_i}(q)\rangle, \tag{2.8}$$

with $a = 0, \dots, n_a - 1$, such that the training set is given by

$$T_{n_t n_a}^\sigma \equiv \left\{ |\Theta_a^{\sigma\lambda_i}\rangle ; i = 1, \dots, n_t \text{ and } a = 0, \dots, n_a - 1 \right\}, \tag{2.9}$$

the number of training vectors thus being

$$n_T = n_t n_a. \tag{2.10}$$

²The proof works for any of the n_a training vectors associated with H^{λ_1} whereas the $n_T - n_a$ other solutions obtained from the EC emulator carry no obvious meaning. Based on the Ritz variational principle, it is easy to prove that the ground-state energy $E_0^{\tilde{\sigma}}(\lambda_1)$, if $|\Psi_0^\sigma(\lambda_1)\rangle$ is indeed in the training set, is the lowest eigenvalue delivered by the emulator. Contrarily, one cannot anticipate to which solutions of the emulator the $n_a - 1$ other training vectors associated with H^{λ_1} correspond to. Eventually, the process can be repeated for $H^{\lambda_2}, \dots, H^{\lambda_{n_t}}$ to recover the complete set of training vectors from the emulator.

Given $T_{n_t n_a}^\sigma$, the $n_p \times n_T(n_T + 1)/2$ Hamiltonian kernels (and $n_T(n_T + 1)/2$ norm kernels) needed to apply EC are expanded in terms of **elementary projected kernels**

$$\langle \Theta_a^{\sigma \lambda_i} | \Theta_b^{\sigma \lambda_j} \rangle = \sum_{q \in S} \sum_{q' \in S} f_a^{\sigma \lambda_i^*}(q) f_b^{\sigma \lambda_j}(q') \langle \Phi^{\lambda_i}(\mathbf{q}) | \mathbf{P}_{00}^{\bar{\sigma}} | \Phi^{\lambda_j}(\mathbf{q}') \rangle, \quad (2.11a)$$

$$\langle \Theta_a^{\sigma \lambda_i} | \check{H}_k | \Theta_b^{\sigma \lambda_j} \rangle = \sum_{q \in S} \sum_{q' \in S} f_a^{\sigma \lambda_i^*}(q) f_b^{\sigma \lambda_j}(q') \langle \Phi^{\lambda_i}(\mathbf{q}) | \check{H}_k \mathbf{P}_{00}^{\bar{\sigma}} | \Phi^{\lambda_j}(\mathbf{q}') \rangle, \quad (2.11b)$$

where the commutation of the projection operator $P_{M0}^{\bar{\sigma}^\dagger}$ with \check{H}_k and the identity $P_{M0}^{\bar{\sigma}^\dagger} P_{M0}^{\bar{\sigma}} = P_{0M}^{\bar{\sigma}} P_{M0}^{\bar{\sigma}} = P_{00}^{\bar{\sigma}}$ have been used. Following Eq. (1.14), these elementary projected kernels can in turn be expanded in terms of **elementary generalized off-diagonal overlaps**

$$N_{qq'}^{\bar{\sigma} \lambda_i \lambda_j} \equiv \langle \Phi^{\lambda_i}(q) | P_{00}^{\bar{\sigma}} | \Phi^{\lambda_j}(q') \rangle = \frac{d_\sigma^2}{v_G^2} \sum_{\theta} D_{00}^{\bar{\sigma}^*}(\theta) \langle \Phi^{\lambda_i}(\mathbf{q}) | \Phi^{\lambda_j}(\mathbf{q}'; \theta) \rangle, \quad (2.12a)$$

$$\check{H}_{qq'}^{\bar{\sigma} \lambda_i \lambda_j k} \equiv \langle \Phi^{\lambda_i}(q) | \check{H}_k P_{00}^{\bar{\sigma}} | \Phi^{\lambda_j}(q') \rangle = \frac{d_\sigma^2}{v_G^2} \sum_{\theta} D_{00}^{\bar{\sigma}^*}(\theta) \langle \Phi^{\lambda_i}(\mathbf{q}) | \check{H}_k | \Phi^{\lambda_j}(\mathbf{q}'; \theta) \rangle. \quad (2.12b)$$

Eventually, building the PGCM-EC emulator reduces to the computation of the set of elementary generalized off-diagonal norm and Hamiltonian overlaps

$$N^{\lambda_i \lambda_j}(q, q'; \theta) \equiv \langle \Phi^{\lambda_i}(q) | \Phi^{\lambda_j}(q'; \theta) \rangle, \quad (2.13a)$$

$$\check{h}^{\lambda_i \lambda_j k}(q, q'; \theta) \equiv \frac{\langle \Phi^{\lambda_i}(q) | \check{H}_k | \Phi^{\lambda_j}(q'; \theta) \rangle}{\langle \Phi^{\lambda_i}(q) | \Phi^{\lambda_j}(q'; \theta) \rangle}, \quad (2.13b)$$

which are of identical nature to those already involved in actual PGCM calculations while extending them in two ways. First, their *generalized* character relates to the fact that they are now also of off-diagonal nature with respect to the parameter values λ_i and λ_j , i.e. the overlaps involving all HFB states originating from the n_t different PGCM simulations performed during the training phase must be computed to build the emulator³. Second, the *elementary* character of the reduced off-diagonal Hamiltonian overlaps $\check{h}^{\lambda_i \lambda_j k}(q, q'; \theta)$ relates to the fact that such overlaps must be computed for each of the n_p parameter-independent⁴ operators \check{H}_k rather than for the full Hamiltonian as is done in traditional PGCM calculations. In any case, the overlaps defined in Eq. (2.13) can be straightforwardly computed from the technology already available from the PGCM simulator. Elementary generalized hamiltonian kernels are illustrated in Fig. 2.1.

2.3 PGCM-EC emulator algorithm

Given a Hamiltonian model H^λ satisfying Eq. (2.5), one chooses

- a parameter mesh $L_n = \{\lambda_1, \lambda_2, \dots, \lambda_n\}$,
- a generator coordinate mesh $S = \{q_1, q_2, \dots, q_{n_q}\}$.

Based on these two meshes, constrained HFB equations are solved repeatedly to generate

$$|\Phi^{\lambda_i}(q)\rangle \text{ for } i = 1, \dots, n \text{ and } q \in S, \quad (2.14)$$

³Overlaps that are diagonal with respect to parameter values are thus already available from the training phase, i.e. one only needs to further compute the off-diagonal blocks of the super overlap matrices with respect to the parameter indices.

⁴The key points is that those kernels only depend on the *training* parameters via the bra and ket but *not* on the parameter λ associated with the PGCM states one wishes to emulate.

| | λ_0 | λ_1 | λ_2 |
|-------------|---|---|---|
| λ_0 | $\frac{\langle \Phi^{\lambda_0}(q) \check{H}_k \Phi^{\lambda_0}(q'; \theta) \rangle}{\langle \Phi^{\lambda_0}(q) \Phi^{\lambda_0}(q'; \theta) \rangle}$ | $\frac{\langle \Phi^{\lambda_0}(q) \check{H}_k \Phi^{\lambda_1}(q'; \theta) \rangle}{\langle \Phi^{\lambda_0}(q) \Phi^{\lambda_1}(q'; \theta) \rangle}$ | $\frac{\langle \Phi^{\lambda_0}(q) \check{H}_k \Phi^{\lambda_2}(q'; \theta) \rangle}{\langle \Phi^{\lambda_0}(q) \Phi^{\lambda_2}(q'; \theta) \rangle}$ |
| λ_1 | $\frac{\langle \Phi^{\lambda_1}(q) \check{H}_k \Phi^{\lambda_0}(q'; \theta) \rangle}{\langle \Phi^{\lambda_1}(q) \Phi^{\lambda_0}(q'; \theta) \rangle}$ | $\frac{\langle \Phi^{\lambda_1}(q) \check{H}_k \Phi^{\lambda_1}(q'; \theta) \rangle}{\langle \Phi^{\lambda_1}(q) \Phi^{\lambda_1}(q'; \theta) \rangle}$ | $\frac{\langle \Phi^{\lambda_1}(q) \check{H}_k \Phi^{\lambda_2}(q'; \theta) \rangle}{\langle \Phi^{\lambda_1}(q) \Phi^{\lambda_2}(q'; \theta) \rangle}$ |
| λ_2 | $\frac{\langle \Phi^{\lambda_2}(q) \check{H}_k \Phi^{\lambda_0}(q'; \theta) \rangle}{\langle \Phi^{\lambda_2}(q) \Phi^{\lambda_0}(q'; \theta) \rangle}$ | $\frac{\langle \Phi^{\lambda_2}(q) \check{H}_k \Phi^{\lambda_1}(q'; \theta) \rangle}{\langle \Phi^{\lambda_2}(q) \Phi^{\lambda_1}(q'; \theta) \rangle}$ | $\frac{\langle \Phi^{\lambda_2}(q) \check{H}_k \Phi^{\lambda_2}(q'; \theta) \rangle}{\langle \Phi^{\lambda_2}(q) \Phi^{\lambda_2}(q'; \theta) \rangle}$ |

Figure 2.1: Schematic illustration of elementary generalized hamiltonian kernels, organised with respect to parameter values λ_i , diagonal kernels needed for sole PGCM computations are highlighted in green, and additional off-diagonal kernels also needed for the emulator are highlighted in purple. In this figure, $n_t = 3$.

before computing the elementary projected kernels (in practice stored in a file)

$$N_{qq'}^{\bar{\sigma}\lambda_i\lambda_j} = \langle \Phi^{\lambda_i}(q) | P_{00}^{\bar{\sigma}} | \Phi^{\lambda_j}(q') \rangle, \quad (2.15a)$$

$$\check{H}_{qq'}^{\bar{\sigma}\lambda_i\lambda_jk} = \langle \Phi^{\lambda_i}(q) | \check{H}_k P_{00}^{\bar{\sigma}} | \Phi^{\lambda_j}(q') \rangle, \quad (2.15b)$$

for $i, j = 1, \dots, n$ and $q, q' \in S$, as well as $k = 1, \dots, n_p$.

2.3.1 Building blocks of the algorithm

The PGCM-EC algorithm have three basic building blocks, that are ultimately assembled differently, depending on the computation to be done (either a PGCM computation, or a PGCM-EC emulation). There are three types of building block.

TYPE 1 building block

a TYPE 1 building block takes as inputs an index $1 \leq \alpha \leq n$, a threshold value $\epsilon^{\bar{\sigma}\alpha} > 0$.

First, the projected norm and Hamiltonian matrices

$$N^{\bar{\sigma}\alpha} \equiv N^{\bar{\sigma}\lambda_\alpha\lambda_\alpha}, \quad (2.16a)$$

$$\check{H}^{\bar{\sigma}\alpha k} \equiv \check{H}^{\bar{\sigma}\lambda_\alpha\lambda_\alpha k}, \quad (2.16b)$$

are extracted from the precomputed elementary projected kernels data.

Second, the norm matrix is diagonalized according to

$$N^{\bar{\sigma}\alpha} X^{\bar{\sigma}\alpha} = \Lambda^{\bar{\sigma}\alpha} X^{\bar{\sigma}\alpha}, \quad (2.17)$$

with $\Lambda^{\bar{\sigma}\alpha}$ a diagonal matrix

$$\Lambda^{\bar{\sigma}\alpha} \equiv \text{diag}(s_1^{\bar{\sigma}\alpha}, s_2^{\bar{\sigma}\alpha}, \dots, s_{n_q}^{\bar{\sigma}\alpha}), \quad (2.18a)$$

$$0 \leq s_1^{\tilde{\sigma}\alpha} \leq \dots \leq s_{n_q}^{\tilde{\sigma}\alpha}, \quad (2.18b)$$

and $X^{\tilde{\sigma}\alpha}$ a $n_q \times n_q$ unitary matrix. Eigenvalues smaller than a chosen threshold $\epsilon^{\tilde{\sigma}\alpha}$

$$s_{\tilde{r}^{\tilde{\sigma}\alpha}-1}^{\tilde{\sigma}\alpha} < \epsilon^{\tilde{\sigma}\alpha} \leq s_{\tilde{r}^{\tilde{\sigma}\alpha}}^{\tilde{\sigma}\alpha}, \quad (2.19)$$

are discarded such that matrices $\Lambda^{\tilde{\sigma}\alpha}$ and $X^{\tilde{\sigma}\alpha}$ are effectively replaced by⁵

$$\tilde{\Lambda}^{\tilde{\sigma}\alpha} \equiv \text{diag}(s_{\tilde{r}^{\tilde{\sigma}\alpha}}^{\tilde{\sigma}\alpha}, s_{\tilde{r}^{\tilde{\sigma}\alpha}+1}^{\tilde{\sigma}\alpha}, \dots, s_{n_q}^{\tilde{\sigma}\alpha}), \quad (2.20a)$$

$$\tilde{X}^{\tilde{\sigma}\alpha} \equiv X^{\tilde{\sigma}\alpha} [1 : n_q, \tilde{r}^{\tilde{\sigma}\alpha} : n_q]. \quad (2.20b)$$

Next the matrix

$$Y^{\tilde{\sigma}\alpha} \equiv \tilde{X}^{\tilde{\sigma}\alpha} (\tilde{\Lambda}^{\tilde{\sigma}\alpha})^{-\frac{1}{2}}, \quad (2.21)$$

such that the orthonormal basis states of the approximation to $E_{n_q}^{\sigma\lambda\alpha}$ read as

$$|\Xi_j^{\sigma\lambda\alpha}\rangle = \sum_{i=1}^{n_q} Y_{ij}^{\tilde{\sigma}\alpha} P_{M0}^{\tilde{\sigma}\alpha} |\Phi^{\lambda\alpha}(q_i)\rangle, \quad (2.22)$$

for every

$$1 \leq j \leq d^{\tilde{\sigma}\alpha} \equiv n_q - \tilde{r}^{\tilde{\sigma}\alpha} + 1.$$

Third, the projected Hamiltonian matrices are transformed into new orthonormal basis according to

$$\tilde{H}_{ij}^{\tilde{\sigma}\alpha k} \equiv \langle \Xi_i^{\sigma\lambda\alpha} | \check{H}_k | \Xi_j^{\sigma\lambda\alpha} \rangle = \left((Y^{\tilde{\sigma}\alpha})^\dagger \check{H}^{\tilde{\sigma}\alpha k} Y^{\tilde{\sigma}\alpha} \right)_{ij}, \quad (2.23)$$

for every $1 \leq i, j \leq \tilde{r}^{\tilde{\sigma}\alpha}$. The situation may be represented schematically⁶ as in Fig. 1

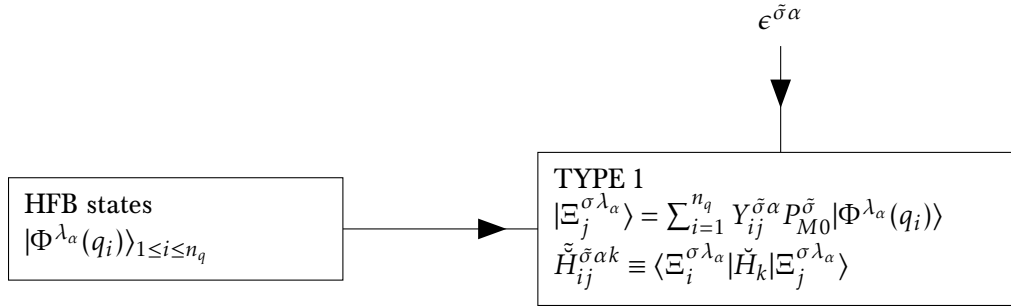


Figure 1 . Schematic representation of a TYPE 1 building block.

TYPE 2 building block

A TYPE 2 building block takes as inputs TYPE 1 or TYPE 3 building block, and a parametrisation μ . First the total $r \times r$ Hamiltonian matrix is constructed

$$\tilde{H}^{\tilde{\sigma}\mu} = \sum_{k=1}^{n_p} f_k(\mu) \tilde{H}^{\tilde{\sigma}k}. \quad (2.24)$$

where one has either⁷

⁵For a matrix A , $A[p_1 : p_2, q_1 : q_2]$ denotes the submatrix obtained by extracting $p_2 - p_1 + 1$ rows between p_1 and p_2 , and $q_2 - q_1 + 1$ columns between q_1 and q_2 .

⁶Flowchart in this chapter as well as geometrical figures in chapter 6 are constructed with the Fig4Tex macro package [70].

⁷The notation for $\tilde{H}^{\tilde{\sigma}\mu}$ and $\tilde{H}^{\tilde{\sigma}k}$ does not specify the parameter(s) characterizing the bra and ket in order to remain generic and valid for both TYPE 1 or TYPE 3 inputs.

- $\tilde{H}^{\tilde{\sigma}k} \equiv \tilde{H}^{\tilde{\sigma}\alpha k}$ if constructed from TYPE 1, in which case $r = d^{\tilde{\sigma}\alpha}$,
- $\tilde{H}^{\tilde{\sigma}k} \equiv \tilde{H}'^{\tilde{\sigma}k}$ if constructed from TYPE 3, in which case $r = d^{\tilde{\sigma}}$.

The total Hamiltonian matrix $\tilde{H}^{\tilde{\sigma}\mu}$ is then diagonalized according to

$$\tilde{H}^{\tilde{\sigma}\mu} Z^{\tilde{\sigma}\mu} = E^{\tilde{\sigma}\mu} Z^{\tilde{\sigma}\mu}, \quad (2.25)$$

with $E^{\tilde{\sigma}\mu}$ a diagonal matrix, and $Z^{\tilde{\sigma}\mu}$ the unitary matrix whose columns are eigenvectors of $\tilde{H}^{\tilde{\sigma}\mu}$

$$E^{\tilde{\sigma}\mu} = \text{diag}(E_1^{\tilde{\sigma}\mu}, \dots, E_r^{\tilde{\sigma}\mu}), \quad (2.26a)$$

$$Z^{\tilde{\sigma}\mu} (Z^{\tilde{\sigma}\mu})^\dagger = (Z^{\tilde{\sigma}\mu})^\dagger Z^{\tilde{\sigma}\mu} = 1_r. \quad (2.26b)$$

The situation may be represented schematically as displayed in Fig. 2

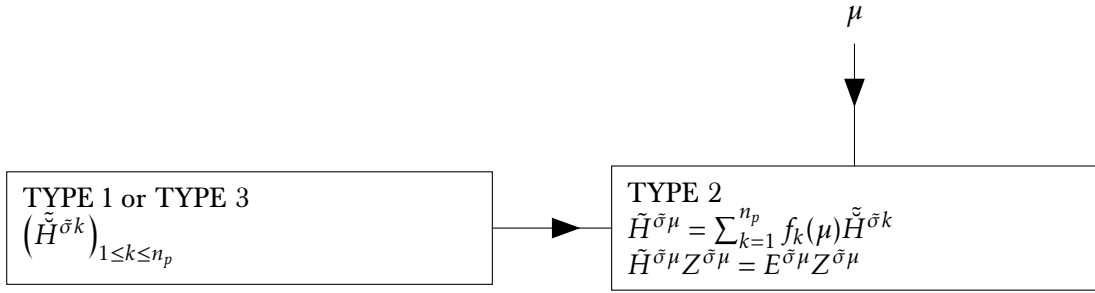


Figure 2. Schematic representation of a TYPE 2 building block.

The process can be exemplified for a PGCM simulation based on the Hamiltonian H^{λ_α} , i.e. when ever using a TYPE 1 building block as an input such that

$$\tilde{H}^{\tilde{\sigma}k} \equiv \tilde{H}^{\tilde{\sigma}\alpha k} \quad (2.27)$$

from Eq. (2.23) and such that the entire process can be schematically described as displayed in Fig. 3

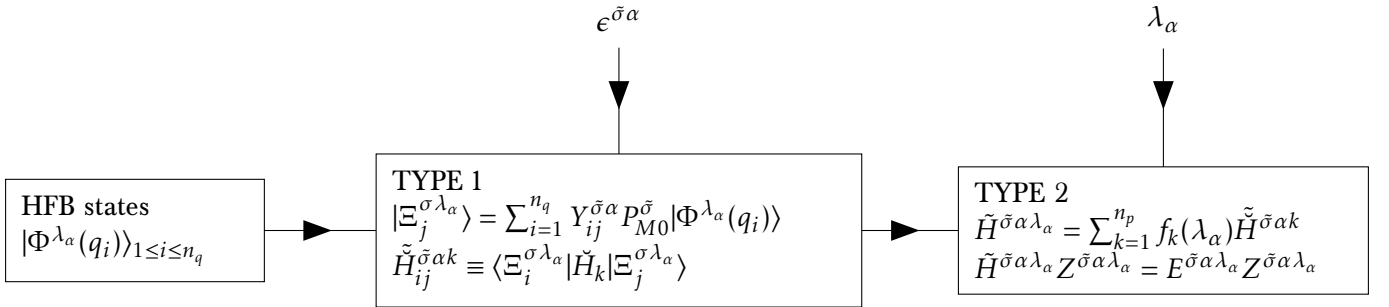


Figure 3. Schematic representation of a PGCM simulation based on the Hamiltonian H^{λ_α} .

TYPE 3 building block

A TYPE 3 building block takes as inputs a threshold $\epsilon_t^{\tilde{\sigma}} > 0$, the integer $n_a \geq 1$ and a set of TYPE 2 building blocks constructed from TYPE 1 building blocks for each parameter value of the training set $L_{n_t} \subset L_n$ ⁸. The set of PGCM training vector is thus given by

$$T_{n_a n_q}^{\sigma L_{n_t}} = \left\{ |\Theta_a^{\sigma \lambda_{\alpha_m}} \rangle ; m = 1, \dots, n_t \text{ and } a = 0, \dots, n_a - 1 \right\}, \quad (2.28)$$

⁸In PGCM-EC applications discussed in the present work, one constructs the training set L_{n_t} from a subset of L_n , the complementary part of the latter being used as a *validation* set against reference PGCM simulations.

with

$$|\Theta_a^{\sigma\lambda_{\alpha_m}}\rangle = \sum_{i=1}^{\check{r}^{\sigma\lambda_{\alpha_m}}} Z_{ia}^{\tilde{\sigma}\alpha_m\lambda_{\alpha_m}} |\Xi_i^{\sigma\lambda_{\alpha_m}}\rangle. \quad (2.29)$$

For each couple $1 \leq m, n \leq n_t$, the projected kernels $N_{qq'}^{\tilde{\sigma}\lambda_m\lambda_n}$ and $\check{H}_{qq'}^{\tilde{\sigma}\lambda_m\lambda_n k}$ from Eq. (2.15) are extracted from precomputed elementary projected kernels data, in order to compute, for $0 \leq a, b \leq n_a$, the kernels between the PGCM training vectors needed to apply EC

$$\langle \Theta_a^{\sigma\lambda_{\alpha_m}} | \Theta_b^{\sigma\lambda_{\alpha_n}} \rangle = \left(\left(Z^{\tilde{\sigma}\alpha_m\lambda_{\alpha_m}} \right)^\dagger \left(Y^{\tilde{\sigma}\alpha_m} \right)^\dagger N^{\tilde{\sigma}\lambda_m\lambda_n} Y^{\tilde{\sigma}\alpha_n} Z^{\tilde{\sigma}\alpha_n\lambda_{\alpha_n}} \right)_{ab}, \quad (2.30a)$$

$$\langle \Theta_a^{\sigma\lambda_{\alpha_m}} | \check{H}^k | \Theta_b^{\sigma\lambda_{\alpha_n}} \rangle = \sum_{i=1}^{\check{r}^{\sigma\lambda_{\alpha_m}}} \sum_{j=1}^{\check{r}^{\sigma\lambda_{\alpha_n}}} \left(Z_{ia}^{\tilde{\sigma}\alpha_m\lambda_{\alpha_m}} \right)^\dagger Z_{jb}^{\tilde{\sigma}\alpha_n\lambda_{\alpha_n}} \langle \Xi_i^{\sigma\lambda_{\alpha_m}} | \check{H}^k | \Xi_j^{\sigma\lambda_{\alpha_n}} \rangle \quad (2.30b)$$

$$= \sum_{i=1}^{\check{r}^{\sigma\lambda_{\alpha_m}}} \sum_{j=1}^{\check{r}^{\sigma\lambda_{\alpha_n}}} \sum_{q=1}^{n_q} \sum_{q'=1}^{n_q} \left(Z_{ia}^{\tilde{\sigma}\alpha_m\lambda_{\alpha_m}} \right)^\dagger Z_{jb}^{\tilde{\sigma}\alpha_n\lambda_{\alpha_n}} \left(Y_{qi}^{\tilde{\sigma}\alpha_m} \right)^\dagger Y_{q'j}^{\tilde{\sigma}\alpha_n} \check{H}_{qq'}^{\tilde{\sigma}\lambda_m\lambda_n k} \quad (2.30c)$$

$$= \left(\left(Z^{\tilde{\sigma}\alpha_m\lambda_{\alpha_m}} \right)^\dagger \left(Y^{\tilde{\sigma}\alpha_m} \right)^\dagger \check{H}^{\tilde{\sigma}\lambda_m\lambda_n k} Y^{\tilde{\sigma}\alpha_n} Z^{\tilde{\sigma}\alpha_n\lambda_{\alpha_n}} \right)_{ab}. \quad (2.30d)$$

Following the computation of these kernels, the associated super norm matrix

$$N_{ma \ nb}^{\tilde{\sigma}} \equiv \langle \Theta_a^{\sigma\lambda_{\alpha_m}} | \Theta_b^{\sigma\lambda_{\alpha_n}} \rangle, \quad (2.31)$$

is diagonalized, while keeping eigenvalues above the super threshold $\epsilon_t^{\tilde{\sigma}}$, to build the orthonormal basis, with $1 \leq i \leq d'^{\tilde{\sigma}}$

$$|\Xi_i'^{\sigma}\rangle \equiv \sum_{ma} Y_{i(ma)}'^{\tilde{\sigma}} |\Theta_a^{\sigma M\lambda_{\alpha_m}}\rangle, \quad (2.32)$$

of the approximation to the training PGCM subspace $E_{n_q}^{\sigma L_{n_t}}$. Eventually, the super elementary Hamiltonian matrices are computed according to

$$\check{H}_{ij}'^{\tilde{\sigma}k} \equiv \langle \Xi_i'^{\sigma} | \check{H}^k | \Xi_j'^{\sigma} \rangle, \quad (2.33)$$

and stored within the HWG object of TYPE 3 type. This ends the construction of considered TYPE 3 building block.

The trained emulator thus obtained can then be used to emulate the PGCM simulation associated with any new parameter μ by using the super elementary Hamiltonian matrices as inputs to the TYPE 2 building block described above. The workflow elaborated in this section can be schematized for $n_t = 3$ as displayed in Fig. 4

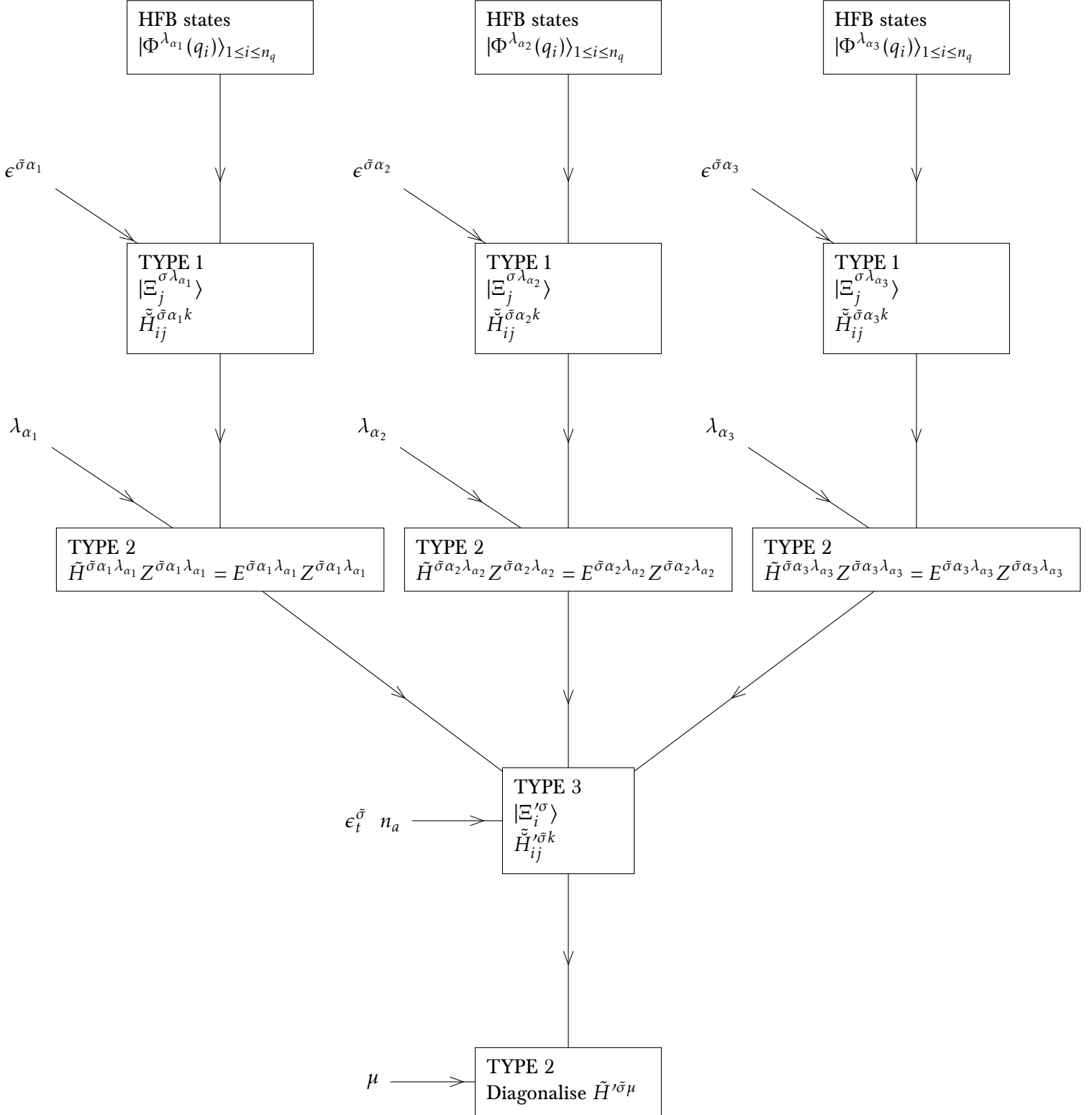


Figure 4. Schematic representation of a PGCM-EC emulation for $n_t = 3$.

Chapter 3

Interaction

Contents

| | |
|---|-----------|
| 3.1 Gogny pseudo-potential | 40 |
| 3.2 Basis functions | 41 |
| 3.2.1 Orthonormality relations | 42 |
| 3.2.2 Talman coefficients | 42 |
| 3.2.3 Moshinsky coefficients | 42 |
| 3.3 Calculation of matrix elements | 43 |
| 3.3.1 Central term | 43 |
| 3.3.2 Coulomb term | 44 |
| 3.3.3 Two-body center of mass correction | 44 |
| 3.3.4 Density term | 45 |
| 3.3.5 Spin-orbit term | 46 |

The current paradigm of *ab initio* nuclear theory constructs the nuclear Hamiltonian as a χ EFT expansion of QCD. The number of terms entering this expansion grows quickly with the order in the χ EFT expansion and requires the introduction of numerous low-energy constants (LECs).

In order to assess the performance of the PGCM-EC emulator for the sensitivity analysis, it is interesting to first perform a preliminary study with a simpler interaction that contains less parameters and only two-body terms. To do so, non-relativistic phenomenological interactions used with success over the last decades offer an interesting testing ground. They are usually declined into two families: zero- (Skyrme [71]) and finite-range (Gogny [72]). However, these phenomenological interactions require (for an accurate description of both radii and binding energies in all nuclei) the introduction of a density-dependent term (effectively compensating in particular for the lack of three-body terms in the Hamiltonian) that disqualifies their interpretation as true Hamiltonian. These pseudo-Hamiltonians have proven versatile for mean-field calculations over the whole nuclear chart, but they cannot be safely used in multi-reference methods such as the (P)GCM [73, 74, 75].

The above considerations motivated the use of the simple Brink-Boeker [76] two-body interaction in the present study; see Chap. 4 for the definition of the model case presently employed to characterize the performance of the PGCM-EC emulator. While the terms contained in the Brink-Boeker are a subset of those appearing in the Gogny interaction, there is no density-dependent term such that the Brink-Boeker does qualify as a true Hamiltonian and can thus be safely used in (P)GCM calculations.

For the sake of generality, and future investigations, all matrix elements of the Gogny interaction have been re-derived and implemented in the PAN@CEA numerical solver. The corresponding derivations and the associated set of final formulas are reported in the present chapter.

| i | μ_i fm | W_i MeV | B_i MeV | H_i MeV | M_i MeV | t_0 MeV.fm $^{3(\alpha_G+1)}$ | x_0 | α_G | W_{LS} MeV.fm 5 |
|-----|---------------|--------------|--------------|--------------|--------------|------------------------------------|-------|------------|-------------------------|
| 1 | 0.7 | 1720.30 | 1300.0 | -18013.53 | 1397.6 | 1390.6 | 1 | 1/3 | 130 |
| 2 | 1.2 | 103.639 | -163.483 | 162.812 | -223.933 | | | | |

Table 3.1: DIS parametrization of the Gogny effective interaction.

3.1 Gogny pseudo-potential

The Gogny pseudo-potential is an example of a density-dependent interaction giving rise to a pseudo-Hamiltonian and then a pseudo-potential. The Gogny pseudo-potential is given by (see Ref. [77], Eq. (1.30))

$$V_{DIS}(\mathbf{R}, \mathbf{r}) \equiv \sum_{i=1}^2 \left[W_i + B_i \hat{P}_s - H_i \hat{P}_t - M_i \hat{P}_s \hat{P}_t \right] e^{-\mathbf{r}^2/\mu_i^2} \quad (3.1a)$$

$$+ \frac{q^2}{|\mathbf{r}|} \quad (3.1b)$$

$$- \frac{\mathbf{P}_1 \cdot \mathbf{P}_2}{m\langle A \rangle} \quad (3.1c)$$

$$+ t_0 \left(1 + \chi_0 \hat{P}_s \right) \rho^{\alpha_G}(\mathbf{R}) \delta(\mathbf{r}) \quad (3.1d)$$

$$+ i W_{LS} (\boldsymbol{\sigma}_1 + \boldsymbol{\sigma}_2) \cdot \overleftarrow{\mathbf{k}}' \times \delta(\mathbf{r}) \overrightarrow{\mathbf{k}} \quad (3.1e)$$

$$\equiv V^C + V^{\text{Coul}} + V^{\text{COM2}} + V^D + V^{\text{SO}} , \quad (3.1f)$$

where

$$\mathbf{r} \equiv \mathbf{r}_1 - \mathbf{r}_2, \quad (3.2a)$$

$$\mathbf{R} \equiv \frac{\mathbf{r}_1 + \mathbf{r}_2}{2}, \quad (3.2b)$$

$$\hat{P}_s \equiv \frac{1}{2} (1 + \boldsymbol{\sigma}_1 \cdot \boldsymbol{\sigma}_2), \quad (3.2c)$$

$$\hat{P}_t \equiv \frac{1}{2} (1 + \boldsymbol{\tau}_1 \cdot \boldsymbol{\tau}_2), \quad (3.2d)$$

$$\overrightarrow{\mathbf{k}} \equiv -\frac{i}{2} (\overrightarrow{\nabla}_1 - \overrightarrow{\nabla}_2), \quad (3.2e)$$

$$\overleftarrow{\mathbf{k}}' \equiv -\left(\overrightarrow{\mathbf{k}}\right)^\dagger = -\frac{i}{2} (\overleftarrow{\nabla}_1 - \overleftarrow{\nabla}_2) , \quad (3.2f)$$

and $W_{1,2}$, $B_{1,2}$, $H_{1,2}$, $M_{1,2}$, $\mu_{1,2}$, t_0 , χ_0 , α , and W_{LS} are free parameters. Several parametrizations of the Gogny interactions have been established and tested in the nuclear community. In particular, the DIS parametrization ([78], chapter 2) of the Gogny interaction is reported in Tab. 3.1.

The corresponding two-body matrix elements are given by

$$\begin{aligned} v_{\alpha\beta\gamma\delta}[\rho] &= \langle 1 : \alpha ; 2 : \beta | V | 1 : \gamma ; 2 : \delta \rangle \\ &= \sum_{\nu_1 \nu_2 \nu_3 \nu_4} \int d^3 r_1 d^3 r_2 d^3 r_3 d^3 r_4 \end{aligned}$$

$$\begin{aligned}
& \times \langle 1 : \alpha ; 2 : \beta | \mathbf{r}_1, \nu_1 ; \mathbf{r}_2, \nu_2 \rangle \\
& \times \langle \mathbf{r}_1, \nu_1 ; \mathbf{r}_2, \nu_2 | V | \mathbf{r}_3, \nu_3 ; \mathbf{r}_4, \nu_4 \rangle \\
& \times \langle \mathbf{r}_3, \nu_3 ; \mathbf{r}_4, \nu_4 | 3 : \gamma ; 4 : \delta \rangle .
\end{aligned} \tag{3.3}$$

Here $|\psi_\alpha\rangle$ is a yet unspecified basis of \mathcal{H}_1 , and $\nu \equiv (\text{spin, isospin})$. The density dependence of V is characteristic of a pseudo-hamiltonian. The associated pseudo-Hamiltonian is

$$H_{\text{eff}}[\rho] \equiv \sum_{\alpha\beta\gamma\delta} V_{\alpha\beta\gamma\delta}[\rho] a_\alpha^\dagger a_\beta^\dagger a_\delta a_\gamma, \tag{3.4}$$

with a_α^\dagger the creation operator creating a particle in the single-particle state ϕ_α . Note that the Gogny pseudo-hamiltonian is κ and $\bar{\kappa}$ independent.

3.2 Basis functions

In principle, the nuclear problem is independent of the choice of the basis of the one-body Hilbert space. In practice, truncations imposed by numerical limitations suggest to use functions that are well-localized in order to describe nuclei at a reasonable cost. Amongst localized bases, harmonic oscillator wave-functions happen to be extremely useful given that matrix elements of the Gaussian terms entering the interaction can be easily expressed analytically using such basis function as is shown below. In the present work, axial harmonic oscillator wave functions ([78], chapter 2) are employed and read as

$$\psi_{m n n_z}(\mathbf{r}; b_r, b_z) \equiv \psi_{m n}^{(2)}(r, \varphi; b_r) \psi_{n_z}^{(1)}(z; b_z) \tag{3.5a}$$

$$\equiv \chi_n^{|m|}(r; b_r) \frac{e^{im\varphi}}{\sqrt{2\pi}} \psi_{n_z}^{(1)}(z; b_z) \tag{3.5b}$$

$$\equiv e^{im\varphi} \tilde{\psi}_{nmz}(r, z; b_r, b_z) \tag{3.5c}$$

where m is the orbital angular momentum z -component, n_z and n are both non-negative integers, and b_r, b_z are positive numbers with unit of length. By definition, $r \equiv \sqrt{x^2 + y^2}$ and $(x, y) = (r \cos \varphi, r \sin \varphi)$. For $m \in \mathbb{Z}, n \in \mathbb{N}$, one has

$$\chi_n^{|m|}(r; b_r) \equiv N_n^{|m|}(b_r) e^{-\frac{r^2}{2b_r^2}} \left(\frac{r}{b_r}\right)^{|m|} L_n^{|m|}\left(\frac{r^2}{b_r^2}\right), \tag{3.6a}$$

$$\psi_{n_z}^{(1)}(z; b_z) \equiv N_{n_z}(b_z) e^{-\frac{z^2}{2b_z^2}} H_{n_z}\left(\frac{z}{b_z}\right), \tag{3.6b}$$

where the normalisations are given by

$$N_n^{|m|}(b_r) \equiv \frac{\sqrt{2}}{b_r} \sqrt{\frac{n!}{(n+|m|)!}}, \tag{3.7a}$$

$$N_{n_z}(b_z) \equiv \frac{1}{\sqrt{b_z}} \sqrt{\frac{1}{2^{n_z} n_z! \sqrt{\pi}}}, \tag{3.7b}$$

and where L_n^k, H_n are generalized Laguerre and Hermite polynomials respectively. As already mentioned, these functions are eigenfunctions of the axially deformed harmonic oscillator

$$\left(-\frac{\hbar^2}{2M} \frac{d^2}{dz^2} + \frac{1}{2} M \omega_z^2 z^2\right) \psi_{n_z}^{(1)}(z; b_z) = \hbar \omega_z \left(n_z + \frac{1}{2}\right) \psi_{n_z}^{(1)}(z; b_z), \tag{3.8a}$$

$$\left(-\frac{\hbar^2}{2M}\Delta + \frac{1}{2}M\omega_r^2 r^2\right)\psi_{m\ n}^{(2)}(r, \varphi; b_r) = \hbar\omega_r(2n + |m| + 1)\psi_{m\ n}^{(2)}(r, \varphi; b_r) . \quad (3.8b)$$

Where M , ω_z and ω_r are any positive numbers satisfying

$$M\omega_z = \frac{\hbar}{b_z^2} , \quad (3.9a)$$

$$M\omega_r = \frac{\hbar}{b_r^2} . \quad (3.9b)$$

Spin and isospin degrees of freedom can eventually be added by considering the tensor product basis

$$\psi_{m\ n\ n_z}(\mathbf{r}; b_r, b_z) \otimes |\pm\rangle_s \otimes |\pm\rangle_t . \quad (3.10)$$

3.2.1 Orthonormality relations

The basis functions satisfy

$$\int_{-\infty}^{+\infty} dz \psi_{n_z}^{(1)}(z; b_z) \psi_{n'_z}^{(1)}(z; b_z) = \delta_{n_z n'_z} , \quad (3.11a)$$

$$\int_0^{+\infty} r dr \int_0^{2\pi} d\varphi \psi_{m\ n}^{(2)*}(r, \varphi; b_r) \psi_{m'\ n'}^{(2)}(r, \varphi; b_r) = \delta_{nn'} \delta_{mm'} . \quad (3.11b)$$

3.2.2 Talman coefficients

As shown in Refs. [79] and [80], products of basis functions can be expanded as finite sums of basis functions times a Gaussian factor.

$$\psi_{n_{z1}}^{(1)}(z; b_z) \psi_{n_{z2}}^{(1)}(z; b_z) = \frac{e^{-z^2/2b_z^2}}{\sqrt{b_z}\sqrt{\pi}} \sum_n T^{(1)n_{z1}n_{z2}} \psi_n^{(1)}(z; b_z) , \quad (3.12)$$

$$\psi_{m_1 n_1}^{(2)*}(r, \varphi; b_r) \psi_{m_2 n_2}^{(2)}(r, \varphi; b_r) = \frac{e^{-r^2/2b_r^2}}{b_r \sqrt{\pi}} \sum_n T^{(2)n_{m_1 n_1 m_2 n_2}} \psi_{m_2 - m_1\ n}^{(2)}(r, \varphi; b_r) . \quad (3.13)$$

Where coefficients $T^{(1)}$ and $T^{(2)}$ (called Talman coefficients [81]) are real and detailed in appendix C.1. Those coefficients properties ensure that sums in Eqs. (3.12) and (3.13) are finite. In Eq. (3.12), index n runs over

$$|n_{z1} - n_{z2}| \leq n_z \leq n_{z1} + n_{z2} \quad \text{with } n_z + n_{z1} + n_{z2} \text{ even} , \quad (3.14)$$

and in Eq. (3.13), index n runs over

$$0 \leq n \leq n_1 + n_2 + \frac{1}{2}(|m_1| + |m_2| - |m_1 - m_2|) \equiv n_{1,2} . \quad (3.15)$$

3.2.3 Moshinsky coefficients

From Ref. [80] it is shown that for $i = 1, 2$

$$\psi_{\mu}^{(i)}(\mathbf{r}_1; b_1) \psi_{\nu}^{(i)}(\mathbf{r}_2; b_2) = \sum_{\alpha\beta} \mathcal{M}_{\mu\nu}^{(i)\alpha\beta}(b_1, b_2) \psi_{\alpha}^{(i)}\left(\frac{B^2}{\sqrt{2}}\left[\frac{\mathbf{r}_1}{b_1^2} + \frac{\mathbf{r}_2}{b_2^2}\right]; \frac{b_1 b_2 \sqrt{2}}{\sqrt{b_1^2 + b_2^2}}\right) \psi_{\beta}^{(i)}\left(\frac{1}{\sqrt{2}}[\mathbf{r}_1 - \mathbf{r}_2]; \frac{\sqrt{b_1^2 + b_2^2}}{\sqrt{2}}\right) , \quad (3.16)$$

$\mathcal{M}^{(1,2)}$ are the Moshinsky coefficients. In our work we will only need a subset of the Moshinsky coefficients which will be called reduced Moshinsky coefficients. By definition

$$\mathcal{M}_{n_{z1}n_{z2}}^{(1) \text{ red}} \equiv \mathcal{M}_{n_{z1} n_{z2}}^{(1)0} (b_z, b_z) , \quad (3.17a)$$

$$\mathcal{M}_{m n_1 n_2}^{(2) \text{ red}} \equiv \mathcal{M}_{(m, n_1) (-m, n_2)}^{(2)(0,0)} (0, n_1 + n_2 + |m|) (b_r, b_r) . \quad (3.17b)$$

Note that reduced Moshinsky coefficients are b_z and b_r independent. The formulas for computing those coefficients are given in Appendix D.

3.3 Calculation of matrix elements

3.3.1 Central term

The central term (see Eq. (3.1a)) is given by

$$V^C(\mathbf{r}_1, \mathbf{r}_2) = \left[W + B\hat{P}_s - H\hat{P}_t - M\hat{P}_s\hat{P}_t \right] e^{-(\mathbf{r}_1 - \mathbf{r}_2)^2/\mu^2} . \quad (3.18)$$

Where $\mu = \mu_1, \mu_2$ and P_s (resp. P_t) is the spin (resp. isospin) exchange operator defined by Eqs (3.2c) (3.2d), these are linear operators such that for any kets $|x_s\rangle, |y_s\rangle$ in spin space and any kets $|x_t\rangle, |y_t\rangle$ in isospin space

$$P_s |x_s\rangle \otimes |y_s\rangle = |y_s\rangle \otimes |x_s\rangle , \quad (3.19a)$$

$$P_t |x_t\rangle \otimes |y_t\rangle = |y_t\rangle \otimes |x_t\rangle . \quad (3.19b)$$

The non-antisymmetrised matrix elements for the central part are by definition

$$V_{\alpha\beta\gamma\delta}^C = \langle 1 : \alpha ; 2 : \beta | V^C | 1 : \gamma ; 2 : \delta \rangle . \quad (3.20)$$

The spin-isospin and spatial contribution are easily factored out

$$V_{\alpha\beta\gamma\delta}^C \equiv V_{\alpha\beta\gamma\delta}^{C_{st}} V_{\alpha\beta\gamma\delta}^{C_r} \equiv V_{\alpha\beta\gamma\delta}^{C_{st}} V_{\alpha\beta\gamma\delta}^{C_1} V_{\alpha\beta\gamma\delta}^{C_2} \quad (3.21)$$

where

$$\begin{aligned} V_{\alpha\beta\gamma\delta}^{C_{st}} &\equiv W \delta_{s_\alpha s_\gamma} \delta_{s_\beta s_\delta} \delta_{t_\alpha t_\gamma} \delta_{t_\beta t_\delta} \\ &+ B \delta_{s_\alpha s_\delta} \delta_{s_\beta s_\gamma} \delta_{t_\alpha t_\gamma} \delta_{t_\beta t_\delta} \\ &- H \delta_{s_\alpha s_\gamma} \delta_{s_\beta s_\delta} \delta_{t_\alpha t_\delta} \delta_{t_\beta t_\gamma} \\ &- M \delta_{s_\alpha s_\delta} \delta_{s_\beta s_\gamma} \delta_{t_\alpha t_\delta} \delta_{t_\beta t_\gamma} , \end{aligned} \quad (3.22)$$

and

$$V_{\alpha\beta\gamma\delta}^{C_1} = \int dz_1 dz_2 \psi_\alpha^{(1)}(z_1; b_z) \psi_\beta^{(1)}(z_2; b_z) e^{-(z_1 - z_2)^2/\mu^2} \psi_\gamma^{(1)}(z_1; b_z) \psi_\delta^{(1)}(z_2; b_z) , \quad (3.23a)$$

$$V_{\alpha\beta\gamma\delta}^{C_2} = \int d^2\vec{r}_1 d^2\vec{r}_2 \psi_\alpha^{(2)*}(\vec{r}_1; b_r) \psi_\beta^{(2)*}(\vec{r}_2; b_r) e^{-(\vec{r}_1 - \vec{r}_2)^2/\mu^2} \psi_\gamma^{(2)}(\vec{r}_1; b_r) \psi_\delta^{(2)}(\vec{r}_2; b_r) . \quad (3.23b)$$

The strategy for computing the last integrals is exposed in great details in [79]. In this reference it is shown (Eqs.(D.2) and (20)) that¹

$$V_{\alpha\beta\gamma\delta}^{C_1} = \delta(n_{z\alpha} + n_{z\beta} + n_{z\gamma} + n_{z\delta} \text{ even}) \frac{\mu}{\sqrt{2\pi^3} b_z} \sum_{n_z = |n_{z\beta} - n_{z\delta}|, 2}^{n_{z\beta} + n_{z\delta}} T^{(1)n_z}_{n_{z\beta} n_{z\delta}} \bar{F}_{n_{z\alpha} n_{z\gamma}}^{n_z} , \quad (3.24)$$

¹In Eq.(3.24) the summation step is 2 as indicated.

and

$$V_{\alpha\beta\gamma\delta}^{C_2} = \delta_{m_\alpha+m_\beta, m_\gamma+m_\delta} \frac{G_r - 1}{G_r + 1} \sum_{n_1=0}^{n_{\beta,\delta}} \sum_{n_2=0}^{n_{\alpha,\gamma}} T_{n_\alpha, m_\alpha; n_\gamma, m_\gamma}^{(2)n_2} T_{n_\beta, m_\beta; n_\delta, m_\delta}^{(2)n_1} \bar{I}(m_\alpha - m_\gamma, n_1, n_2) . \quad (3.25)$$

In Eq. (3.25), \bar{I} is given by Eq. (G.5), coefficient $\bar{F}_{n_{z\alpha}, n_{z\gamma}}^{n_z}$ in Eq. (3.24) is defined in Eq. (G.6), and G_r is defined in Eq. (G.4).

3.3.2 Coulomb term

The Coulomb term is (Eq. (3.1b))

$$V^{\text{Coul}}(\mathbf{r}_1, \mathbf{r}_2) \equiv \frac{q^2}{|\mathbf{r}_1 - \mathbf{r}_2|} . \quad (3.26)$$

Coulomb matrix elements are readily factorised in a spatial part and spin-isospin part

$$V_{\alpha\beta\gamma\delta}^{\text{Coul}} \equiv V_{\alpha\beta\gamma\delta}^{\text{Coul}_r} V_{\alpha\beta\gamma\delta}^{\text{Coul}_{st}} , \quad (3.27)$$

with

$$V_{\alpha\beta\gamma\delta}^{\text{Coul}_{st}} \equiv \delta_{s_\alpha s_\gamma} \delta_{s_\beta s_\delta} \delta(t_\alpha = t_\beta = t_\gamma = t_\delta = \text{proton}) , \quad (3.28)$$

and

$$V_{\alpha\beta\gamma\delta}^{\text{Coul}_r} \equiv q_{\text{proton}}^2 \int d^3\mathbf{r}_1 d^3\mathbf{r}_2 \psi_\alpha^*(\mathbf{r}_1) \psi_\beta^*(\mathbf{r}_2) \frac{1}{|\mathbf{r}_1 - \mathbf{r}_2|} \psi_\gamma(\mathbf{r}_1) \psi_\delta(\mathbf{r}_2) . \quad (3.29)$$

As shown in Ref. [80]

$$\begin{aligned} V_{\alpha\beta\gamma\delta}^{\text{Coul}_r} &= \frac{q_{\text{proton}}^2 \sqrt{2}}{\pi^{1/4}} \sum_{n_\mu=0}^{n_{\alpha\gamma}} \sum_{n_\nu=0}^{n_{\beta\delta}} \sum_{n_{z\mu}=|n_{z\alpha}-n_{z\gamma}|, 2}^{n_{z\alpha}+n_{z\gamma}} \sum_{n_{z\nu}=|n_{z\beta}-n_{z\delta}|, 2}^{n_{z\beta}+n_{z\delta}} \\ &\times T_{n_{z\beta} n_{z\delta}}^{(1)n_{z\nu}} T_{n_{z\alpha} n_{z\gamma}}^{(1)n_{z\mu}} T_{m_\beta n_\beta}^{(2)n_\nu} T_{m_\delta n_\delta}^{(2)n_\mu} \mathcal{M}_{n_{z\mu} n_{z\nu}}^{(1)\text{red}} \mathcal{M}_{m_\gamma - m_\alpha}^{(2)\text{red}} \\ &\times I_{\text{coul}}(n_\mu + n_\nu + |m_\gamma - m_\alpha|, n_{z\mu} + n_{z\nu}) , \end{aligned} \quad (3.30)$$

with $I_{\text{coul}}(n, n_z)$ given by Eq.(G.13).

3.3.3 Two-body center of mass correction

The center of mass correction reads as in Eq. (3.1c)

$$V^{\text{COM}} = -\frac{\mathbf{p}_1 \cdot \mathbf{p}_2}{m\langle A \rangle} , \quad (3.31)$$

and the corresponding matrix element is

$$\begin{aligned} V_{\alpha\beta\gamma\delta}^{\text{COM}} &= -\frac{1}{m\langle A \rangle} \langle \alpha\beta | \mathbf{p}_1 \cdot \mathbf{p}_2 | \gamma\delta \rangle \\ &= -\frac{1}{m\langle A \rangle} \langle \psi_\alpha \psi_\beta | \mathbf{p}_1 \cdot \mathbf{p}_2 | \psi_\gamma \psi_\delta \rangle \delta_{s_\alpha s_\gamma} \delta_{s_\beta s_\delta} \delta_{t_\alpha t_\gamma} \delta_{t_\beta t_\delta} . \end{aligned} \quad (3.32)$$

It is shown in App. G.3 that

$$\langle \psi_\alpha \psi_\beta | \mathbf{p}_1 \cdot \mathbf{p}_2 | \psi_\gamma \psi_\delta \rangle = -\hbar^2 \left(-C_{\alpha\gamma}^+ C_{\beta\delta}^- - C_{\alpha\gamma}^- C_{\beta\delta}^+ + C_{\alpha\gamma}^3 C_{\beta\delta}^3 \right) , \quad (3.33)$$

where

$$C_{\alpha\beta}^+ = \delta_{n_{z\alpha}n_{z\beta}} \delta_{m_\alpha, m_\beta+1} \frac{(-1)^{\delta(m_\beta \leq -1)}}{b_r \sqrt{2}} \left[\sqrt{n_\beta + \delta(m_\beta \leq -1)} \delta_{n_\alpha, n_\beta + (-1)^{\delta(m_\beta \geq 0)}} + \sqrt{n_\beta + |m_\beta| + \delta(m_\beta \geq 0)} \delta_{n_\alpha, n_\beta} \right], \quad (3.34)$$

$$C_{\alpha\beta}^- = \delta_{n_{z\alpha}n_{z\beta}} \delta_{m_\alpha, m_\beta-1} \frac{(-1)^{\delta(m_\beta \leq 0)}}{b_r \sqrt{2}} \left[\sqrt{n_\beta + \delta(m_\beta \geq 1)} \delta_{n_\alpha, n_\beta + (-1)^{\delta(m_\beta \leq 0)}} + \sqrt{n_\beta + |m_\beta| + \delta(m_\beta \leq 0)} \delta_{n_\alpha, n_\beta} \right], \quad (3.35)$$

$$C_{\alpha\beta}^3 = \delta_{m_\alpha m_\beta} \delta_{n_\alpha n_\beta} \frac{1}{b_z \sqrt{2}} \left[\sqrt{n_{z\beta}} \delta_{n_{z\alpha}, n_{z\beta}-1} - \sqrt{n_{z\beta} + 1} \delta_{n_{z\alpha}, n_{z\beta}+1} \right]. \quad (3.36)$$

3.3.4 Density term

Transforming ρ density matrix from cylindrical harmonic oscillator basis to spatial representation gives

$$\begin{aligned} \rho(\mathbf{r}_1, s_1, t_1; \mathbf{r}_2, s_2, t_2) &= \langle \mathbf{r}_1, s_1, t_1 | \hat{\rho} | \mathbf{r}_2, s_2, t_2 \rangle \\ &= \sum_{\alpha\beta} \langle \mathbf{r}_1, s_1, t_1 | \alpha \rangle \langle \alpha | \hat{\rho} | \beta \rangle \langle \beta | \mathbf{r}_2, s_2, t_2 \rangle \\ &= \sum_{\alpha\beta} \psi_{m_\alpha n_\alpha n_{z\alpha}}(\mathbf{r}_1) \psi_{m_\beta n_\beta n_{z\beta}}^*(\mathbf{r}_2) \\ &\quad \times \rho(m_\alpha, n_\alpha, n_{z\alpha}, s_1, t_1; m_\beta, n_\beta, n_{z\beta}, s_2, t_2). \end{aligned} \quad (3.37)$$

Only the case with $\mathbf{r}_1 = \mathbf{r}_2$ and $t_1 = t_2$ is to be considered, and one defines

$$\rho(\mathbf{r}) \equiv \sum_{st} \rho(\mathbf{r}, s, t; \mathbf{r}, s, t). \quad (3.38)$$

Antisymmetrised density pseudo-operator has been introduced in Eq. (3.1d) as

$$V^D(r_1, r_2) = t_3 (1 + x_0 P_s) (1 - P_s P_t) \delta(r_1 - r_2) \rho^{\alpha_G}(r_1), \quad (3.39)$$

such that density matrix element factorise into a spin-isospin part and a spatial part.

$$V_{\alpha\beta\gamma\delta}^D = \langle \alpha\beta | V^D | \gamma\delta \rangle \quad (3.40)$$

$$= V_{\alpha\beta\gamma\delta}^{D_{st}} V_{\alpha\beta\gamma\delta}^{D_r}, \quad (3.41)$$

with

$$\begin{aligned} V_{\alpha\beta\gamma\delta}^{D_{st}} &= \left(\delta_{s_\alpha s_\gamma} \delta_{s_\beta s_\delta} + x_0 \delta_{s_\alpha s_\delta} \delta_{s_\beta s_\gamma} \right) \delta_{t_\alpha t_\gamma} \delta_{t_\beta t_\delta} \\ &\quad - \left(x_0 \delta_{s_\alpha s_\gamma} \delta_{s_\beta s_\delta} + \delta_{s_\alpha s_\delta} \delta_{s_\beta s_\gamma} \right) \delta_{t_\alpha t_\delta} \delta_{t_\beta t_\gamma}, \end{aligned} \quad (3.42)$$

and

$$V_{\alpha\beta\gamma\delta}^{D_r} = \int d^3\mathbf{r} \psi_{m_\alpha n_\alpha n_{z\alpha}}^*(\mathbf{r}) \psi_{m_\beta n_\beta n_{z\beta}}^*(\mathbf{r}) \rho^{\alpha_G}(\mathbf{r}) \psi_{m_\gamma n_\gamma n_{z\gamma}}(\mathbf{r}) \psi_{m_\delta n_\delta n_{z\delta}}(\mathbf{r}). \quad (3.43)$$

The explicit density dependence of the interaction is precisely what is preventing it from being a true Hamiltonian. This manifests at mean-field level by the presence of a rearrangement contribution as detailed in App. G.4.2.

3.3.5 Spin-orbit term

The spin-orbit term has been introduced in Eq. (3.1e) as

$$iW_{LS}(\boldsymbol{\sigma}_1 + \boldsymbol{\sigma}_2) \cdot \overleftarrow{\mathbf{k}}' \times \delta(\mathbf{r}) \overrightarrow{\mathbf{k}}. \quad (3.44)$$

As shown in App. G.5, antisymmetrised spin-orbit matrix elements can be expressed as

$$\begin{aligned} \overline{V}_{\alpha\beta\gamma\delta}^{\text{SO}} = & \frac{iW_{LS}}{2} \left[-\left(I_{\alpha\beta\gamma\delta}^+ + I_{\beta\alpha\delta\gamma}^+\right) \langle s_\alpha s_\beta | \sigma_1^- + \sigma_2^- | s_\gamma s_\delta \rangle \right. \\ & - \left. \left(I_{\alpha\beta\gamma\delta}^- + I_{\beta\alpha\delta\gamma}^-\right) \langle s_\alpha s_\beta | \sigma_1^+ + \sigma_2^+ | s_\gamma s_\delta \rangle \right. \\ & \left. + \left(I_{\alpha\beta\gamma\delta}^3 + I_{\beta\alpha\delta\gamma}^3\right) \langle s_\alpha s_\beta | \sigma_1^3 + \sigma_2^3 | s_\gamma s_\delta \rangle \right] \langle t_\alpha t_\beta | T | t_\gamma t_\delta \rangle, \quad (3.45) \end{aligned}$$

where I^+ , I^- , I^3 , T are respectively defined by Eqs. (G.52), (G.53) (G.54), (G.48), and $\sigma_{1,2}^+$, $\sigma_{1,2}^-$, $\sigma_{1,2}^3$ are defined in Eqs. (E.4).

Chapter 4

PGCM-EC model study

Contents

| | |
|---|-----------|
| 4.1 Brink-Boeker potential | 47 |
| 4.2 GCM setting | 50 |
| 4.3 Latin hypercube sampling | 51 |
| 4.4 Cost function | 51 |
| 4.5 PGCM-EC setting | 52 |
| 4.5.1 Parameter space | 52 |
| 4.5.2 Set of HF states | 52 |
| 4.5.3 Set of kernels | 52 |
| 4.6 Brute-force learning | 53 |

This chapter defines the model chosen to test the (P)GCM-EC emulator. This model uses

1. a simple effective interaction with four parameters to be varied,
2. a realistic GCM calculation of the doubly open-shell ^{20}Ne nucleus,
3. a brute force learning algorithm to choose optimal training parameters/GCM vectors.

Despite being relatively simple and limited to a single nucleus, it allows one to explore in details the characteristics of the (P)GCM-EC emulator. The actual results of the PGCM-EC study is discussed in the following chapters.

4.1 Brink-Boeker potential

The Brink-Boeker two-body interaction [76] is a special case of Eq. (3.1) reading as

$$V_{\text{BB}}(\mathbf{R}, \mathbf{r}) \equiv \sum_{i=1}^2 \left[w_i - m_i \hat{p}_s \hat{p}_t \right] e^{-r^2/\mu_i^2} - \frac{\mathbf{P}_1 \cdot \mathbf{P}_2}{m\langle A \rangle} \quad (4.1a)$$

$$\equiv V^{\text{BB C}} + V^{\text{BB COM2}} \quad , \quad (4.1b)$$

where $w_{1,2}$, $m_{1,2}$ and $\mu_{1,2}$ the set of denote free parameters. The nominal values of parameters [76] collectively denoted as λ_0 are reported in Tab. 4.1.

| i | μ_i | w_i | m_i |
|-----|---------|---------|---------|
| | fm | MeV | MeV |
| 1 | 1.4 | -72.21 | -68.39 |
| 2 | 0.7 | -595.55 | -206.05 |

Table 4.1: Nominal parametrization λ_0 of the Brink-Boeker two-body interaction [76].

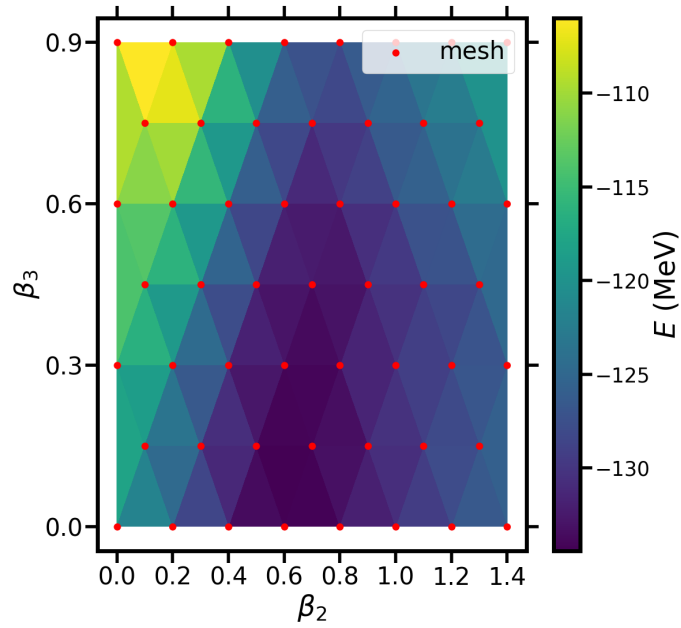


Figure 4.1: Two-dimensional Hartree-Fock potential energy surface in ^{20}Ne obtained in the (β_2, β_3) plane from the nominal Brink-Boeker interaction. The number of mesh points $q_i = (\beta_{2i}, \beta_{3i})$ in the plane, is $n_q = 53$.

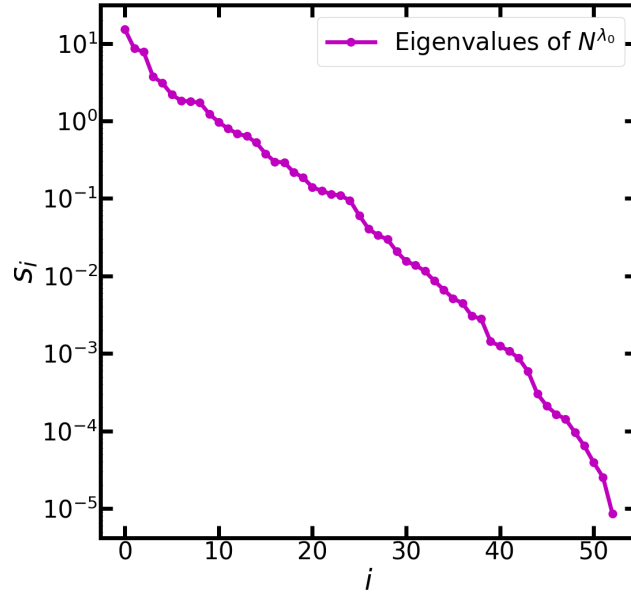


Figure 4.2: Eigenvalues of the norm matrix N^{λ_0} associated with the GCM subspace $E_{n_q}^{\lambda_0}$ with $n_q = 53$ corresponding to the nominal parameter set λ_0 .

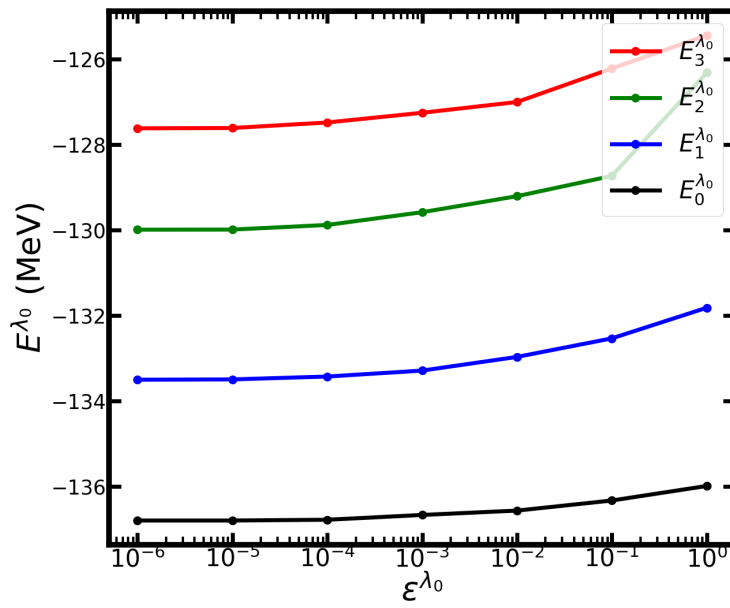


Figure 4.3: Nominal GCM eigenenergies as a function of the threshold ϵ^{λ_0} .

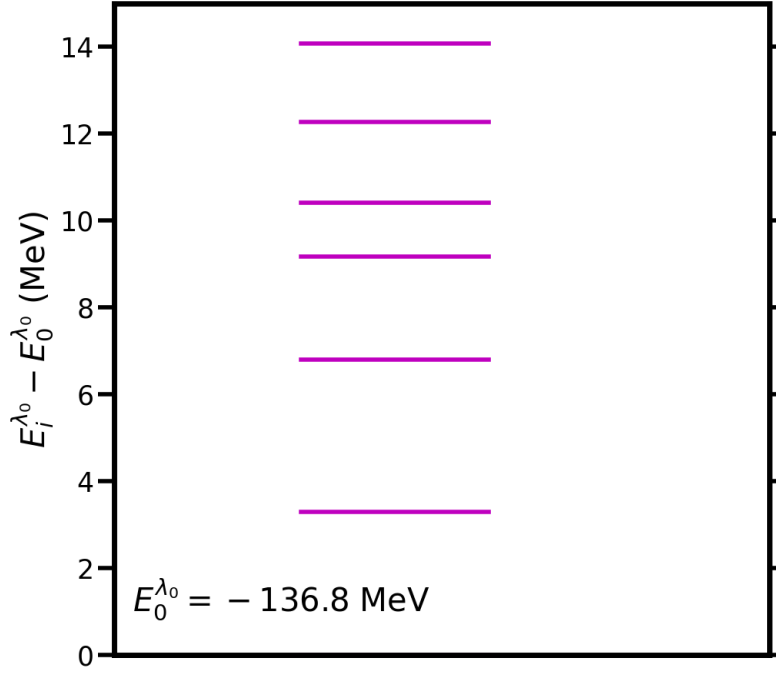


Figure 4.4: GCM spectrum in ^{20}Ne from the nominal Brink-Boeker interaction and the threshold value $\epsilon^{\lambda_0} = 10^{-6}$.

4.2 GCM setting

The present study relies on a realistic GCM calculation of the doubly open-shell nucleus ^{20}Ne based on a set of deformed Hartree-Fock states constrained to different values of the axial quadrupole (β_2) and axial octupole (β_3) moments. While the HF states break both rotational and parity symmetries, the effect of the projection on good angular momentum and parity is left to a future study. Correspondingly, the GCM spectrum purely relates to *vibrational* states. Calculations are performed with the Brink-Boeker two-body interaction using a harmonic oscillator basis truncated to $n_{\text{oscil}} = 8$.

The corresponding two-dimensional HF potential energy surface (PES) obtained for the nominal Brink-Boeker interaction is displayed in Fig. 4.1 as a function of $q = (\beta_2, \beta_3)$. The red dots on the PES are associated with the $n_q = 53$ HF states $|\Phi^{\lambda_0}(q_i)\rangle$, $i = 1, \dots, 53$, constituting the baseline for the subsequent GCM calculation.

Based on these $n_q = 53$ HF states, the GCM subspace $E_{53}^{\lambda_0}$ is considered. The eigenvalues $\{s_i, i = 1, \dots, n_q\}$ of the associated norm matrix N^{λ_0} are displayed in decreasing order in Fig. 4.2. These eigenvalues span 6 orders of magnitude, from a few 10^1 down to about 10^{-5} .

Next, the $1 \leq n_{\lambda_0}^{\text{dim}} \leq n_q$ largest eigenvalues are chosen according to the truncation $s_i \geq \epsilon^{\lambda_0}$ to build the orthogonal basis $\{|\Psi_i^{\lambda_0}\rangle, i = 1, \dots, n_{\lambda_0}^{\text{dim}}\}$ of (the approximation to) $E_{53}^{\lambda_0}$ and solve the Hill-Wheeler-Griffin equation. The corresponding GCM eigenenergies are displayed in Fig. 4.3 as a function of ϵ^{λ_0} . The results demonstrate that the calculation is well converged for $\epsilon^{\lambda_0} \leq 10^{-5}$ and actually remains stable down to the

| Task | Computational cost (s) |
|-------------|-------------------------------|
| HF states | 52884 $\equiv S_{\text{HFB}}$ |
| GCM kernels | 3913 $\equiv S_{\text{ker}}$ |

Table 4.2: Computing cost (in seconds) for the two main steps of a GCM calculation in ^{20}Ne with the Brink-Boeker interaction. The cost of solving the HWG equation is negligible.

lowest eigenvalue. Picking $\epsilon^{\lambda_0} = 10^{-6}$, the GCM excitation spectrum is displayed in Fig. 4.4. The first, second and third excited states are seen to be located at about 3, 7 and 9 MeV, respectively.

Eventually, the computational cost of the GCM calculation is reported in Tab. 4.2. The cost separates into (i) S_{HFB} associated with the computation of the $n_q = 53$ seed HF states and (ii) S_{ker} associated with the computation of the norm and Hamiltonian kernels among those HF states. In the present GCM setting, i.e. in absence of symmetry projections, the cost is dominated by S_{HFB} and amounts to about $S_{\text{HFB}} + S_{\text{ker}} = 16h$. Consequently, performing a very large number n of GCM simulations for different parameter sets amount to a numerical cost of $n \times (S_{\text{HFB}} + S_{\text{ker}})$ that becomes quickly prohibitive. This motivates the present work on emulating (P)GCM simulations.

4.3 Latin hypercube sampling

Having at hands the GCM calculation based on the nominal Brink-Boeker interaction, propagating uncertainties associated with its parameter set relies on sampling the parameters value according to a given probability distribution. Similarly, performing a sensitivity analysis requires to sample a set of pre-defined parameters interval in the most faithful manner.

In this context, the latin hypercube sampling (LHS) is an alternative to a simple random sampling, such that moments of a function over the sampled space are unbiased and display a substantially smaller variance than that of the estimator based on simple random sampling [82, 83]. Assuming that the sampled space is $B = [0, 1]^d$ ($d \geq 1$ integer), and given an integer $N \geq 1$, a LHS of size N on B is obtained by

- randomly choosing π_1, \dots, π_d permutations of $\{1, \dots, N\}$, uniformly distributed over all $n!$ permutations;
- picking, for each $1 \leq i \leq N$, a point $x_i \in \prod_{1 \leq k \leq d} \left[\frac{\pi_k(i)-1}{N}, \frac{\pi_k(i)}{N} \right]$ according to a uniform distribution.

4.4 Cost function

In order to quantitatively evaluate a GCM-EC emulator characterized by the couple (L_{n_t}, n_a) , a cost function is chosen based on a given observable A and a validating set $V \equiv (\lambda_{i_1}, \lambda_{i_2}, \dots, \lambda_{i_{n_v}})$.

For a validating parameter λ_{i_k} , one collects the $n_{\lambda_{i_k}}^{\text{dim}}$ values $A_k^{\text{GCM}}(j)$, $j = 1, \dots, n_{\lambda_{i_k}}^{\text{dim}}$, associated with the GCM eigenstates and the $n_{L_{n_t}}^{\text{dim}}$ values $A_k^{\text{EC}}(i)$, $i = 1, \dots, n_{L_{n_t}}^{\text{dim}}$, associated with the GCM-EC solutions. Then, the cost function for each index $1 \leq j \leq \min(n_{\lambda_{i_k}}^{\text{dim}}, n_{L_{n_t}}^{\text{dim}})$ is given by

$$C(A, j) \equiv \frac{1}{n_v} \sum_{k=1}^{n_v} \left| \frac{A_k^{\text{emul}}(j) - A_k^{\text{gcm}}(j)}{A_k^{\text{gcm}}(j)} \right|, \quad (4.2)$$

and is nothing but the mean relative error of the emulator with respect to the simulator. Eventually, the cost function can in fact combine the error over several GCM solutions and/or over several observables.

4.5 PGCM-EC setting

4.5.1 Parameter space

In the Brink-Boeker interaction, the dependence of only 4 out of 6 parameters, i.e. (m_0, m_1, w_0, w_1) , satisfy Eq. (2.5), which is a necessary condition to apply EC to them¹. Consequently, μ_1, μ_2 are kept fixed to their nominal values whereas a four-dimensional parameter mesh in (m_0, m_1, w_0, w_1) containing $N = 50$ points is generated using LHS within the box

$$B \equiv [m_0^{\lambda_0} - 10, m_0^{\lambda_0} + 10] \times [m_1^{\lambda_0} - 10, m_1^{\lambda_0} + 10] \times [w_0^{\lambda_0} - 10, w_0^{\lambda_0} + 10] \times [w_1^{\lambda_0} - 10, w_1^{\lambda_0} + 10] , \quad (4.3)$$

centered on the nominal parametrisation $\lambda_0 \equiv (m_0^{\lambda_0}, m_1^{\lambda_0}, w_0^{\lambda_0}, w_1^{\lambda_0})$. The obtained parameter mesh is denoted

$$L_{50} \equiv (\lambda_1, \lambda_2, \dots, \lambda_{50}) , \quad (4.4)$$

with, for each $1 \leq i \leq 50$,

$$\lambda_i \equiv (m_0^i, m_1^i, w_0^i, w_1^i) . \quad (4.5)$$

4.5.2 Set of HF states

For each $1 \leq i \leq 50$, the $n_q = 53$ HF states constrained

$$B_{n_q}^{\lambda_i} \equiv \{|\Phi^{\lambda_i}(q)\rangle; q \in S\} , \quad (4.6)$$

are generated using the same generator coordinate mesh $S = (q_1, q_2, \dots, q_{n_q})$ over the (β_2, β_3) plane as the one displayed in Fig. 4.1.

4.5.3 Set of kernels

One considers the set of operators

$$\mathcal{O} \equiv \{\check{H}_1, \check{H}_2, \check{H}_3, \check{H}_4, \text{COM2}, \text{KIN}, R_{1b}, 1\} , \quad (4.7)$$

where R_{1b} denotes the one-body radius operator and 1 is the identity operator. The other operators relate to the decomposition of the Hamiltonian containing the Brink-Boeker interaction according to (with $\lambda = (m_0, m_1, w_0, w_1)$)

$$H^\lambda \equiv m_0 \check{H}_1 + m_1 \check{H}_2 + w_0 \check{H}_3 + w_1 \check{H}_4 + \text{COM2} + \text{Kinetic} , \quad (4.8)$$

where the latter two terms correspond to the two-body center-of-mass correction and the kinetic energy², respectively. For each operator $A \in \mathcal{O}$, the off-diagonal elementary kernels

$$\langle \Phi^{\lambda_i}(q) | A | \Phi^{\lambda_j}(q') \rangle , \quad (4.9)$$

are computed and stored to a file.

¹The use of more involved methods dealing with non-multiplicative dependencies is postponed to a future study.

²The kinetic energy contains the one-body part of the center-of-mass correction.

4.6 Brute-force learning

The notion of brute-force learning is inspired from the self-learning scheme detailed in Ref. [84] in which the sole *emulator* is used to determine incrementally the optimal set of training parameters.

In the self-learning setup, any new potential training point λ_i is tested using the cost function

$$F(\lambda_i) = \sqrt{\frac{\langle \Theta(\lambda_i) | (H^{\lambda_i} - E(\lambda_i))^2 | \Theta(\lambda_i) \rangle}{\langle \Psi(\lambda_i) | (H^{\lambda_i})^2 | \Theta(\lambda_i) \rangle}}, \quad (4.10)$$

where $|\Theta(\lambda_i)\rangle$ is the ground state obtained for parameter λ_i from the already available emulator based on n_t training points whereas $E(\lambda_i) = \langle \Theta(\lambda_i) | H^{\lambda_i} | \Theta(\lambda_i) \rangle$ is the associated energy. The parameter point maximising this cost function is added to the training set and the procedure is repeated recursively. This technique is efficient and reliable but, unfortunately, cannot be applied with our (P)GCM-EC emulator. Indeed, to evaluate Eq. (4.10), the expectation value of the (up to) four-body operator $(H^{\lambda_i})^2$ must be computed, which is not possible with the PAN@CEA numerical solver in its present form. Since this self-learning scheme is not practical for the time being, a more simplistic (but brutal) way to construct the optimal training set is employed.

The brute-force character of the learning method presently employed relates to the fact that it relies on a large enough set of PGCM results pre-computed for parameter values selected via LHS. In the present case, the available parameter values corresponds to the set L_{50} introduced in Eq. (4.4). The optimisation method is rather flexible, i.e. given an emulator involving n_a PGCM eigenstates, the optimisation focuses on a chosen observable A_{optim}

- Total energies ($A_{\text{optim}} \equiv 0$),
- Excitation energies ($A_{\text{optim}} \equiv 1$),
- Radii ($A_{\text{optim}} \equiv 2$),

to be computed for the n_{optim} lowest eigenstates. For example, $(A_{\text{optim}}, n_{\text{optim}}) = (0, 3)$ defines an optimisation performed on E_0, E_1 and E_2 whereas for $(A_{\text{optim}}, n_{\text{optim}}) = (1, 2)$ the optimisation is made on $E_1 - E_0$ and $E_2 - E_0$. Eventually, the optimisation procedure works as follows

- 1 For $1 \leq i < j \leq 50$, all possible training sets $L_2 \equiv (\lambda_i, \lambda_j)$ are constructed and each emulator (L_2, n_a) is tested on the complementary parameter set $V_2 \equiv \{1, \dots, 50\} - L_2$ according to the cost function

$$\max_{1 \leq k \leq n_{\text{optim}}} C(A_{\text{optim}}, k). \quad (4.11)$$

The training set $L_2 \equiv (\lambda_{i_1}, \lambda_{i_2})$ displaying the lowest cost function defines the optimal training set for $n_t = 2$.

- 2 A parameter value is added to the optimal training set $L_{n_t} = (\lambda_{i_1}, \dots, \lambda_{i_{n_t}})$, i.e. for each $i \in \{1, \dots, 50\} - L_{n_t}$, an incremented training set is defined according to

$$L_{n_t+1} \equiv (\lambda_{i_1}, \dots, \lambda_{i_{n_t}}, \lambda_i). \quad (4.12)$$

Each emulator (L_{n_t+1}, n_a) is tested over the complementary set $V_{n_t+1} \equiv \{1, \dots, 50\} - L_{n_t+1}$ according to the cost function

$$\max_{1 \leq k \leq n_{\text{optim}}} C(A_{\text{optim}}, k). \quad (4.13)$$

The training set $L_{n_t} \equiv (\lambda_{i_1}, \dots, \lambda_{i_{n_t}}, \lambda_{i_{n_t+1}})$ displaying the lowest cost function defines the optimal $n_t + 1$ training parameters.

- 3 Step 2 is reiterated until the number of training points is considered large enough.

Chapter 5

PGCM-EC model results

Contents

| | |
|--|----|
| 5.1 Training on excited states | 55 |
| 5.2 Optimisation | 57 |
| 5.3 Matter radius | 59 |
| 5.4 Over training | 59 |
| 5.5 Conclusions | 62 |

So far, the EC method has been applied in conjunction with various many-body methods but it has mainly remained restricted to emulating ground states. Preliminary works have been recently dedicated to excited states but only within the frame of schematic models [59, 85]. Regarding realistic PGCM calculations, one is primarily interested in the collective spectroscopy of nuclei such that the accurate emulation of excited states is indeed primordial. In Refs.[59, 85], as well as in an even more recent study dedicated to the GCM applied to Lipkin-Meshkov-Glick toy model, the necessity to train the emulator on excited states was shown to be key to accurately emulate the corresponding excited states.

In this context, the present chapter exposes the numerical results dedicated to the emulation of realistic GCM calculations according to the model study introduced in Chap. 4. The training set is obtained via the brute-force learning method exposed in Sec. 4.6 up to $n_t = 14$ such that the 36 other available parameter values define the validation set.

5.1 Training on excited states

Figure 5.1 displays the mean and dispersion of the error (%) over the validation set of the four lowest PGCM energies $E_a^{\lambda_i}$ (top panels) and the three associated excitation energies $E_a^{\lambda_i} - E_0^{\lambda_i}$ (bottom panels) as a function of n_t . This is done by only training on the ground state at first ($n_a = 1$), before adding the first excited state ($n_a = 2$) and the second excited state ($n_a = 3$) to the training. The brute-force learning is performed by optimising $(E_0^{\lambda_i}, E_1^{\lambda_i})$.

For $n_a = 1, 2$ and 3, the mean error on the ground-state energy quickly converges towards [0.1, 0.2]% as n_t increases. The dispersion decreases steadily to eventually reach $\pm 0.1\%$. For $n_a = 2$ and 3, one further observes that, while decreasing until $n_t = 5$, the error in fact increases again slowly for $n_t > 5$. For $n_a = 1$, the error on $E_1^{\lambda_i}$ reaches 3% for $n_t = 14$ whereas the error on both $E_2^{\lambda_i}$ and $E_3^{\lambda_i}$ stabilizes around 10%. Further including the first excited state in the training ($n_a > 1$), the error on $E_1^{\lambda_i}$ drops to 0.1%, thus reaching the same accuracy as for the ground-state energy. This observation repeats itself for $E_2^{\lambda_i}$ with $n_a = 3$ and seems to be systematic, i.e. using the n^{th} excited state to train the emulator reduces the mean

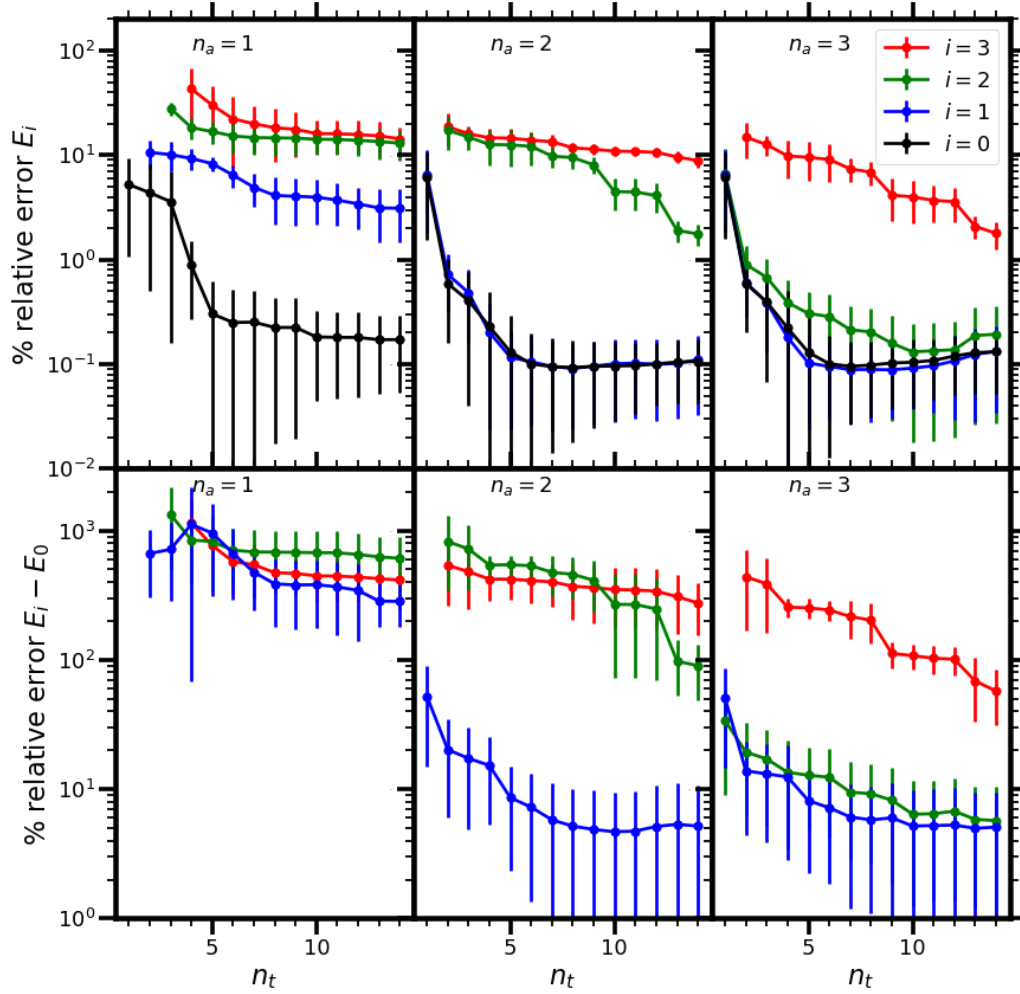


Figure 5.1: Mean and dispersion of the error (%) over the validation set for the four lowest PGCM energies (top panels) and the three associated excitation energies (bottom panels) as a function of n_t for $n_a = 1, 2$ and 3. The brute-force learning is performed by optimising $(E_0^{\lambda_i}, E_1^{\lambda_i})$.

| Error (%) | n_a | | |
|-------------|-------|-----|-----|
| Observable | 1 | 2 | 3 |
| E_0 | 0.2 | 0.1 | 0.1 |
| E_1 | 3.1 | 0.1 | 0.1 |
| E_2 | 13 | 1.8 | 0.2 |
| E_3 | 14 | 8.8 | 1.8 |
| $E_1 - E_0$ | 280 | 5.2 | 5.1 |
| $E_2 - E_0$ | 610 | 90 | 5.7 |
| $E_3 - E_0$ | 410 | 280 | 57 |

Table 5.1: Mean error on the four lowest PGCM energies and on the three associated excitation energies delivered by the PGCM-EC emulator for 36 validation points. The results are extracted from Fig. 5.1 for $n_t = 14$ and $n_a = 1, 2, 3$.

error on the corresponding eigenenergy by more than one order of magnitude to typically reach a value around 0.1% or 0.2%.

The above analysis is also valid for excitation energies, i.e. while the emulator is completely unable to reproduce excitation energies for $n_a = 1$, including a given excited state in the training allows one to reach a mean error of 5 – 6% (~ 170 keV on an 3 MeV excitation) on the corresponding excitation energy for $n_t = 14$.

These results demonstrate that excited states must be included in the training to be satisfactorily reproduced by the emulator. The corresponding mean errors obtained for $n_t = 14$ are reproduced in Tab. 5.1.

5.2 Optimisation

As detailed in Sec. 4.6 the brute-force learning relies not only on choosing an appropriate value for n_a but also on selecting an (a set of) observable A_{optim} to select the optimal training points. Typically, training can be optimised towards total energies or excitation energies.

To investigate the impact of the optimisation method on the performance of the emulator, Fig. 5.2 displays the mean error on $E_0^{\lambda_i}$ (top panels), $E_1^{\lambda_i}$ (middle panels) and $E_1^{\lambda_i} - E_0^{\lambda_i}$ (bottom panels) as a function of n_t for three different optimisations, i.e. optimizing (i) $E_0^{\lambda_i}$ (left panels), (ii) $(E_0^{\lambda_i}, E_1^{\lambda_i})$ (middle panels) and (iii) $E_1^{\lambda_i} - E_0^{\lambda_i}$ (right panels). As the present example focuses on the ground state and the first excited state, $n_a = 2$ is used accordingly.

The optimisations on $E_0^{\lambda_i}$ and $(E_0^{\lambda_i}, E_1^{\lambda_i})$ deliver similar results and the smallest errors for $E_0^{\lambda_i}$ and $E_1^{\lambda_i}$, i.e. between 0.1% and 0.2% for $n_t = 14$. One however observes that the rising of the error on $E_0^{\lambda_i}$ beyond $n_t = 5$ is even more pronounced when solely optimizing on it. The mean error on the first excitation energy $E_1^{\lambda_i} - E_0^{\lambda_i}$ is equal to 5% in this case. Rather optimising the emulator on $E_1^{\lambda_i} - E_0^{\lambda_i}$ enhances the mean error on the individual energies by more than one order of magnitude, i.e. to 4%, while only lowering the mean error on the excitation energy from 5 to 3%.

Eventually, optimizing the training on total energies is optimal to accurately emulate both total and excitation energies. The mean errors extracted from Fig. 5.2 for $n_t = 14$ are reported in Tab. 5.2.

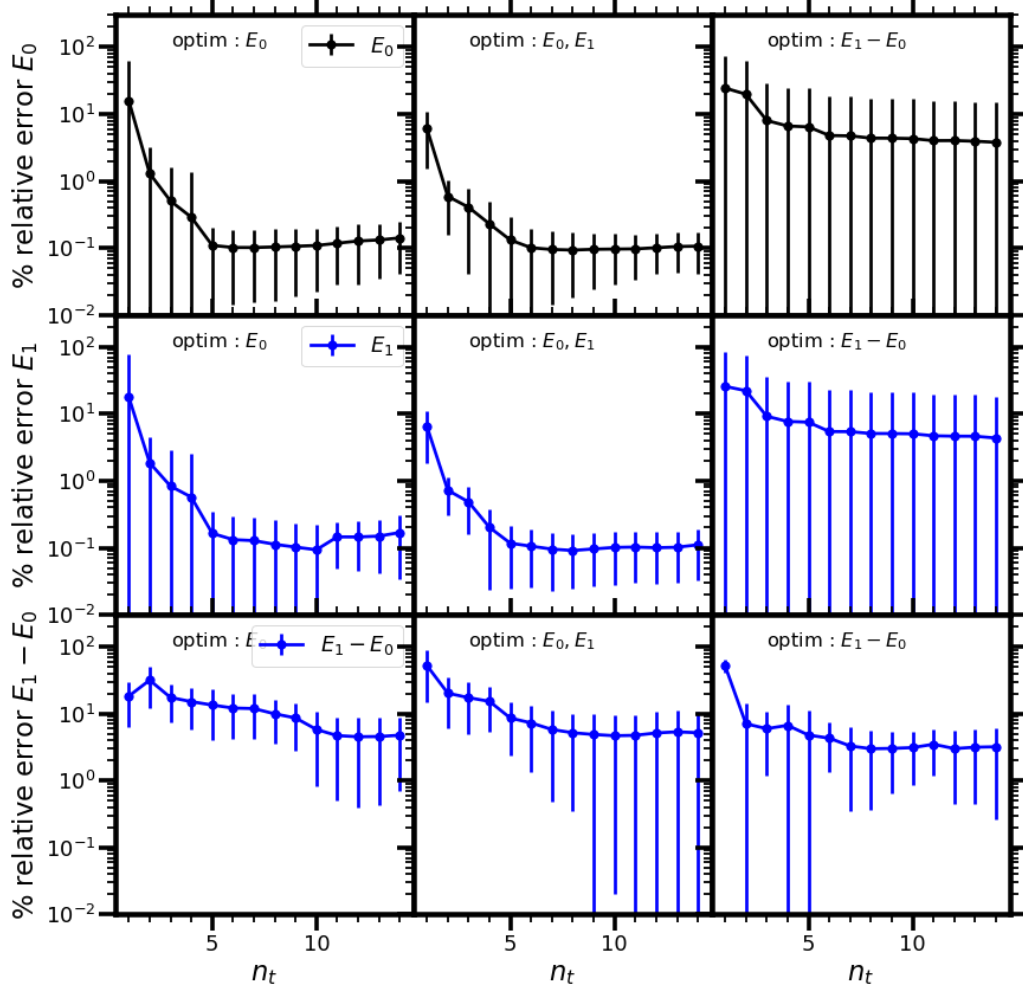


Figure 5.2: Mean and dispersion of the errors (%) over the validation set, on total energies E_0 (top panels), $E_1^{\lambda_i}$ (middle panels) and $E_1^{\lambda_i} - E_0^{\lambda_i}$ (bottom panels) against n_t , for different optimisations, $E_0^{\lambda_i}$ (left panels), $\max(E_0^{\lambda_i}, E_1^{\lambda_i})$ (middle panels) and $E_1^{\lambda_i} - E_0^{\lambda_i}$ (right panels)

| Error (%) | Optimisation | | |
|-------------|--------------|-------|-------------|
| | E_0 | E_1 | $E_1 - E_0$ |
| Observable | | | |
| E_0 | 0.1 | 0.1 | 3.8 |
| E_1 | 0.2 | 0.1 | 4.4 |
| $E_1 - E_0$ | 4.8 | 5.2 | 3.2 |

Table 5.2: Mean error on the two lowest PGCM energies and on the associated excitation energy delivered by the PGCM-EC emulator for 36 validation points. The results are extracted from Fig. 5.2 for $n_t = 14$ and different optimisation options.

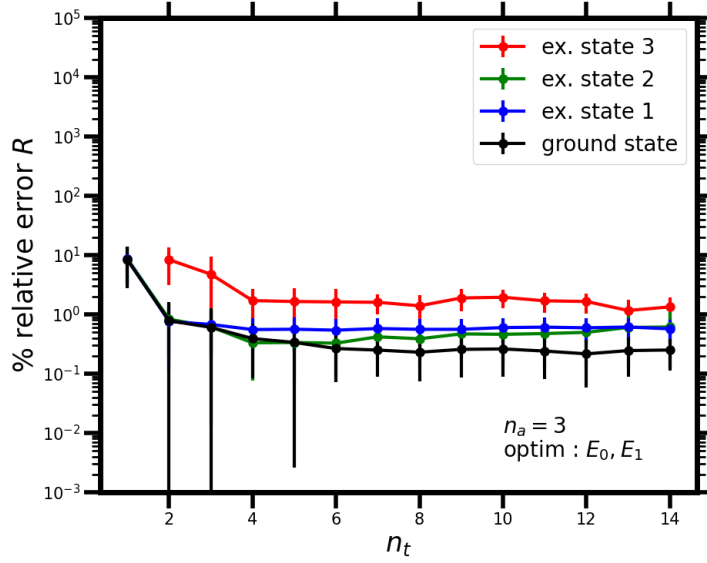


Figure 5.3: Mean error (%) on the matter radius of the four lowest PGCM states as a function of n_t . The training is done for $n_a = 3$ while optimizing $(E_0^{\lambda_i}, E_1^{\lambda_i})$.

5.3 Matter radius

The GCM-EC emulator is not limited to emulate energies and can be used for any observable A for which off-diagonal kernels

$$A_{qq'}^{\lambda_i \lambda_j} \equiv \langle \Phi^{\lambda_i}(q) | A | \Phi^{\lambda_j}(q') \rangle, \quad (5.1)$$

are available. As already mentioned in Sec. 4.5.3, such kernels are indeed readily available for the one-body matter radius¹. Thus, Fig. 5.3 displays the mean error on radii as a function of n_t , for an emulator trained with $n_a = 3$ and optimised on $(E_0^{\lambda_i}, E_1^{\lambda_i})$. The mean errors obtained for the ground-state, the first and the second excited states that are included in the training are comprised between 0.2% and 0.6% whereas the error for the third excited state reaches about 2%. This demonstrates that the GCM-EC emulator can satisfactorily reproduce radii, with a significant benefit from including the corresponding state in the training.

5.4 Over training

Even though the GCM-EC emulator provides a good enough reproduction of total energies, excitation energies and radii for practical applications, it is interesting to deepen the analysis and understand why the mean error quickly saturates around 0.1% for total energies and 1% for excitation energies.

As discussed in Sec. 2.1.2, the emulator applied for the training values is characterized by a null error whenever the training vectors are exact solutions of Schrodinger's equation. In practice, however, EC is applied on the basis of approximate solutions of Schrodinger's equation delivered by a certain simulator one wishes to emulate. This is particularly true of (P)GCM states that are not good approximations to the exact eigenstates of the Hamiltonian, even though energy differences are. Correspondingly, a (P)GCM

¹Because of the lack of angular momentum projection in the present study, the same cannot be done here for electromagnetic transitions. Such a study is postponed to a future work.

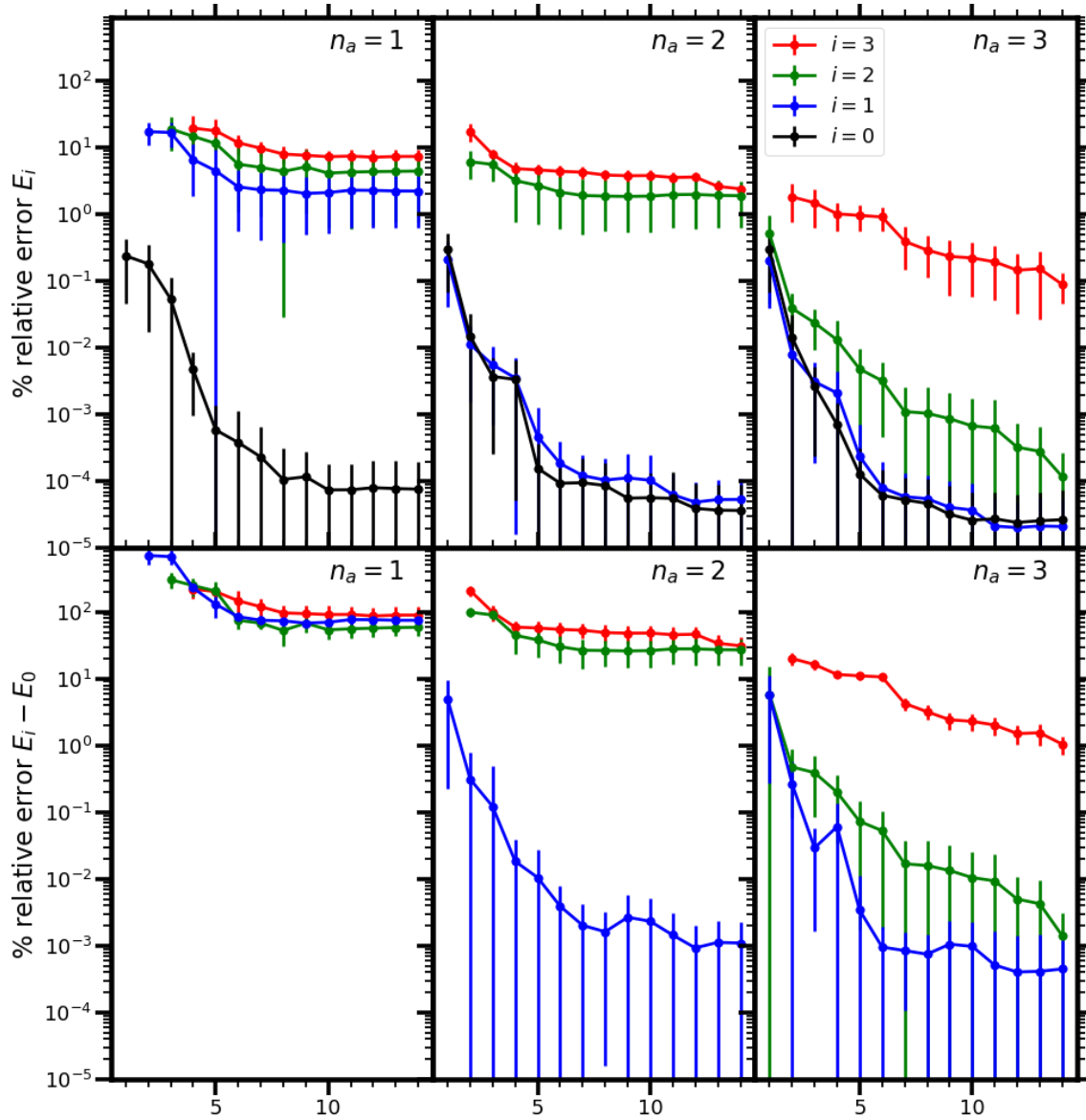


Figure 5.4: Same as Fig. 5.1 for the toy GCM defined in the fixed nominal subspace $E_{53}^{\lambda_0}$.

| Error (%) | n_a | | |
|-------------|-------------|-------------|-------------|
| | 1 | 2 | 3 |
| Observable | | | |
| E_0 | 8.10^{-5} | 4.10^{-5} | 3.10^{-5} |
| E_1 | 2.2 | 5.10^{-5} | 2.10^{-5} |
| E_2 | 4.5 | 1.9 | 1.10^{-4} |
| E_3 | 7.4 | 2.4 | 0.1 |
| $E_1 - E_0$ | 75 | 1.10^{-3} | 4.10^{-4} |
| $E_2 - E_0$ | 58 | 27 | 1.10^{-3} |
| $E_3 - E_0$ | 89% | 31% | 1.1% |

Table 5.3: Same as Tab. 5.1 for the toy GCM based on the fixed nominal subspace $E_{53}^{\lambda_0}$.

subspace $E_{n_p}^{(\sigma)\lambda_i}$ typically displays a very small effective dimension compared to the training subspace $E_{n_p}^{\sigma L_{n_t}}$ when n_t becomes significantly greater than one. For a training value, the emulated state thus runs the risk to be significantly better than the (P)GCM state one wishes to emulate, thus inducing a non-zero error on the energy. This is particularly clear for the ground-state energy whose emulated value runs the risk to be below the reference one and can only moves away from it by further adding training vectors. Eventually, such a systematic error can propagate to the parameter values that are not in the training set.

In order to investigate the quantitative role of this potential over training, the GCM-EC emulator is temporarily applied to a toy formulation of the GCM based on the sole nominal GCM subspace $E_{53}^{\lambda_0}$, i.e. whenever changing the parameter set, the GCM subspace remains fixed. In such a case, no over training is possible given that the training space remains included into $E_{53}^{\lambda_0}$ all throughout. Figure 5.4 represents the counterpart of Fig. 5.1 for this toy GCM. The mean errors are considerably lower than in Fig. 5.1 and do not saturate at 0.1% for total energies and 1% for excitation energies; i.e. the mean error reaches few $10^{-5}\%$ for the former and few $10^{-4}\%$ for the latter at $n_t = 14$.

The above analysis proves that it is possible to produce an extremely accurate emulator in the toy GCM based on a fixed PGCM subspace. In order to quantify to which extend the lower bound observed whenever relaxing such a simplification is indeed partly or totally due to an over training, Fig. 5.5 displays the mean error on the GCM ground-state energy for three different parameter sets

1. The training set in the realistic GCM,
2. The validation set in the realistic GCM,
3. The training set in the toy GCM.

On the scale used in the figure, the error obtained for the training set in the toy GCM is essentially zero. This demonstrates that whenever the training ground states are built over the full Hilbert space of the problem at play, EC allows to emulate the ground state corresponding to other parameter sets extremely accurately. Working with the realistic (P)GCM, whose main feature is to efficiently operate within a physically-optimized low-dimensional space, the emulator displays a systematic over training that grows with n_t . In the present application, the error of the emulated ground-state energy for training values, which is zero by construction for $n_t = 1$, decreases monotonically with n_t , which indeed signals the over training. Eventually, the mean error over the training set reaches -0.3% for $n_t = 14$. Moving to the validation set, the mean error is positive and large for $n_t = 1$ but quickly decreases with n_t . For $n_t > 5$, the mean error becomes negative and eventually reaches -0.1% for $n_t = 14$ as discussed earlier on. While it is clear from

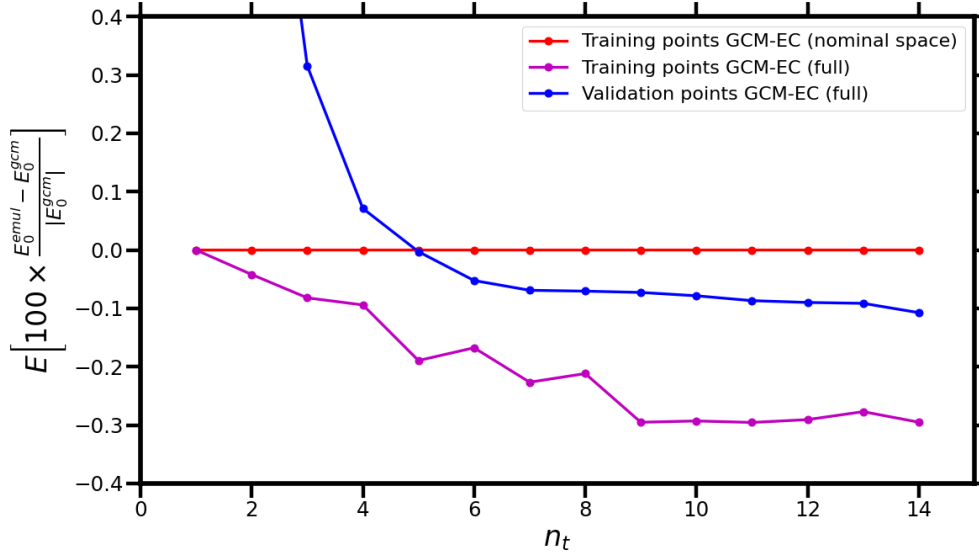


Figure 5.5: Mean error on the ground-state energy as a function of n_t for both the training and validation sets of the realistic GCM as well as for the training set of the toy GCM based on a fixed nominal GCM subspace.

a variational viewpoint that the over training also impacts the validation set², the associated value is not as large as for the training set, eventually leading to a smaller error. While it is counter intuitive that the error is larger for the training set than for the validation set, it is in fact due to a compensation of errors.

Indeed, the GCM-EC emulator does not only suffer from a (small) *over* training due to the training subspace being larger than a single GCM subspace, it also suffers from an (eventually even smaller) *under* training due to the fact that the GCM subspace associated with a given validation point is not fully spanned by the training subspace. Both act in opposite direction thus leading to a compensation of (small) errors³.

5.5 Conclusions

Employing realistic GCM calculations based on a simple but realistic enough two-body interaction, the GCM-EC emulator was shown to deliver an accurate reproduction of total energies ($\sim 0.1 - 0.2\%$ error), excitation energies ($\sim 5 - 6\%$ error) and matter radii ($\sim 0.2 - 0.6\%$ error) of the low-lying GCM states. Importantly, achieving such results requires to include the excited states of interest in the training.

While sufficient in practice, the lower bound on the error was shown to result from two (compensating) errors that are intimately related to the nature of the (P)GCM

1. an *over* training due to the growing dimension of the training space with n_t that largely supersedes the subspace characterizing a (P)GCM simulation,

²As opposed to Fig. 5.5, the absolute value of the error was plotted in previous figures, which explains why the over training error makes the error rise beyond $n_t = 5$ in Figs 5.1 and 5.2. The fact that the rise is more pronounced when optimizing on $E_0^{\lambda_i}$ alone rather than on both $E_0^{\lambda_i}$ and $E_1^{\lambda_i}$ in Fig. 5.2 is due to the fact that the over training is maximized when optimizing the sole ground state.

³Because the GCM subspace associated with a training point is fully included into the training subspace, training points cannot suffer from such an under training. Consequently, training points do not benefit from such a compensation effect as seen in Fig. 5.5.

2. an *under* training induced by the imperfect spanning of a given (P)GCM subspace by the training subspace.

While the over training was explicitly characterized and quantified, the notion of "imperfect spanning of a given (P)GCM subspace by the training subspace" remains qualitative at this point. It is the goal of the next chapter to characterize it more quantitatively by invoking a computable *separation distance* between any two subspaces of the complete Hilbert space.

Chapter 6

Subspace distances

Contents

| | |
|---|-----------|
| 6.1 Metric | 65 |
| 6.1.1 Definitions | 65 |
| 6.2 Parameters distance | 66 |
| 6.2.1 Parameter distance | 66 |
| 6.3 Subspaces distance | 66 |
| 6.3.1 Identical dimensions | 67 |
| 6.3.2 Different dimensions | 69 |
| 6.3.3 Limit cases | 71 |
| 6.4 Numerical tests | 71 |
| 6.4.1 Inclusion and orthogonality | 71 |
| 6.4.2 Distances between GCM subspaces | 72 |
| 6.4.3 Distance to training subspace | 73 |

The performance of the (P)GCM-EC emulator characterized in Chap. 5 is sufficient to perform large-scale studies with small enough error on energies and radii of collective excited states. Yet, the over training associated with a given training subspace and the difficulty to emulate arbitrary (P)GCM subspaces out of that training subspace set lower bound to the achievable accuracy of the (P)GCM-EC emulator.

In the present chapter, the goal is to better characterize and quantify these two limitations that are inherent to the (P)GCM, i.e. they relate to the fact that the (P)GCM diagonalizes the Hamiltonian in a very small, physically optimized, subspace of \mathcal{H}_A . In order to so, the goal is to be able to compute

1. the proximity of a parameter $\mu \in \mathbb{R}^{n_p}$ to the training set L_{n_t} ,
2. the proximity of a PGCM subspace $E_{n_p}^{\sigma\mu}$ to the training subspace $E_{n_p}^{\sigma L_{n_t}}$,

and to correlate the error of the emulator with such distances.

6.1 Metric

6.1.1 Definitions

Let E be a non-empty set. A *metric* ([86], chapter 3) on E is a map $d : E \times E \rightarrow \mathbb{R}^+$ satisfying, for all $x, y, z \in E$,

$$d(x, y) = d(y, x) , \tag{6.1a}$$

$$d(x, y) = 0 \iff x = y, \quad (6.1b)$$

$$d(x, y) \leq d(x, z) + d(z, y). \quad (6.1c)$$

When only a subset of these three properties are satisfied, weaker notions are invoked such that d is coined as

- a *semimetric* if (6.1a) and (6.1b) are true, but (6.1c) is not.
- a *pseudometric* if (6.1a) and (6.1c) are true, but (6.1b) is replaced by the weaker condition

$$d(x, x) = 0, \quad (6.2)$$

for all $x \in E$.

- a *premetric* if (6.1a) and (6.2) are true, but (6.1c) is not.

Given d a premetric on E and A a nonempty subset of E , the *distance* between an element $x \in E$ and the subset is given by

$$d(A, x) \equiv \inf_{y \in A} d(y, x). \quad (6.3)$$

6.2 Parameters distance

To define the distance between a parameter $\mu \in \mathbb{R}^{n_p}$ and the training set L_{n_t} , \mathbb{R}^{n_p} is assumed to be endowed with the standard vector space structure, the standard scalar product $\langle \cdot, \cdot \rangle$, the norm $\|x\| \equiv \sqrt{\langle x, x \rangle}$ and the metric

$$d(x, y) \equiv \|x - y\| = \left(\sum_{i=1}^{n_p} (x_i - y_i)^2 \right)^{1/2}. \quad (6.4)$$

Given this metric d on \mathbb{R}^{n_p} , the distance between μ and the set L_{n_t} is introduced

6.2.1 Parameter distance

The distance between an arbitrary parameter μ and the training set L_{n_t} is thus given by

$$d_s(L_{n_t}, \mu) \equiv d(L_{n_t}, \mu) = \inf_{\lambda \in L_{n_t}} d(\lambda, \mu), \quad (6.5a)$$

Given that L_{n_t} is closed in E , the distance satisfy

$$d_s(L_{n_t}, \mu) = 0 \iff \mu \in L_{n_t}, \quad (6.6a)$$

The computation of $d_s(L_{n_t}, \mu)$ is straightforward.

6.3 Subspaces distance

The question of the distance between two linear subspaces of a given vector space is not standard. In order to set it for the problem of present interest, let us introduce, for $1 \leq p \leq \dim \tilde{\mathcal{F}}$, the set $\text{Gr}(p, \tilde{\mathcal{F}})$ of the p -dimensional linear subspaces of $\tilde{\mathcal{F}}^1$. This set, together with a canonical riemannian manifold structure [87] and [88] chapter 16.11, is known to be a *grassmannian manifold*.

¹Recall that $\tilde{\mathcal{F}}$ denotes a finite-dimensional truncated Fock space.

6.3.1 Identical dimensions

Let us first consider the case of two subspaces of identical dimensions, i.e. two PGCM subspaces $E_{n_q}^{\sigma\mu_1}$ and $E_{n_q}^{\sigma\mu_2}$ of identical (effective) dimensions $n_{\sigma\mu_1}^{\dim} = n_{\sigma\mu_2}^{\dim} \equiv p$ such that they both belong to $\text{Gr}(p, \tilde{\mathcal{F}})$.

Principal vectors and angles

In order to define the distance between both subspaces, one needs to first extract the associated *principal vectors* and *principal angles*. Given the two orthonormal bases $\{|\Xi_q^{\sigma\mu_1}\rangle; q = 1, \dots, p\}$ and $\{|\Xi_q^{\sigma\mu_2}\rangle; q = 1, \dots, p\}$ extracted according to the protocol detailed in Sec. 1.7, the principal vectors $\{|\Lambda_q^{\sigma\mu_1}\rangle; q = 1, \dots, p\}$ and $\{|\Lambda_q^{\sigma\mu_2}\rangle; q = 1, \dots, p\}$ belonging respectively to $E_{n_q}^{\sigma\mu_1}$ and $E_{n_q}^{\sigma\mu_2}$ are defined recursively via the algorithm

1. For $q = 1, \dots, p$

(a) maximize $\langle \Lambda_q^{\sigma\mu_1} | \Lambda_q^{\sigma\mu_2} \rangle$,

(b) under the constraints that

$$\langle \Lambda_q^{\sigma\mu_1} | \Lambda_1^{\sigma\mu_1} \rangle = \dots = \langle \Lambda_q^{\sigma\mu_1} | \Lambda_{q-1}^{\sigma\mu_1} \rangle = 0 ,$$

$$\langle \Lambda_q^{\sigma\mu_2} | \Lambda_1^{\sigma\mu_2} \rangle = \dots = \langle \Lambda_q^{\sigma\mu_2} | \Lambda_{q-1}^{\sigma\mu_2} \rangle = 0 ,$$

$$\langle \Lambda_q^{\sigma\mu_1} | \Lambda_q^{\sigma\mu_1} \rangle = \langle \Lambda_q^{\sigma\mu_2} | \Lambda_q^{\sigma\mu_2} \rangle = 1 ,$$

2. go back to 1

Once the principal vectors have been determined, the p principal angles $\{\theta_q^{\sigma\mu_1\mu_2}, q = 1, \dots, p\}$ are obtained via

$$\cos \theta_q^{\sigma\mu_1\mu_2} \equiv \left| \langle \Lambda_q^{\sigma\mu_1} | \Lambda_q^{\sigma\mu_2} \rangle \right| \in [0, 1] , \quad (6.7a)$$

$$0 \leq \theta_q^{\sigma\mu_1\mu_2} \leq \frac{\pi}{2} . \quad (6.7b)$$

Figure 5 illustrates the situation for two subspaces of dimension 1. In this case, the normed basis vector of each subspace already deliver the two principal vectors and the principal angle between them is trivially given by the angle between both one-dimensional lines.

:

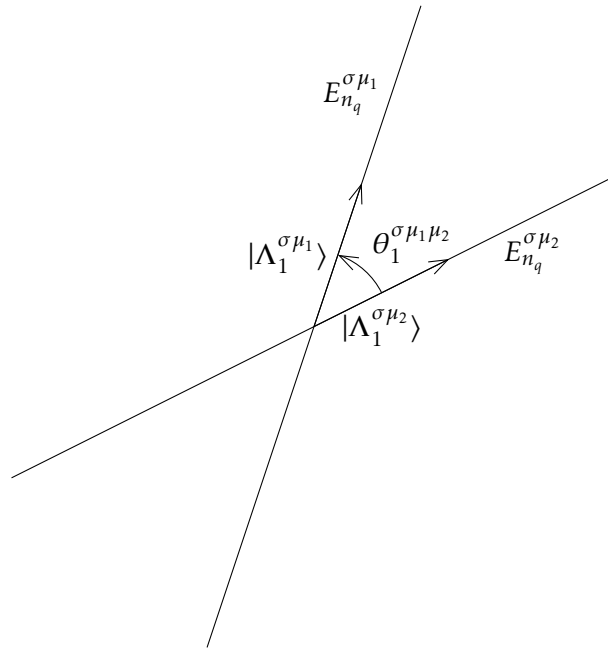


Fig. 5 Schematic illustration of the principal vectors and angles for $n_{\sigma\mu_1}^{\dim} = n_{\sigma\mu_2}^{\dim} = 1$

Figure 6 further illustrates the situation for two subspaces of dimension 2. In this case, the principal vectors are in principle different from the initial basis vectors. In the schematic example the first two principal vectors are identical and the first principal angle is 0. The second principal angle is nothing but the angle formed by the two planes.

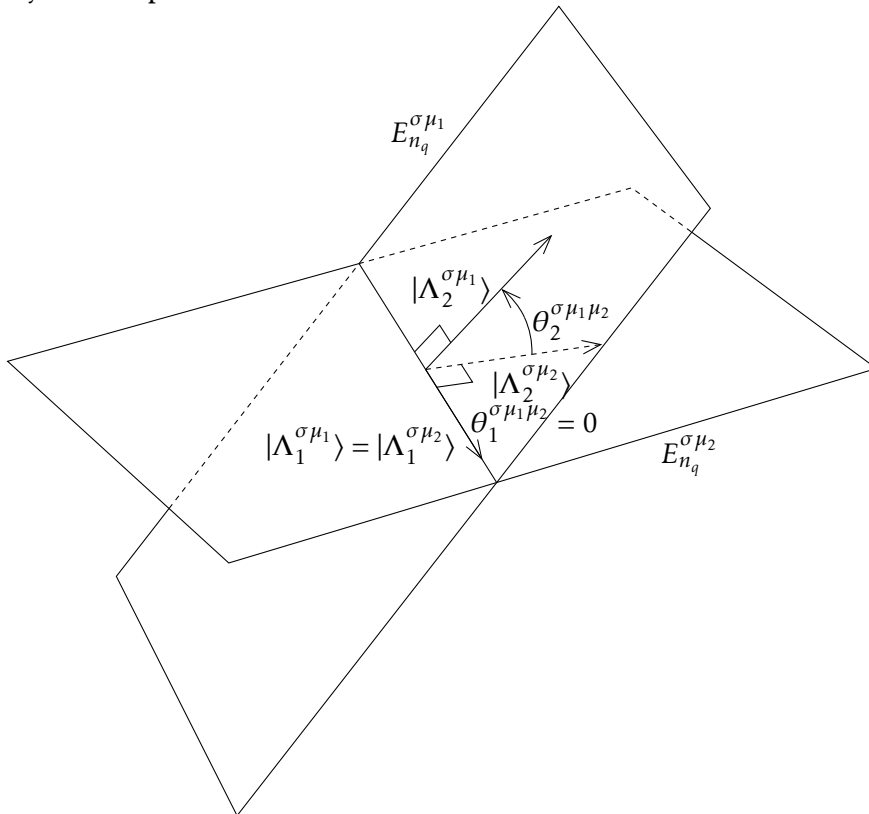


Fig. 6 Schematic illustration of the principal vectors and angles for $n_{\sigma\mu_1}^{\dim} = n_{\sigma\mu_2}^{\dim} = 2$

Geodesic distance

Having the principal angles between both subspaces at hands, their geodesic distance, known as the Grassmann distance, is given by²

$$\delta_p(E_{n_q}^{\sigma\mu_1}, E_{n_q}^{\sigma\mu_2}) \equiv \sqrt{\sum_{q=1}^p (\theta_q^{\sigma\mu_1\mu_2})^2}, \quad (6.10)$$

It is easy to check that d_p is a metric on $\text{Gr}(p, \tilde{\mathcal{F}})$ that is *intrinsic*, i.e. which does not depend on any embedding and that is independent of the dimension of the truncated Fock space $\tilde{\mathcal{F}}$.

Principal angles computation

In practice, the principal vectors and angles are obtained by applying a singular value decomposition (SVD) on the matrix built from the overlap between members of the orthonormal bases of $E_{n_q}^{\sigma\mu_1}$ and $E_{n_q}^{\sigma\mu_2}$, i.e. for $1 \leq q, q' \leq p$

$$\tilde{N}_{qq'}^{\sigma\mu_1\mu_2} \equiv \langle \Xi_q^{\sigma\mu_1} | \Xi_{q'}^{\sigma\mu_2} \rangle. \quad (6.11)$$

The application of the SVD reads as

$$\tilde{N}^{\sigma\mu_1\mu_2} = U^{\sigma\mu_1\mu_2} \Sigma^{\sigma\mu_1\mu_2} V^{\sigma\mu_1\mu_2 T}, \quad (6.12)$$

where $U^{\sigma\mu_1\mu_2}$ ($V^{\sigma\mu_1\mu_2}$) collects the left (right) eigenvectors and where the singular values delivers the principal angles according to

$$\Sigma^{\sigma\mu_1\mu_2} = \text{diag}(\cos \theta_1^{\sigma\mu_1\mu_2}, \dots, \cos \theta_p^{\sigma\mu_1\mu_2}). \quad (6.13)$$

6.3.2 Different dimensions

The distance δ_p is however undefined for subspaces of different dimensions. Fortunately, this problem could be recently addressed [89], inspired by Schubert calculus, knowing that any valid distance between two subspaces can only be a function of their principal angles [90]. It was thus possible to define an intrinsic distance reducing to the Grassmann distance for equal dimensions.

Schubert varieties

Given the two PGCM subspaces $E_{n_q}^{\sigma\mu_1} \in \text{Gr}(p, \tilde{\mathcal{F}})$ and $E_{n_q}^{\sigma\mu_2} \in \text{Gr}(q, \tilde{\mathcal{F}})$ and assuming without any loss of generality that $1 \leq p \leq q \leq \dim \tilde{\mathcal{F}}$, one introduces the two Schubert varieties in $\text{Gr}(q, \tilde{\mathcal{F}})$ and $\text{Gr}(p, \tilde{\mathcal{F}})$, respectively, according to

$$\Omega_+(E_{n_q}^{\sigma\mu_1}) \equiv \{X \in \text{Gr}(q, \tilde{\mathcal{F}}) \mid E_{n_q}^{\sigma\mu_1} \subset X\} \subset \text{Gr}(q, \tilde{\mathcal{F}}), \quad (6.14a)$$

$$\Omega_-(E_{n_q}^{\sigma\mu_2}) \equiv \{Y \in \text{Gr}(p, \tilde{\mathcal{F}}) \mid Y \subset E_{n_q}^{\sigma\mu_2}\} \subset \text{Gr}(p, \tilde{\mathcal{F}}), \quad (6.14b)$$

i.e. $\Omega_+(E_{n_q}^{\sigma\mu_1})$ is the set of q -dimensional linear subspaces of $\tilde{\mathcal{F}}$ containing $E_{n_q}^{\sigma\mu_1}$ whereas $\Omega_-(E_{n_q}^{\sigma\mu_2})$ is the set of p -dimensional linear subspaces of $E_{n_q}^{\sigma\mu_2}$.

²While the Grassmann distance is the geodesic distance, many alternative distances have been defined, e.g. the Asimov distance

$$\delta_\alpha(E_{n_q}^{\sigma\mu}, E_{n_q}^{\sigma L}) \equiv \theta_p^{\sigma\mu_1\mu_2}, \quad (6.8)$$

or the Chordal distance

$$\delta_\kappa(E_{n_q}^{\sigma\mu}, E_{n_q}^{\sigma L}) \equiv \sqrt{\sum_{q=1}^p \sin^2(\theta_q^{\sigma\mu_1\mu_2})}, \quad (6.9)$$

which are all functions of the principal angles.

Distance

With the varieties at hand, the distance between the two subspaces of (possibly) different dimensions is defined as [89]

$$\delta(E_{n_q}^{\sigma\mu_1}, E_{n_q}^{\sigma\mu_2}) \equiv \delta_q(\Omega_+(E_{n_q}^{\sigma\mu_1}), E_{n_q}^{\sigma\mu_2}) \quad (6.15a)$$

$$= \delta_p(E_{n_q}^{\sigma\mu_1}, \Omega_-(E_{n_q}^{\sigma\mu_2})) \quad (6.15b)$$

and is thus nothing but the Grassmann distance between $E_{n_q}^{\sigma\mu_2}$ and the nearest q -dimensional linear subspace containing $E_{n_q}^{\sigma\mu_1}$ or, equivalently, the Grassmann distance between $E_{n_q}^{\sigma\mu_1}$ and the nearest p -dimensional subspace of $E_{n_q}^{\sigma\mu_2}$.

The principal angles between both PGCM subspaces are obtained as before by applying the SVD to the (now rectangular) matrix $\tilde{N}^{\sigma\mu_1\mu_2}$ such that the number of singular values is reduced to $m \equiv \min(p, q)$. With these at hand, the distance reads as³

$$\delta(E_{n_q}^{\sigma\mu_1}, E_{n_q}^{\sigma\mu_2}) = \sqrt{\sum_{n=1}^m (\theta_n^{\sigma\mu_1\mu_2})^2}. \quad (6.16)$$

Eventually, δ indeed agrees with δ_p whenever $p = q$. However, the triangular inequality is not satisfied such that δ is not a metric but a premetric⁴.

Figure 7 illustrates the situation for $n_{\sigma\mu_1}^{\dim} = 1$ and $n_{\sigma\mu_2}^{\dim} = 2$ where one observes that the distance is indeed nothing but the distance between $E_{n_q}^{\sigma\mu_1}$ and the closest one-dimensional subspace of $E_{n_q}^{\sigma\mu_2}$.

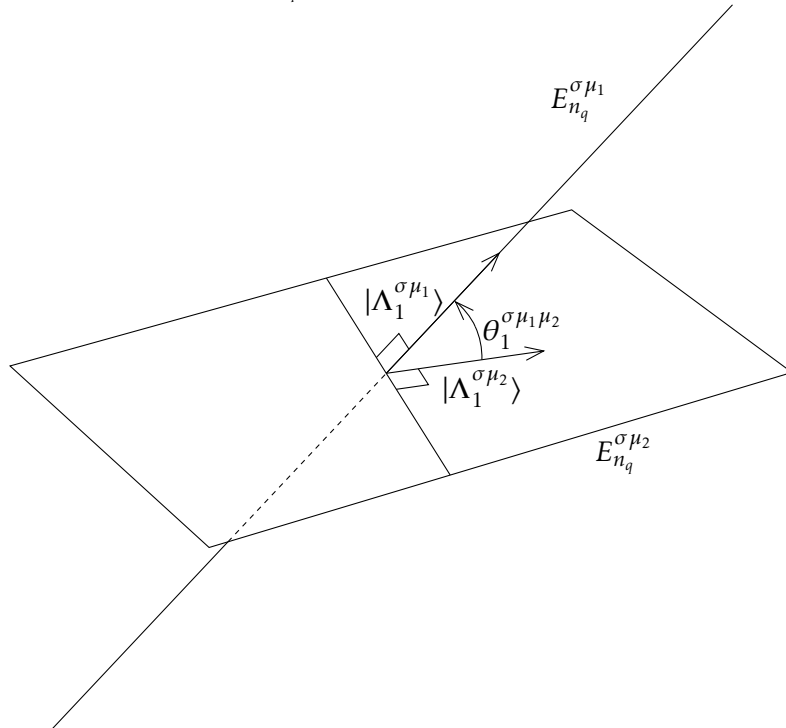


Fig. 7 Schematic illustration of the principal vectors and angles for $n_{\sigma\mu_1}^{\dim} = 1$ and $n_{\sigma\mu_2}^{\dim} = 2$

³Other existing distances between subspaces of equal dimensions, e.g. Asimov or Chordal distances, generalize similarly.

⁴Further generalizations are possible to make it a metric on the so-called doubly infinite Grassmannian $\text{Gr}(\infty, \infty)$ [89].

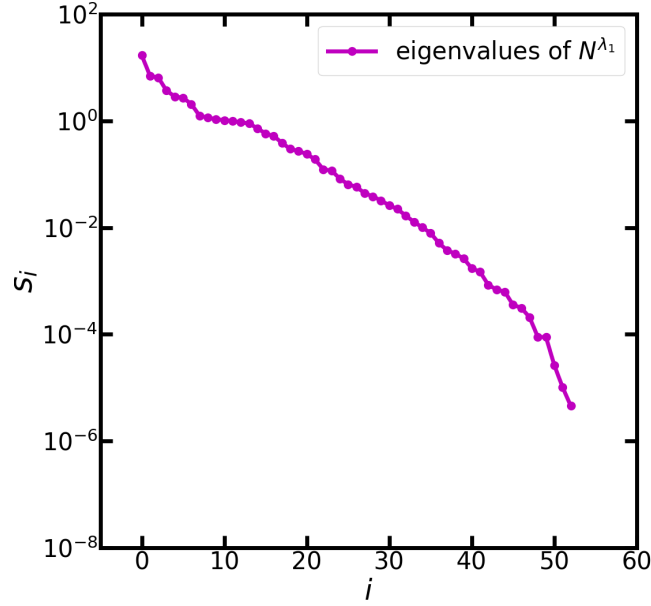


Figure 6.1: Eigenvalues of the norm matrix N^{λ_1} associated with the GCM subspace $E_{n_q}^{\lambda_1}$ with $n_q = 53$ corresponding to the (arbitrary) parameter set λ_1 .

6.3.3 Limit cases

For $E_{n_q}^{\sigma\mu_1}$ a p -dimensional subspace and $E_{n_q}^{\sigma\mu_2}$ a q -dimensional subspace, there are $m = \min(p, q)$ principal angles comprised in the interval $[0, \frac{\pi}{2}]$. Thus, from (6.16) the inequalities

$$0 \leq \delta(E_{n_q}^{\sigma\mu_1}, E_{n_q}^{\sigma\mu_2}) \leq \frac{\pi}{2} \sqrt{m}, \quad (6.17)$$

are satisfied.

The lower bound in Eq. (6.17) is attained if and only if all principal angles are zero, i.e. whenever $E_{n_q}^{\sigma\mu_1} \subset E_{n_q}^{\sigma\mu_2}$ or $E_{n_q}^{\sigma\mu_2} \subset E_{n_q}^{\sigma\mu_1}$. The fact that the distance between two subspaces is zero as soon as one is included into the other is a desired property in the present context as will become clear later on.

The upper bound in Eq. (6.17) is attained if and only if all principal angles equate $\pi/2$, i.e. whenever $E_{n_q}^{\sigma\mu_1}$ and $E_{n_q}^{\sigma\mu_2}$ are orthogonal to each other.

6.4 Numerical tests

The goal is now to validate the computation in both limit cases as well as to investigate the typical distances one encounter in the context of a realistic GCM-EC study. To do so, a simple case is first employed before moving to a situation that is typical of the real situation of present interest.

6.4.1 Inclusion and orthogonality

Let us consider the GCM subspace $E_{n_q}^{\lambda_1}$ with $n_q = 53$ corresponding to the (arbitrary) parameter set λ_1 . The eigenvalues $\{s_i, i = 1, \dots, n_q\}$ of the associated norm matrix N^{λ_1} are displayed in decreasing order in

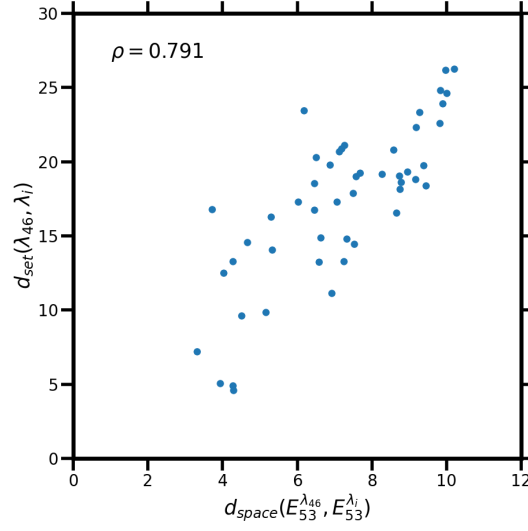


Figure 6.2: Distance in parameter space between λ_{46} and the 49 other parameter sets λ_i against the distance between $E_{53}^{\lambda_{46}}$ and 49 other GCM subspaces $E_{53}^{\lambda_i}$.

Fig. 6.1. The eigenvalues span about 7 orders of magnitude, the smallest being equal to 4.5×10^{-6} and the largest to 1.6×10^1 .

Next, the $1 \leq n_{\lambda_1}^{\text{dim}} \leq n_q$ largest eigenvalues are chosen according to the truncation $s_i \geq \epsilon^{\lambda_1}$ to build the orthogonal basis $\{|\Xi_i^{\lambda_1}\rangle, i = 1, \dots, n_{\lambda_1}^{\text{dim}}\}$ spanning the approximation to $E_{n_q}^{\lambda_1}$. For a given value of $n_{\lambda_1}^{\text{dim}}(\epsilon^{\lambda_1})$, the subspace $U_p \subset E_{n_q}^{\lambda_1}$ spanned by the $1 \leq p \leq n_{\lambda_1}^{\text{dim}} - 1$ first vectors $\{|\Xi_i^{\lambda_1}\rangle, i = 1, \dots, p\}$ is introduced. Given U_p , one further defines

1. the subspace $V_q \subset E_{n_q}^{\lambda_1}$ spanned by the $1 \leq q \leq p$ first vectors $\{|\Xi_j^{\lambda_1}\rangle, j = 1, \dots, q\}$ such that $V_q \subset U_p$. In this case, numerical calculations of subspace distances gives $\delta(U_p, V_q) = 0$ up to numerical accuracy.
2. The subspace $W_m \subset E_{n_q}^{\lambda_1}$ spanned by the $1 \leq m \leq n_{\lambda_1}^{\text{dim}} - p$ last vectors $\{|\Xi_j^{\lambda_1}\rangle, j = p + 1, \dots, n_{\lambda_1}^{\text{dim}}\}$ such that W_m is orthogonal to U_p . In this case numerical calculations gives $\delta(U_p, W_m) = \frac{\pi}{2} \sqrt{\min(p, m)}$ up to numerical accuracy.

This numerical computations validates that the orthonormality of the basis vectors $\{|\Xi_i^{\lambda_1}\rangle, i = 1, \dots, n_{\lambda_1}^{\text{dim}}(\epsilon^{\lambda_1})\}$ is numerically satisfied along with the null distance between a given subspace and one included into it.

6.4.2 Distances between GCM subspaces

Let us now consider the 50 GCM subspaces $E_{n_q}^{\lambda_i}, i = 1, \dots, 50$, each originating from $n_q = 53$ non-orthogonal HF states and being associated with a specific parameter set λ_i . The diagonalization of the norm matrix N^{λ_i} and the truncation of its eigenvalues according to the thresholds ϵ^{λ_i} delivers the orthogonal basis $\{|\Xi_j^{\lambda_i}\rangle, j = 1, \dots, n_{\lambda_i}^{\text{dim}}\}$ spanning (the approximation to) $E_{n_q}^{\lambda_i}$. In practice, the convergence pattern observed in Chap. 4 for the nominal GCM spectrum is the same for all parameter set λ_i such that all 53 eigenvalues can safely be kept, i.e. $n_{\lambda_i}^{\text{dim}} = n_q = 53$ for $i = 1, \dots, 50$.

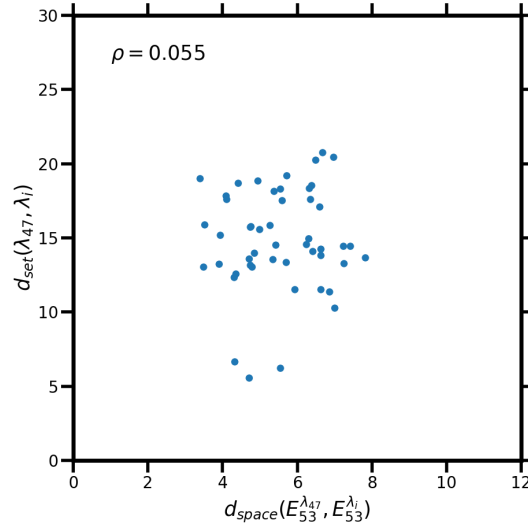


Figure 6.3: Same as in Fig. 6.2 for λ_{47} and $E_{53}^{\lambda_{47}}$.

In Fig. 6.2 (6.3), the distance between $E_{53}^{\lambda_{46}}$ ($E_{53}^{\lambda_{47}}$) and the 49 other GCM subspaces is plotted against the corresponding distance in parameter space. Noticing that the maximum distance between two subspaces of dimension 53 is $\pi\sqrt{53}/2 \approx 11.43$ whenever they are orthogonal, one observes that $\delta(E_{53}^{\lambda_{46}}, E_{53}^{\lambda_i})$ covers a rather large range of values between about 3 and 10 such that certain subspaces are not far from being orthogonal to $E_{53}^{\lambda_{46}}$ whereas others have a strong overlap with it. In the second case, the span is reduced, i.e. $\delta(E_{53}^{\lambda_{47}}, E_{53}^{\lambda_i})$ varies from about 3 to about 7. These two cases represent extreme situations in this respect such that any arbitrarily chosen GCM subspace among the 50 presently under consideration would all lie somewhat in between. It seems in particular that the minimal distance between any two GCM subspaces among the 50 generated via the LHS in parameter space described in Chap. 4 is around 3.

Furthermore, one observes in Fig. 6.2 and 6.3 that the distance between subspaces and the distance in parameter space are not strongly correlated, i.e. while the Pearson correlation coefficient (PCC) ρ is equal to 0.79 in the first case, it is only equal to 0.05 in the second case. Overall, the distance in parameter space does not constitute a safe indicator of the actual distance between subspaces such that it is not used any further in the following.

6.4.3 Distance to training subspace

Let us now proceed to the incremental reunion of the first $n_t = 1, \dots, 40$ among the 50 orthonormal bases defined above to set up the training subspaces $E_{n_q}^{L_{n_t}}$ associated with the training parameter sets L_{n_t} . Building and diagonalizing the *super* norm matrix $\tilde{N}^{L_{n_t}}$, before truncating its eigenvalues according to the *super* threshold $\epsilon^{L_{n_t}}$, provides an orthonormal basis of (the approximation to) $E_{n_q}^{L_{n_t}}$ with effective dimension $n_{L_{n_t}}^{\text{dim}}$.

Figure 6.4 compares the eigenvalues of $\tilde{N}^{L_{40}}$ with those of N^{λ_1} already shown in Fig. 6.1. While the latter span 7 orders of magnitude, the former now span 12 orders of magnitude, all the way down to 10^{-11} . The fact that the eigenvalues of $\tilde{N}^{L_{n_t}}$ reach much smaller values results from the dramatic increase with n_t of the colinearity between the vectors gathered to span $E_{n_q}^{L_{n_t}}$ compared to the case $n_t = 1$ studied above via $E_{n_q}^{\lambda_1}$.

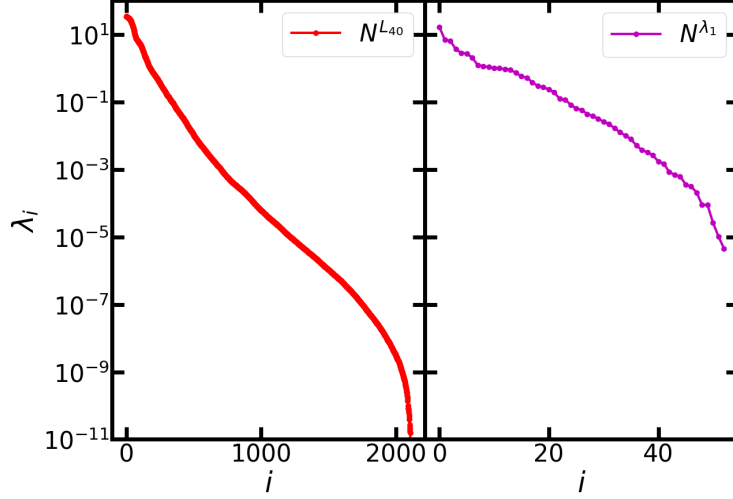


Figure 6.4: Eigenvalues of the norm matrices $\tilde{N}^{L_{40}}$ (left) and N^{λ_1} (right).

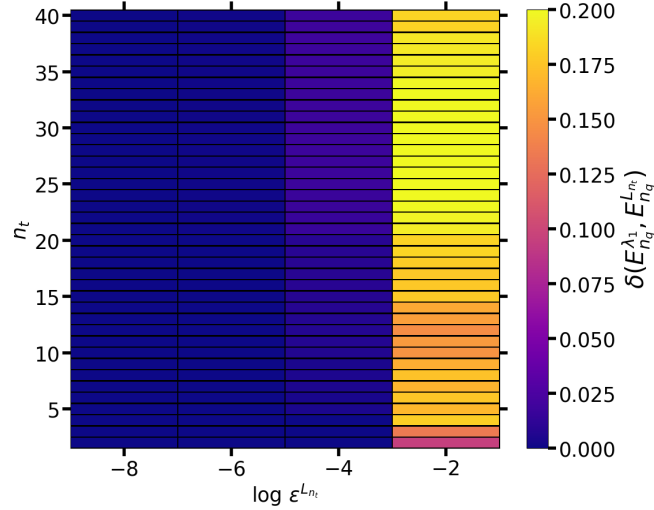


Figure 6.5: Distance $\delta(E_{n_q}^{\lambda_1}, E_{n_q}^{L_{n_t}})$ against the super threshold $\epsilon^{L_{n_t}}$ and the number n_t of training GCM spaces gathered to form the training space $E_{n_q}^{L_{n_t}}$. All GCM subspaces are built out of $n_q = 53$ non-orthogonal constrained HF states.

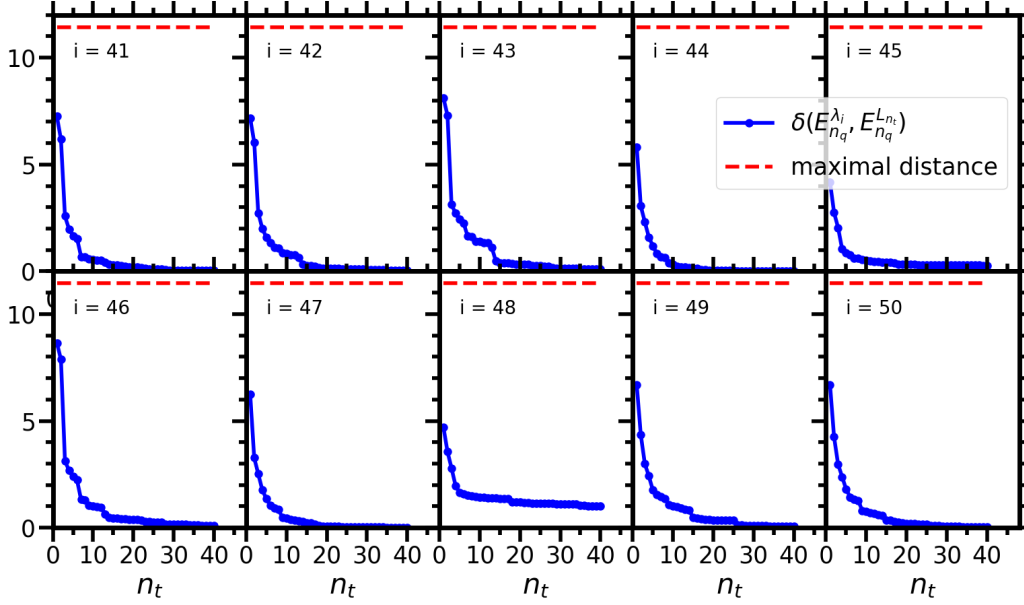


Figure 6.6: Distance $\delta\left(E_{n_q}^{L_{n_t}}, E_{n_q}^{\lambda_i}\right)$, $i = 41, \dots, 50$, against n_t . Each of the 50 involved GCM subspace is built out of $n_q = 53$ non-orthogonal constrained HF states and is such that $n_{\lambda_i}^{\dim} = n_q$. The super threshold is taken to be $\epsilon^{L_{n_t}} = 10^{-8}$ for all n_t . The maximum distance $\pi\sqrt{53}/2 \approx 11.43$ that would be reached if the two subspaces were orthogonal is also shown.

Taking $n_t = 40$ as an example, Fig. 6.5 displays the distance $\delta\left(E_{n_q}^{\lambda_1}, E_{n_q}^{L_{n_t}}\right)$ between the GCM subspace $E_{n_q}^{\lambda_1}$ and the training subspace against n_t and the super threshold $\epsilon^{L_{n_t}}$. Since by construction $E_{n_q}^{\lambda_1}$ is always among the GCM subspaces used for the training, its distance to the training subspace is expected to be zero. This is indeed true for all n_t , except when the super threshold $\epsilon^{L_{n_t}}$ becomes greater than 10^{-6} . Indeed, in this case the orthonormal basis of $E_{n_q}^{L_{n_t}}$ becomes more and more drastically truncated such that the inclusion of $E_{n_q}^{\lambda_1}$ into it becomes in fact compromised. To avoid such an artifact and safely compute the distance between a given GCM subspace and the training subspace, the present analysis indicates that the super threshold must satisfy $\epsilon^{L_{n_t}} \leq 10^{-6}$ as soon as $n_t > 4$.

Next, the distance between the training subspace $E_{53}^{L_{n_t}}$ and the 10 GCM subspaces $E_{53}^{\lambda_i}$, $i = 41, \dots, 50$, is displayed in Fig. 6.7 as a function of n_t . For $n_t = 1$, the training subspace reduces to (the arbitrarily chosen) subspace $E_{53}^{\lambda_1}$ such that the distance $\delta\left(E_{53}^{\lambda_1}, E_{53}^{\lambda_i}\right)$ is equal to 6.5 on average with a dispersion of 1.3. Such a span is similar to the one visible in Fig. 6.3 for $E_{53}^{\lambda_{47}}$ ⁵. As n_t grows, the distance $\delta\left(E_{53}^{L_{n_t}}, E_{53}^{\lambda_i}\right)$ decreases rapidly and quasi exponentially for (essentially) all $i = 41, \dots, 50$. As such, the distance reduces to 2.8 (0.4) on average for $n_t = 3$ ($n_t = 15$) with a dispersion of 0.3 (0.3). Eventually, the average distance reaches 0.2 for $n_t = 40$ with an asymmetric distribution associated with the dispersion 0.3. As a matter of fact, two among the 10 randomly tested GCM subspaces retain anomalously large distances for $n_t = 40$, e.g. $\delta\left(E_{53}^{L_{40}}, E_{53}^{\lambda_{48}}\right) \sim 1$, which indicates that these two subspaces are not fully emulated by the training subspace

⁵Notice that only 10 different distances are computed in the present case whereas Fig. 6.3 displays the distance between $E_{53}^{\lambda_{47}}$ and 49 other subspaces.

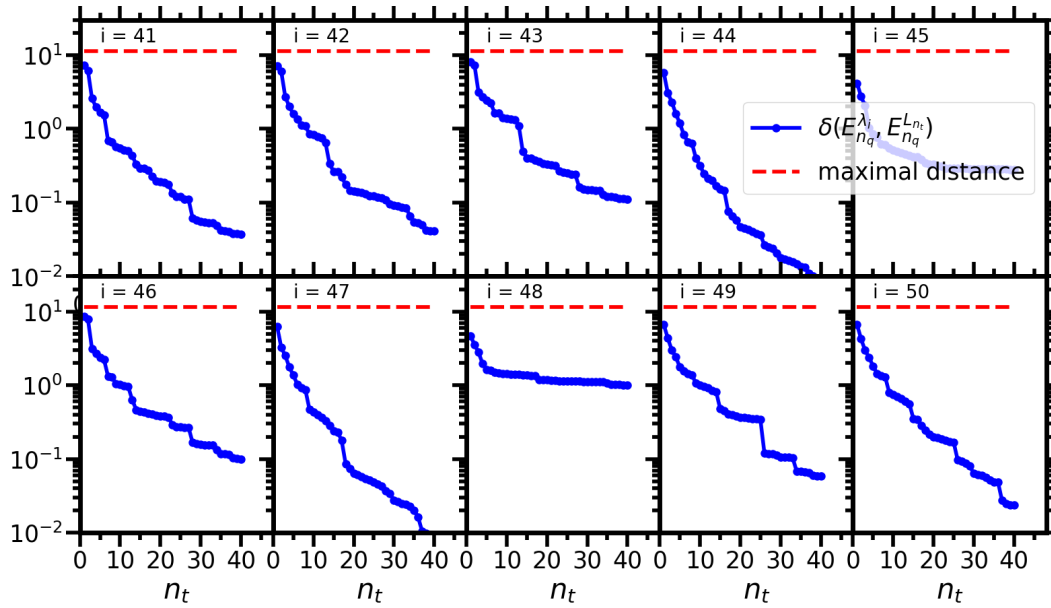


Figure 6.7: Same figure as Fig. 6.6, in logarithmic scale.

gathering 40 GCM subspaces.

One further observes that the distance between a given subspace and the training subspace drops abruptly for certain values of n_t . Taking $E_{53}^{\lambda_{41}}$ as an arbitrary example, the distance to the training subspace decreases gradually as a function of n_t except for $n_t = 3, 7$ and 28 for which a sudden reduction is identified, with additional smaller drops along the way. As visible in Fig. 6.8, such sudden drops correlate with the addition of a subspace that is particularly close to $E_{53}^{\lambda_{41}}$. This is especially true of the first drop where the distance to the training subspace closely reflects the distance to the added subspace. As the size of the training space grows, adding a GCM subspace that is particularly close to the tested subspace does not necessarily translate into a sudden drop of the distance to the training subspace given that the distance to the latter is already very small. Still, whenever a drops occurs, it corresponds to the addition of a particularly close subspace to the tested subspace.

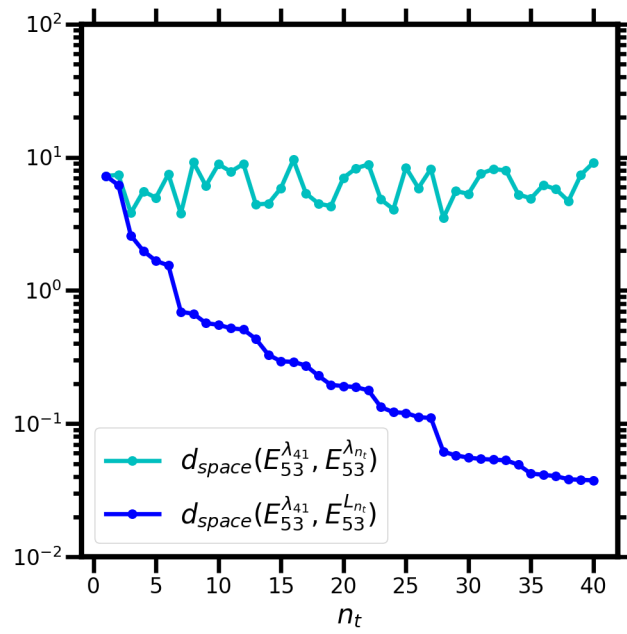


Figure 6.8: Distances $\delta(E_{53}^{L_{n_t}}, E_{53}^{\lambda_{41}})$ and $\delta(E_{53}^{\lambda_{n_t}}, E_{53}^{\lambda_{41}})$ as a function of n_t .

Chapter 7

Training regimes in PGCM-EC

Contents

| | |
|--|----|
| 7.1 Error versus distance to training subspace | 79 |
| 7.2 Training regimes | 81 |
| 7.3 Conclusions | 81 |

Results of the PGCM-EC emulator exposed in Chap. 5 are presently analyzed using the distance between subspaces introduced in Chap. 6.

7.1 Error versus distance to training subspace

The first objective of the present chapter is to study the correlation between the error associated with a given validation point λ_i and the distance

$$d_{\text{space}} \equiv \delta \left(\mathbf{E}_{53}^{\lambda_i}, \mathbf{E}_{53}^{L_{n_t}} \right) \quad (7.1)$$

between the corresponding GCM subspace and the training subspace. To do so, the error on $E_0^{\lambda_i}$ (top panels), $E_1^{\lambda_i}$ (middle panels) and $E_1^{\lambda_i} - E_0^{\lambda_i}$ (bottom panels) for each of the 36 validation points is plotted in Fig. 7.1 against d_{space} for three sizes of the training space, i.e. $n_t = 1$ (left panels), $n_t = 2$ (middle panels) and $n_t = 14$ (right panels). In each panel, the mean error over the 36 validation points is reported along with the Pearson correlation coefficient ρ .

Overall, the mean error strongly decreases with n_t , which is consistent with the data presented in Fig. 5.1. The same is true about the mean distance and its dispersion, which is consistent with the analysis performed in Sec. 6.4.3. For $n_t = 1$, the error on $E_0^{\lambda_i}$ and $E_1^{\lambda_i}$ is strongly correlated with $d_{\text{space}} \in [3.5, 9.3]$. This is also true, even though to a lesser extent, for the excitation energy. Looking more closely, one observes that the larger the distance, the stronger the correlation. Since for $n_t = 2$ all distances to the training subspace are below 5, the error on the individual energies correlates already less significantly and not at all for their difference. For $n_t = 14$, all distances are below 3 and no trace of correlation persists.

The above result demonstrates that the strong under training at play for $n_t = 1$ quickly weakens as the size of the training subspace increases. Still, even for $n_t = 14$ the distance between the GCM subspace to the training subspace is different from zero for many validation points such that a slight undertraining remains. This is consistent with the observation made in connection with Fig. 5.5. As seen from Fig. 6.7, the number of training points n_t would need to be doubled to reduce all distances by another order of magnitude and thus fully overcome the under training. However, the more n_t grows, the more the over training increases at the same time.

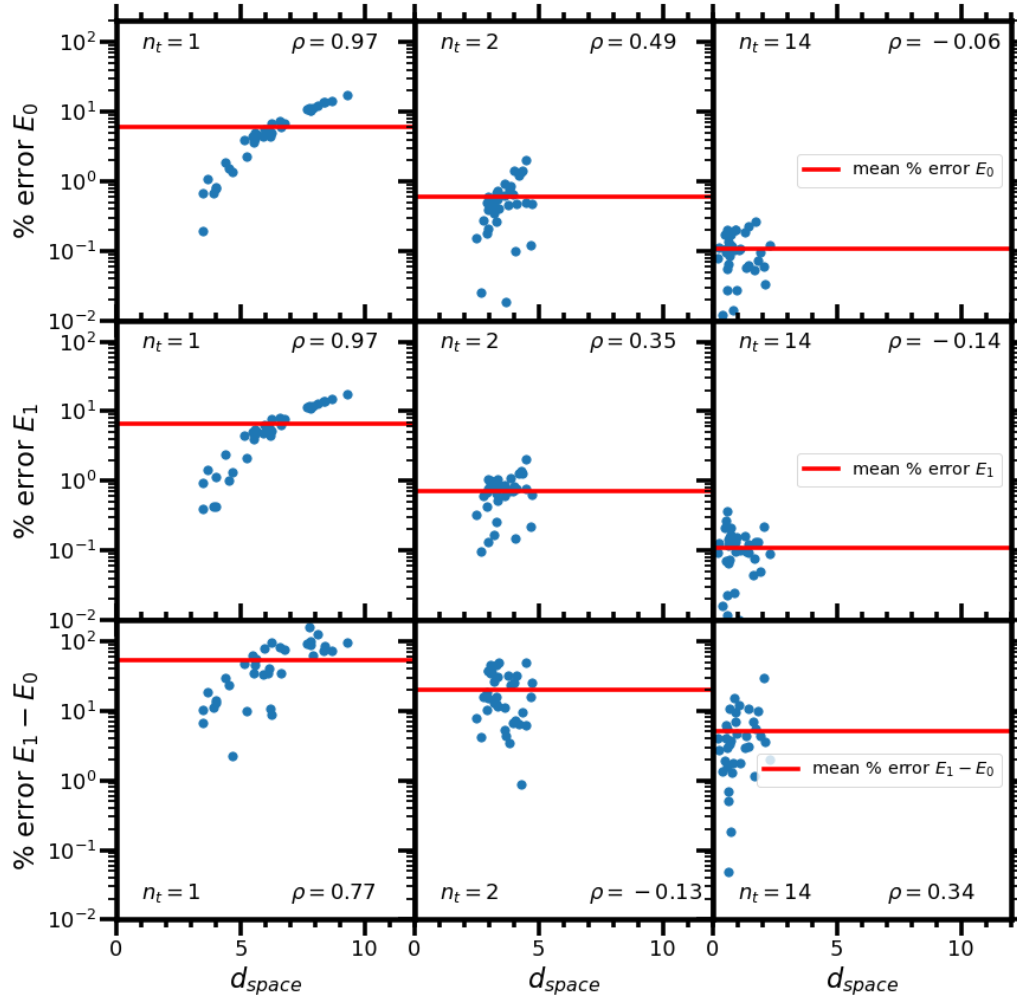


Figure 7.1: mean relative errors (%) on $E_0^{\lambda_i}$ (top panels), $E_1^{\lambda_i}$ (middle panels) and $E_1^{\lambda_i} - E_0^{\lambda_i}$ (bottom panels) for the 36 validation points against the subspace distance d_{space} , for $n_t = 1$ (left panels), $n_t = 2$ (middle panels) and $n_t = 14$ (right panels).

7.2 Training regimes

Figure 7.2 displays the mean error over the validation set on $E_0^{\lambda_i}$ (top panel), $E_1^{\lambda_i}$ (middle panel) and $E_1^{\lambda_i} - E_0^{\lambda_i}$ (bottom panel) against the mean distance for $1 \leq n_t \leq 14$. First, the figure confirms that the mean distance decreases monotonically with n_t . Second, three different regimes can be identified for the error on individual energies

1. for $1 \leq n_t \leq 4$, the mean error decreases steadily by two orders of magnitude,
2. for $5 \leq n_t \leq 6$, the mean error is minimal around 0.1% with a mean distance around 2,
3. for $7 \leq n_t \leq 14$, the mean error grows again slowly, eventually reaching 0.2%.

These three phases can be identified with (1) an under training regime, (2) an optimal training regime and (3) an over training regime, respectively.

For the excitation energy $E_1^{\lambda_i} - E_0^{\lambda_i}$, the three phases do not appear and one only observes a slow, yet steady, decrease of the error from 20% down to 6% for $1 \leq n_t \leq 14$. In particular, the effect of the over training cancels out in the phase ($n_t \geq 7$) where it dominates the error for individual energies. Under the hypothesis that this remains true when further increasing n_t , one may hope to bring the error on excitation energies further down if necessary by pushing the training beyond $n_t = 14$.

7.3 Conclusions

With the help of the computable distance between an arbitrary (P)GCM subspace and the training subspace, it was possible to isolate three different regimes for the performance of the (P)GCM-EC emulator as a function of n_t , i.e. an under training when n_t is too small for the training subspace to properly emulate the (P)GCM subspace of interest, an optimal training regime for intermediate values and an over training phase where the (P)GCM subspace is (essentially) well emulated at the price of working with a training space that completely supersedes it. The corresponding situation is schematically represented in Fig. 7.3.

The fact that the over training dominates when increasing n_t prevents from diminishing the error on individual energies below 0.1%. This is not a problem in practice given that such an error is largely subleading compared to other sources of error in current ab initio calculations. The error reached with the (P)GCM-EC emulator on low-lying excitation energies is of the order of 5%. While already satisfying, one may want to further reduce it, e.g. when studying higher-lying states such as giant resonances [44, 45, 46]. Thankfully, excitation energies seem to be less prone to the over training thanks to its cancellation in energy differences. Consequently, one may hope that pushing the training beyond what was presently done can further reduce the error. This will have to be verified in a future study.

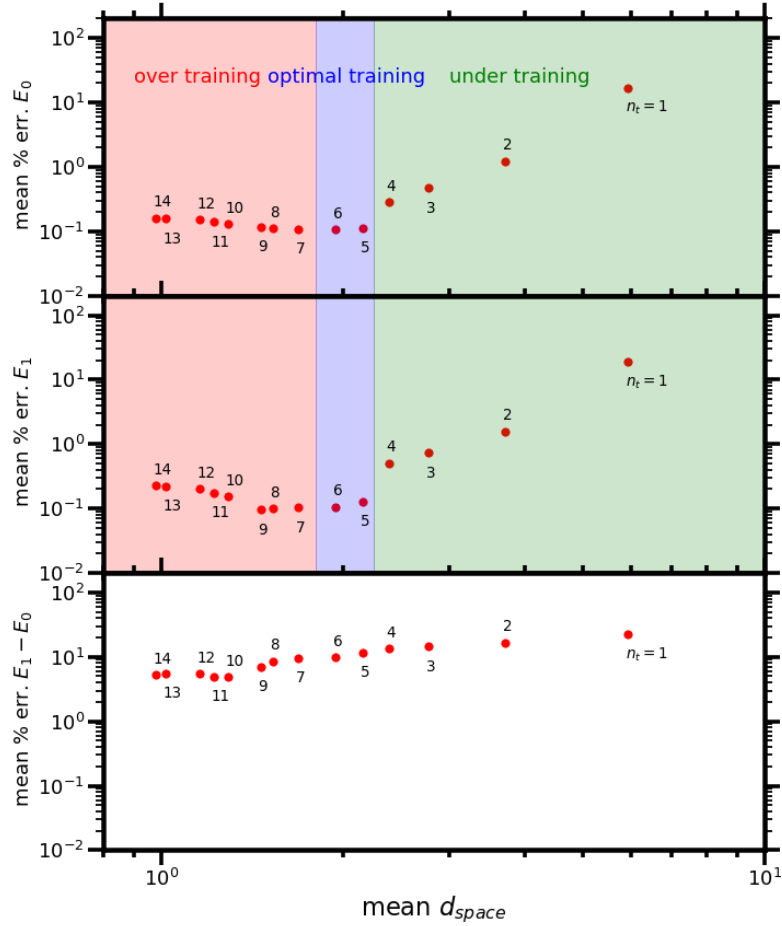


Figure 7.2: Mean error on $E_0^{\lambda_i}$ (top panel), $E_1^{\lambda_i}$ (middle panel) and $E_1^{\lambda_i} - E_0^{\lambda_i}$ (bottom panel) as a function of the mean subspace distance for $1 \leq n_t \leq 14$. The means are taken over the 36 validation points. Regimes of under training, optimal training and over training are highlighted.



Figure 7.3: Schematic illustration of the three training regimes. At first, the (P)GCM subspace corresponding to a given simulation (purple) is imperfectly reproduced by a too small training space (green). In a second phase, the emulation of the (P)GCM subspace constitutes an optimal compromise (blue). Eventually, the (P)GCM subspace is well emulated at the price of a too large training space inducing a non-negligible over training (red).

Chapter 8

Conclusions

The projected generator coordinate method provides the zero-order contribution to the perturbative expansion built on top of it [47]. While total energies require the further inclusion of correlations on top of the PGCM, excitation energies of low-lying collective states are already well converged at the PGCM level [49, 48]. In this context, the present thesis explored the possibility to accurately emulate PGCM simulations via the eigenvector continuation method. The objective is eventually to emulate millions of PGCM simulations at low computational cost to perform sensitivity analyses on the interaction parameters and propagate their uncertainties to many-body observables.

The preliminary study performed in the present work was based on a simple Brink-Boeker two-body interaction. While the Brink-Boeker contains a subset of the terms making up the effective Gogny interaction, all matrix elements of the latter were re-derived and implemented in the PAN@CEA numerical solver. The latter solver was further adapted to train the emulator and perform PGCM-EC emulations for a large number of parameter sets generated via the latin hypercube sampling method.

Based on realistic GCM calculations of ^{20}Ne including both axial quadrupole and octupole deformations, the accuracy of the GCM-EC emulator was investigated for total energies, excitation energies and matter radii of low-lying states. Because of the present lack of angular-momentum restoration, the emulation of electromagnetic transitions was left to a future study. Varying 4 parameters of the Brink-Boeker interaction, up to 14 training sets were generated using a brute-force learning method. Based on 36 validation sets, the GCM-EC was shown to deliver an accurate reproduction of absolute energies ($\sim 0.1 - 0.2\%$ error), excitation energies ($\sim 5 - 6\%$ error) and matter radii ($\sim 0.2 - 0.6\%$ error) of the low-lying GCM states. To achieve such performances, it was shown to be mandatory to train the emulator on the excited states of interest.

While sufficient in practice, the lower bound reached on the error was shown to result from two (compensating) errors that are intimately related to the nature of the (P)GCM

1. an *over* training due to the growing dimension of the training space that largely supersedes the subspace characterizing a (P)GCM simulation,
2. an *under* training induced by the imperfect spanning of a given (P)GCM subspace by the training subspace.

In order to quantify the imperfect spanning of a given (P)GCM subspace by the training subspace, the distance between any two subspaces of the complete Hilbert space was introduced and implemented in the numerical solver. Based on such a tool, three different regimes for the performance of the (P)GCM-EC emulator were identified, i.e. an under training regime when the number of training points is too small for the training subspace to properly emulate the (P)GCM subspace of interest, an optimal training regime obtained for an intermediate number of training points and an over training regime where the

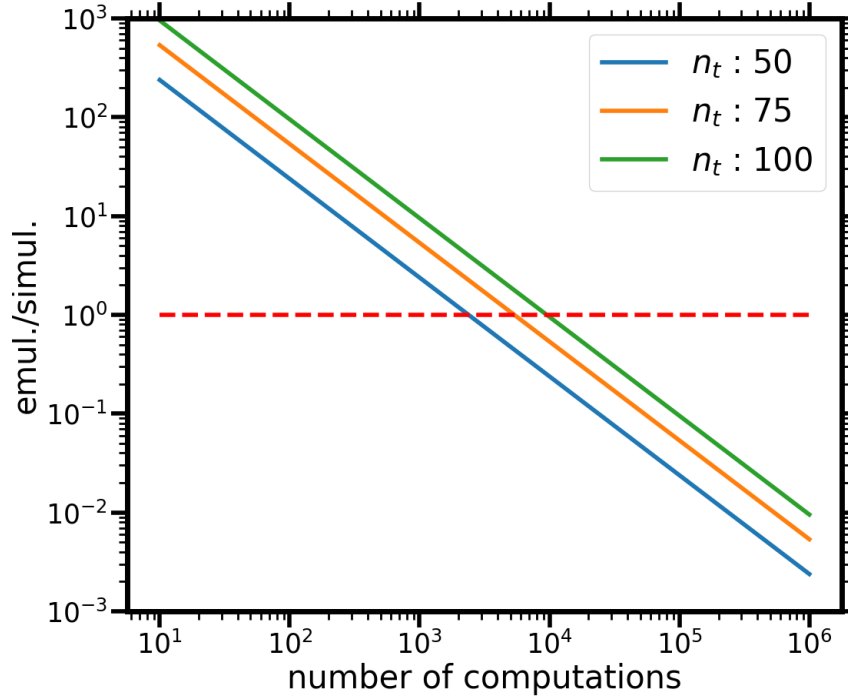


Figure 8.1: Ratio in ^{20}Ne of the GCM-EC emulation time over the GCM simulation time is displayed in Fig.8.1 as a function of the number of computations for three training set sizes $n_t = 50, 75, 100$.

(P)GCM subspace is (essentially) well emulated at the price of working with a training space that completely supersedes it.

While the over training prevents from diminishing the error of the emulator on total energies below 0.1%, it seems possible to bring the error on excitation energies below the 5% presently reached using 14 training points thanks to a cancellation of the over training in energy differences. This would be necessary to study higher-lying states such as giant resonances.

Based on the present thesis, the next step will consists of

1. including angular-momentum restoration to extend the present work to the full PGCM and the emulation of electromagnetic transitions,
2. pushing the study to larger numbers of training and validation points,
3. performing a similar study for χEFT interactions,
4. implementing statistical tools to perform sensitivity analysis and uncertainty propagation,
5. performing large-scale *ab initio* PGCM calculations accompanied with interaction uncertainties.

To anticipate the expected gain in large-scale applications, the ratio in ^{20}Ne of the GCM-EC emulation time over the GCM simulation time is displayed in Fig.8.1 as a function of the number of computations for three training set sizes $n_t = 50, 75, 100$. For a given training set size, the gain increases linearly with the number of computations. Targeting one million computations, which is the order of magnitude necessary to perform controlled statistical analysis [53], the GCM-EC emulator is about 100 to 1000 less expensive

than the GCM simulator. This gain will be even much greater once the restoration of symmetries is taken into account.

Part I

Appendices

Appendix A

Symmetry group

The existence of continuous symmetries in finite systems is linked to conservation laws, such as the particle number conservation arising from $U(1)$ global gauge symmetry and angular momentum conservation arising from $SU(2)$ symmetry. The symmetry group of the nuclear Hamiltonian H leaving the system invariant is defined as

$$G_H \equiv SU(2) \times I \times U(1)_N \times U(1)_Z, \quad (\text{A.1})$$

and is associated with the conservation of total angular momentum, parity and neutron/proton numbers. The group G_H is a compact Lie group, although non Abelian due to $SU(2)$.

A.1 Unitary representation

Each subgroup is represented on Fock space \mathcal{F} via the set of unitary rotation operators

$$R_{\vec{J}}(\Omega) \equiv e^{-i\alpha J_z} e^{-i\beta J_y} e^{-i\gamma J_x}, \quad (\text{A.2a})$$

$$\Pi(\phi_\pi) \equiv e^{-i\phi_\pi F}, \quad (\text{A.2b})$$

$$R_N(\phi_n) \equiv e^{-i\phi_n N}, \quad (\text{A.2c})$$

$$R_Z(\phi_p) \equiv e^{-i\phi_p Z}, \quad (\text{A.2d})$$

where $\Omega \equiv (\alpha, \beta, \gamma)$, ϕ_π and ϕ_n (ϕ_p) denote Euler, parity and neutron- (proton-) gauge angles, respectively. The one-body operators entering in Eqs. (A.2) denote the generators of the group made out of the three components of the total angular momentum $\vec{J} = (J_x, J_y, J_z)$, neutron- (proton-) number N (Z) operators as well as the one-body operator

$$F \equiv \sum_{\alpha\beta} f_{\alpha\beta} c_\alpha^\dagger c_\beta \quad (\text{A.3})$$

defined through its matrix elements

$$f_{\alpha\beta} \equiv \frac{1}{2}(1 - \pi_\alpha)\delta_{\alpha\beta}, \quad (\text{A.4})$$

where π_α denotes the parity of the corresponding one-body basis state.

The irreducible representations of the group are given by

$$\langle \Psi_\mu^\sigma | R(\theta) | \Psi_{\mu'}^{\sigma'} \rangle \equiv D_{MM'}^{\vec{\sigma}}(\theta) \delta_{\sigma\sigma'} \delta_{\mu\mu'}, \quad (\text{A.5})$$

with $\vec{\sigma} \equiv (J\Pi NZ)$ and

$$D_{MM'}^{\vec{\sigma}}(\theta) \equiv D_{MM'}^J(\Omega) e^{-i(1-\pi)\phi_\pi/2} e^{-i\phi_n N} e^{-i\phi_p Z}, \quad (\text{A.6})$$

and where the rotation operators have been gathered into

$$R(\theta) \equiv R_{\vec{J}}(\Omega)\Pi(\phi_\pi)R_N(\phi_n)R_Z(\phi_p), \quad (\text{A.7})$$

with

$$\theta \equiv (\Omega, \phi_\pi, \phi_n, \phi_p) \quad (\text{A.8})$$

collecting all rotation angles.

A.2 Projection operators

The operator

$$P^\sigma \equiv P_M^J P^\Pi P^N P^Z \quad (\text{A.9})$$

collects the projection operators on good symmetry quantum numbers

$$\begin{aligned} P_M^J &\equiv \sum_K g_K P_{MK}^J \\ &\equiv \sum_K g_K \frac{2J+1}{16\pi^2} \int_{[0,4\pi] \times [0,\pi] \times [0,2\pi]} d\Omega D_{MK}^{J*}(\Omega) R_{\vec{J}}(\Omega), \end{aligned} \quad (\text{A.10a})$$

$$P^\Pi \equiv \frac{1}{2} \sum_{\phi_\pi=0,\pi} e^{i(1-\pi)\phi_\pi/2} \Pi(\phi_\pi), \quad (\text{A.10b})$$

$$P^N \equiv \frac{1}{2\pi} \int_0^{2\pi} d\phi_n e^{i\phi_n N} R_N(\phi_n), \quad (\text{A.10c})$$

$$P^Z \equiv \frac{1}{2\pi} \int_0^{2\pi} d\phi_p e^{i\phi_p Z} R_Z(\phi_p). \quad (\text{A.10d})$$

Appendix B

Hill-Wheeler-Griffin equation

In general, the first order variation of $\mathcal{E} = \frac{\langle \Psi | H | \Psi \rangle}{\langle \Psi | \Psi \rangle}$ as $|\Psi\rangle \mapsto |\Psi\rangle + |d\Psi\rangle$ satisfies

$$\langle \Psi | \Psi \rangle d\mathcal{E} = \langle d\Psi | H | \Psi \rangle + \langle \Psi | H | d\Psi \rangle - \mathcal{E}[\Psi](\langle d\Psi | \Psi \rangle + \langle \Psi | d\Psi \rangle) . \quad (\text{B.1})$$

Given a sequence $|\phi_i\rangle_{1 \leq i \leq n}$ in Fock space \mathcal{F} , define V to be the linear subspace of \mathcal{F} generated by $|\phi_i\rangle_{1 \leq i \leq n}$, one has

Theorem B.0.1. *\mathcal{E} is extremal at*

$$|\Psi\rangle = \sum_{i=1}^n a_i |\phi_i\rangle \in V , \quad (\text{B.2})$$

on V if and only if for every $1 \leq i \leq n$

$$\sum_{j=1}^n a_j (\langle \phi_i | H | \phi_j \rangle - \mathcal{E}[\Psi] \langle \phi_i | \phi_j \rangle) = 0 . \quad (\text{B.3})$$

Proof. Using Eq. (B.1), \mathcal{E} is extremal at Ψ on V if and only if, for arbitrary $|h\rangle \in V$

$$\langle h | H | \Psi \rangle + \langle \Psi | H | h \rangle - \mathcal{E}(\langle h | \Psi \rangle + \langle \Psi | h \rangle) = 0 . \quad (\text{B.4})$$

Combining Eq. (B.4) with the equation obtained by replacing $|h\rangle$ by $i|h\rangle$ in Eq. (B.4), one obtain that Eq. (B.4) is equivalent to

$$\langle h | H | \Psi \rangle - \mathcal{E} \langle h | \Psi \rangle = 0 , \quad (\text{B.5})$$

for arbitrary $|h\rangle \in V$. Finally, the definition of V and Eq. (B.2) imply the equivalence of Eq. (B.5) with Eq. (B.3). \square

Appendix C

Talman coefficients and integral relations

C.1 Talman coefficients

The product of two cartesian and polar harmonic oscillator functions may be expanded as (Ref. [79], Eqs. (C1) and (C7))

$$\psi_{n_1}^{(1)}(z; b_z) \psi_{n_2}^{(1)}(z; b_z) = \frac{e^{-z^2/2b_z^2}}{\sqrt{b_z} \sqrt{\pi}} \sum_n T_{n_1 n_2}^{(1)n} \psi_n^{(1)}(z; b_z) , \quad (\text{C.1})$$

$$\psi_{m_1 n_1}^{(2)*}(r, \varphi; b_r) \psi_{m_2 n_2}^{(2)}(r, \varphi; b_r) = \frac{e^{-r^2/2b_r^2}}{b_r \sqrt{\pi}} \sum_n T_{m_1 n_1 m_2 n_2}^{(2)n} \psi_{m_2 - m_1 n}^{(2)}(r, \varphi; b_r) . \quad (\text{C.2})$$

From Ref. [80], the Talman T coefficients can be expressed as

$$T_{n_1, n_2}^{(1)n} \equiv \delta(n_1 + n_2 + n \text{ even}) \delta(|n_1 - n_2| \leq n \leq n_1 + n_2) \frac{\sqrt{n_1! n_2! n!}}{\left(\frac{n_1 - n_2 + n}{2}\right)! \left(\frac{n_2 - n_1 + n}{2}\right)! \left(\frac{n_1 + n_2 - n}{2}\right)!} , \quad (\text{C.3})$$

and

$$T_{m_1 n_1 m_2 n_2}^{(2)n} \equiv (-1)^{n+n_1+n_2} \delta(|X_1 - X_2| \leq X \leq X_1 + X_2) \times \sum_{l=\delta_{\text{inf}}, 2}^{\delta_{\text{sup}}} N(X, X_1, X_2, m, m_1 + l) N(X_1, X_2, X, m_1, l) N(X_2, X, X_1, m_2, m_2 + l) , \quad (\text{C.4})$$

were

$$X_1 \equiv 2n_1 + |m_1| , \quad (\text{C.5})$$

$$X_2 \equiv 2n_2 + |m_2| , \quad (\text{C.6})$$

$$m \equiv m_2 - m_1 , \quad (\text{C.7})$$

$$X \equiv 2n + |m| , \quad (\text{C.8})$$

$$X_a \equiv \frac{1}{2}(X + X_1 - X_2) , \quad (\text{C.9})$$

$$X_b \equiv \frac{1}{2}(X + X_2 - X_1) , \quad (\text{C.10})$$

$$X_c \equiv \frac{1}{2}(X_1 + X_2 - X) , \quad (\text{C.11})$$

$$\delta_{\text{sup}} \equiv \min\{X_a - m_1, X_b - m_2, X_c\} , \quad (\text{C.12})$$

$$\delta_{\text{inf}} \equiv \max \left\{ -X_a - m_1, -X_b - m_2, -X_c \right\} , \quad (\text{C.13})$$

and

$$N(X_a, X_b, X_c, m_a, m_e) \equiv \frac{\sqrt{\left(\frac{X_a - m_a}{2}\right)! \left(\frac{X_a + m_a}{2}\right)!}}{\left(\frac{X_a + X_b - X_c - 2m_e}{4}\right)! \left(\frac{X_a + X_b - X_c + 2m_e}{4}\right)!} . \quad (\text{C.14})$$

C.1.1 Integral relations

Defining

$$I(n_1, n_2; b, B) \equiv \int_{-\infty}^{\infty} dz e^{-z^2/(2b^2) - z^2/(2B^2)} \psi_{n_1}^{(1)}(z; b) \psi_{n_2}^{(1)}(z; B) , \quad (\text{C.15a})$$

$$I(n_1, n_2, n; b, B) \equiv \int dz \psi_{n_1}^{(1)}(z; b) \psi_{n_2}^{(1)}(z; b) \psi_n^{(1)}(z; B) e^{-\frac{z^2}{2B^2}} , \quad (\text{C.15b})$$

$$I(m_1, n_1; m_2, n_2; b, B) \equiv \int_0^{\infty} r dr \int_0^{2\pi} d\varphi e^{-r^2/(2b^2) - r^2/(2B^2)} \psi_{m_1 n_1}^{(2)}(r, \varphi; b) \psi_{m_2 n_2}^{(2)}(r, \varphi; B) , \quad (\text{C.15c})$$

it is shown in Ref. [79] that

$$I(n_1, n_2; b, B) = \delta_{n_1 + n_2 \text{ even}} \frac{\left(\frac{B}{b}\right)^{(n_2 - n_1)/2}}{\left(\frac{b}{B} + \frac{B}{b}\right)^{\frac{n_1 + n_2 + 1}{2}}} \sqrt{\frac{n_1! n_2!}{2^{n_1 + n_2}}} \frac{(-1)^{(n_1 - n_2)/2}}{\left(\frac{n_1 + n_2}{2}\right)!} \binom{n_1 + n_2}{n_2} , \quad (\text{C.16a})$$

$$I(n_1, n_2, n; b, B) = \delta_{n_1 + n_2 + n \text{ even}} \frac{\left(\frac{B}{b}\right)^{n+1}}{\sqrt{2B\pi^{7/2}}} \frac{\Gamma(\xi - n_1) \Gamma(\xi - n_2) \Gamma(\xi - n)}{z^\xi \sqrt{n_1! n_2! n!}} {}_2F_1(-n_1, -n_2; -\xi + n + 1; 1 - z) , \quad (\text{C.16b})$$

$$I(m_1, n_1; m_2, n_2; b, B) = \delta_{m_1, -m_2} \frac{\left(\frac{B}{b}\right)^{n_2 - n_1}}{\left(\frac{B}{b} + \frac{b}{B}\right)^{n_1 + n_2 + |m_1| + 1}} \sqrt{n_1! (n_1 + |m_1|)! n_2! (n_2 + |m_1|)!} \Xi(n_1, n_2, |m_1|) , \quad (\text{C.16c})$$

with

$$\xi \equiv \frac{n_1 + n_2 + n + 1}{2} , \quad (\text{C.17a})$$

$$z \equiv \frac{1}{2} \left(1 + \frac{B^2}{b^2}\right) , \quad (\text{C.17b})$$

$$\Xi(n_1, n_2, |m|) \equiv \frac{1}{(n_1 + n_2 + |m|)!} \binom{n_1 + n_2 + |m|}{n_1} \binom{n_1 + n_2 + |m|}{n_2} . \quad (\text{C.17c})$$

Appendix D

Moshinsky coefficients

From Ref. [80] it is shown that Moshinsky coefficients (3.16) are expressed as

$$\mathcal{M}^{(1,2)0\beta}_{\mu\nu} = (-1)^{X_\nu^{(1,2)}} \left(\frac{1}{\sqrt{2}} \right)^{X_\beta^{(1,2)}} C^{(1,2)\beta}_{\mu\nu} , \quad (\text{D.1})$$

where

$$X_a^{(1)} \equiv n_{z_a} , \quad (\text{D.2a})$$

$$X_a^{(2)} \equiv 2n_a + |m_a| , \quad (\text{D.2b})$$

$$C^{(1)\beta}_{\mu\nu} \equiv \sqrt{\frac{n_{z_\beta}!}{n_{z_\mu}!n_{z_\nu}!}} \delta_{n_{z_\beta} \ n_{z_\mu}+n_{z_\nu}} , \quad (\text{D.2c})$$

$$C^{(2)\beta}_{\mu\nu} \equiv (-1)^{n_\mu+n_\nu+n_\beta} \sqrt{\frac{n_\beta!(n_\beta+|m_\beta|)!}{n_\mu!(n_\mu+|m_\mu|)!n_\nu!(n_\nu+|m_\nu|)!}} \delta_{m_\beta \ m_\mu+m_\nu} \delta_{X_\beta^{(2)} \ X_\mu^{(2)}+X_\nu^{(2)}} . \quad (\text{D.2d})$$

One define then reduced Moshinsky coefficients as

$$\mathcal{M}_{1 \text{ red}}(n_1, n_2) \equiv \mathcal{M}_{n_1 \ n_2}^{0 \ n_1+n_2} \quad (\text{D.3a})$$

$$\mathcal{M}_{2 \text{ red}}(m_1)(n_1, n_2) \equiv \mathcal{M}_{(m_1, n_1) \ (-m_1, n_2)}^{(0,0) \ (0, n_1+n_2+|m_1|)} \quad (\text{D.3b})$$

Appendix E

Spherical change of coordinates

Let (u_x, u_y, u_z) be the coordinates of a vector in a cartesian frame. Let us introduce the change of coordinates

$$u^+ \equiv -\frac{1}{\sqrt{2}}(u_x + iu_y) , \quad (\text{E.1a})$$

$$u^- \equiv \frac{1}{\sqrt{2}}(u_x - iu_y) , \quad (\text{E.1b})$$

$$u^3 \equiv u_z . \quad (\text{E.1c})$$

The scalar product is expressed in term of this new coordinate system as

$$\vec{A} \cdot \vec{B} = -A^- B^+ - A^+ B^- + A^3 B^3 , \quad (\text{E.2})$$

the vector product is written as

$$(\vec{A} \times \vec{B})^+ = i[A^3 B^+ - A^+ B^3] , \quad (\text{E.3a})$$

$$(\vec{A} \times \vec{B})^- = i[A^- B^3 - A^3 B^-] , \quad (\text{E.3b})$$

$$(\vec{A} \times \vec{B})^3 = i[A^- B^+ - A^+ B^-] . \quad (\text{E.3c})$$

And the Pauli matrices transforms as

$$\sigma^+ = -\sqrt{2} \begin{pmatrix} 0 & 1 \\ 0 & 0 \end{pmatrix} \equiv -\sqrt{2} E^{+-} , \quad (\text{E.4a})$$

$$\sigma^- = \sqrt{2} \begin{pmatrix} 0 & 0 \\ 1 & 0 \end{pmatrix} \equiv \sqrt{2} E^{-+} , \quad (\text{E.4b})$$

$$\sigma^3 = \begin{pmatrix} 1 & 0 \\ 0 & -1 \end{pmatrix} \equiv (E^{++} - E^{--}) . \quad (\text{E.4c})$$

Appendix F

Recurrence relations for basis functions

In this appendix, recurrence relations for a cylindrical harmonic oscillator basis are reviewed, proofs are omitted, but can (with some work) be recovered by the reader.

F.1 Recurrence relations for Hermite and Laguerre polynomials

The Hermite polynomials obey recurrence relation

Theorem F.1.1. *for all $n \in \mathbb{N}$*

(i)

$$\frac{d}{dx}H_n = 2nH_{n-1} \text{ ,}$$

(ii)

$$n\frac{d}{dx}H_{n-1}(x) = x\frac{d}{dx}H_n(x) - nH_n(x) \text{ ,}$$

(iii)

$$2xH_n(x) = H_{n+1}(x) + 2nH_{n-1}(x) \text{ .}$$

with the convention $H_{-1} \equiv 0$.

and for generalized Laguerre polynomials

Theorem F.1.2. *for all $\alpha \in \mathbb{C}$, and $n \in \mathbb{N}$*

(i)

$$L_{n-1}^{\alpha+1} + L_n^\alpha = L_n^{\alpha+1} \text{ ,}$$

(ii)

$$(n+1)L_{n+1}^\alpha(x) = (2n + \alpha + 1 - x)L_n^\alpha(x) - (n + \alpha)L_{n-1}^\alpha(x) \text{ ,}$$

(iii)

$$\frac{d}{dx}L_n^\alpha(x) = -L_{n-1}^{\alpha+1} \text{ .}$$

with the convention $L_{-1}^\alpha \equiv 0$.

Moreover

Theorem F.1.3. *for all $n \in \mathbb{N}$*

$$nL_n^{-1}(x) = -xL_{n-1}^1(x) \text{ .} \tag{F.1}$$

These three propositions can be used to show recurrence relations for a cylindrical harmonic oscillator basis.

F.2 Axial part

Theorem F.2.1. *for every $n \geq 0$*

$$\frac{z}{b_z} \psi_n^{(1)}(z; b_z) = \sqrt{\frac{n+1}{2}} \psi_{n+1}^{(1)}(z; b_z) + \sqrt{\frac{n}{2}} \psi_{n-1}^{(1)}(z; b_z) , \quad (\text{F.2})$$

Theorem F.2.2. *for every $n \geq 0$*

$$\psi_{n+1}^{(1)}(z; b_z) = \sqrt{\frac{2}{n+1}} \frac{z}{b_z} \psi_n^{(1)}(z; b_z) - \sqrt{\frac{n}{n+1}} \psi_{n-1}^{(1)}(z; b_z) , \quad (\text{F.3})$$

Theorem F.2.3. *for every $n \geq 0$*

$$\frac{d}{dz} \psi_n^{(1)}(z; b_z) = \frac{1}{b_z \sqrt{2}} \left(\sqrt{n} \psi_{n-1}^{(1)}(z; b_z) - \sqrt{n+1} \psi_{n+1}^{(1)}(z; b_z) \right) , \quad (\text{F.4})$$

F.3 Perpendicular part

Definition F.3.1. *for $n \geq 1$, defining*

$$\chi_n^{-1}(r; b_r) \equiv -\chi_{n-1}^1(r; b_r) , \quad (\text{F.5})$$

and

$$\eta \equiv \frac{r^2}{b_r^2} . \quad (\text{F.6})$$

One has

Theorem F.3.1. *for all $m \geq 0$ and $n \geq 0$*

$$\sqrt{\eta} \chi_n^m(r; b_r) = \sqrt{n+m+1} \chi_n^{m+1}(r; b_r) - \sqrt{n} \chi_{n-1}^{m+1}(r; b_r) , \quad (\text{F.7})$$

Theorem F.3.2. *for every $m \geq 0$ and $n \geq 0$*

$$\sqrt{\eta} \chi_n^m(\eta) = \sqrt{n+m} \chi_n^{m-1}(\eta) - \sqrt{n+1} \chi_{n+1}^{m-1}(\eta) , \quad (\text{F.8})$$

Theorem F.3.3. *for every $m \geq 0$ and $n \geq 0$*

$$\frac{m}{\sqrt{\eta}} \chi_n^m(\eta) = \sqrt{n+m} \chi_n^{m-1}(\eta) + \sqrt{n} \chi_{n-1}^{m+1}(\eta) \quad (\text{F.9})$$

$$= \sqrt{n+m+1} \chi_n^{m+1}(\eta) + \sqrt{n+1} \chi_{n+1}^{m-1}(\eta) . \quad (\text{F.10})$$

Theorem F.3.4. *for every $m \geq 0$ and $n \geq 0$*

$$\begin{aligned} 2\sqrt{\eta} \frac{d}{d\eta} \chi_n^m &= \sqrt{n+1} \chi_{n+1}^{m-1} - \sqrt{n} \chi_{n-1}^{m+1} \\ &= \sqrt{n+m} \chi_n^{m-1} - \sqrt{n+m+1} \chi_n^{m+1} . \end{aligned}$$

Theorem F.3.5. *For all $m \in \mathbb{Z}$ and $n \in \mathbb{N}$*

$$\nabla^- \psi_{m \ n}^{(2)} = \frac{(-1)^{\delta(m \leq 0)}}{\sqrt{2} b_r} \left[\sqrt{n + \delta(m \geq 1)} \psi_{m-1 \ n+(-1)^{\delta(m \leq 0)}}^{(2)} + \sqrt{n + |m| + \delta(m \leq 0)} \psi_{m-1 \ n}^{(2)} \right] \quad (\text{F.11})$$

$$\nabla^+ \psi_{m \ n}^{(2)} = \frac{(-1)^{\delta(m \leq -1)}}{\sqrt{2} b_r} \left[\sqrt{n + \delta(m \leq -1)} \psi_{m+1 \ n+(-1)^{\delta(m \geq 0)}}^{(2)} + \sqrt{n + |m| + \delta(m \geq 0)} \psi_{m+1 \ n}^{(2)} \right] \quad (\text{F.12})$$

Appendix G

Gogny matrix elements and fields

In this Appendix, details are given to complement expressions introduced in Chap. 3. Particular attention is given to the derivation of HFB fields and their optimization.

G.1 Central term

Integrals

$$V_{\alpha\beta\gamma\delta}^{C_1} = \int dz_1 dz_2 \psi_{\alpha}^{(1)}(z_1; b_z) \psi_{\beta}^{(1)}(z_2; b_z) e^{-(z_1-z_2)^2/\mu^2} \psi_{\gamma}^{(1)}(z_1; b_z) \psi_{\delta}^{(1)}(z_2; b_z) , \quad (\text{G.1a})$$

$$V_{\alpha\beta\gamma\delta}^{C_2} = \int d^2\vec{r}_1 d^2\vec{r}_2 \psi_{\alpha}^{(2)*}(\vec{r}_1; b_r) \psi_{\beta}^{(2)*}(\vec{r}_2; b_r) e^{-(\vec{r}_1-\vec{r}_2)^2/\mu^2} \psi_{\gamma}^{(2)}(\vec{r}_1; b_r) \psi_{\delta}^{(2)}(\vec{r}_2; b_r) . \quad (\text{G.1b})$$

Are explicitied into

$$V_{\alpha\beta\gamma\delta}^{C_1} = \delta(n_{z\alpha} + n_{z\beta} + n_{z\gamma} + n_{z\delta} \text{ even}) \frac{\mu}{\sqrt{2\pi^3} b_z} \sum_{n_z=|n_{z\beta}-n_{z\delta}|, 2}^{n_{z\beta}+n_{z\delta}} T_{n_{z\beta}n_{z\delta}}^{(1)n_z} \bar{F}_{n_{z\alpha}n_{z\gamma}}^{n_z} , \quad (\text{G.2})$$

and

$$V_{\alpha\beta\gamma\delta}^{C_2} = \delta_{m_{\alpha}+m_{\beta}, m_{\gamma}+m_{\delta}} \frac{G_r - 1}{G_r + 1} \sum_{n_1=0}^{n_{\beta,\delta}} \sum_{n_2=0}^{n_{\alpha,\gamma}} T_{n_{\alpha}, m_{\alpha}; n_{\gamma}, m_{\gamma}}^{(2)n_2} T_{n_{\beta}, m_{\beta}; n_{\delta}, m_{\delta}}^{(2)n_1} \bar{I}(m_{\alpha} - m_{\gamma}, n_1, n_2) , \quad (\text{G.3})$$

where

$$G_z \equiv 1 + \frac{\mu^2}{b_z^2}, \quad (\text{G.4a})$$

$$G_r \equiv 1 + \frac{\mu^2}{b_r^2}, \quad (\text{G.4b})$$

and

$$\bar{I}(m_{\alpha} - m_{\gamma}, n_1, n_2) \equiv \frac{\sqrt{n_1!(n_1 + |m_{\alpha} - m_{\gamma}|)! n_2!(n_2 + |m_{\alpha} - m_{\gamma}|)!}}{(G_r + 1)^{n_1+n_2+|m_{\alpha}-m_{\gamma}|}} \Xi(n_1, n_2, |m_{\alpha} - m_{\gamma}|) , \quad (\text{G.5})$$

with Ξ given by Eq. (C.17c). The coefficient $\bar{F}_{n_{z\alpha}, n_{z\gamma}}^{n_z}$ is expressed in terms of the Gauss hypergeometric function. Referring to Ref. [91] §4 for the definition of ${}_2F_1$ and Refs. [79, 92] for the proof of Eq. (G.6).

$$\begin{aligned} \bar{F}_{n_{z\alpha}, n_{z\gamma}}^{n_z} &\equiv \delta(n_{z\alpha} + n_{z\gamma} + n_z \text{ even}) \frac{\Gamma(\xi - n_{z\alpha})\Gamma(\xi - n_{z\gamma})\Gamma(\xi - n_z)}{z^\xi \sqrt{n_z! n_{z\alpha}! n_{z\gamma}!}} \\ &\times {}_2F_1(-n_{z\alpha}, -n_{z\gamma}; -\xi + n_z + 1; 1 - z) \ , \end{aligned} \quad (\text{G.6})$$

where

$$\xi \equiv \frac{n_{z\alpha} + n_{z\gamma} + n_z + 1}{2} \ , \quad (\text{G.7a})$$

$$z \equiv 1 + \frac{\mu^2}{2b_z^2} = \frac{1}{2} (G_z + 1) \ . \quad (\text{G.7b})$$

Expressions for V^{C_1} have been shown to be very stable numerically [79], however calculation of V^{C_2} starts breaking down around 20 oscillator shells with double precision. Going to larger bases would either require using quadruple precision or re-express Eq. (G.3) using hypergeometric functions as for V^{C_1} . This is left for a later study.

Numerical implementation of central fields

Once central matrix elements are precomputed, and given off-diagonal one-body density matrices $\rho^{qq'\theta\mu}$ and $\kappa^{qq'\theta\mu}$ (see Eqs. (1.27), (1.31) and (1.32)), off-diagonal one-body fields

$$h_{\alpha\gamma}^{Cqq'\theta\mu} = \frac{1}{2} \sum_{s_\beta s_\delta t_\beta} \left(\sum_{m_\beta m_\delta} \left(\sum_{n_\beta n_\delta} \left(\sum_{n_z \beta n_z \delta} \left(V_{\alpha\beta\gamma\delta}^{C\mu} - V_{\alpha\beta\delta\gamma}^{C\mu} \right) \rho_{\delta\beta}^{qq'\theta\mu} \right) \right) \right) \ , \quad (\text{G.8a})$$

$$\Delta_{\alpha\gamma}^{Cqq'\theta\mu} = \frac{1}{2} \sum_{s_\beta s_\delta t_\beta} \left(\sum_{m_\beta m_\delta} \left(\sum_{n_\beta n_\delta} \left(\sum_{n_z \beta n_z \delta} V_{\alpha\gamma\beta\delta}^{C\mu} \kappa_{\beta\delta}^{qq'\theta\mu} \right) \right) \right) \ , \quad (\text{G.8b})$$

can be computed. in Eqs. (G.8a) and (G.8b) the parenthesis indicates the chosen summation order in the numerical implementation (see Ref. [93]) to reduce computational complexity.

G.2 Coulomb term

Coulomb matrix elements are factorised in a spatial part and spin-isospin part

$$V_{\alpha\beta\gamma\delta}^{\text{Coul}} \equiv V_{\alpha\beta\gamma\delta}^{\text{Coul}_r} V_{\alpha\beta\gamma\delta}^{\text{Coul}_{st}} \ , \quad (\text{G.9})$$

with

$$V_{\alpha\beta\gamma\delta}^{\text{Coul}_{st}} \equiv \delta_{s_\alpha s_\gamma} \delta_{s_\beta s_\delta} \delta(t_\alpha = t_\beta = t_\gamma = t_\delta = \text{proton}) \ , \quad (\text{G.10})$$

and

$$V_{\alpha\beta\gamma\delta}^{\text{Coul}_r} \equiv q_{\text{proton}}^2 \int d^3\mathbf{r}_1 d^3\mathbf{r}_2 \psi_\alpha^*(\mathbf{r}_1) \psi_\beta^*(\mathbf{r}_2) \frac{1}{|\mathbf{r}_1 - \mathbf{r}_2|} \psi_\gamma(\mathbf{r}_1) \psi_\delta(\mathbf{r}_2) \ . \quad (\text{G.11})$$

As shown in Ref. [80]

$$V_{\alpha\beta\gamma\delta}^{\text{Coul}_r} = \frac{q_{\text{proton}}^2 \sqrt{2}}{\pi^{1/4}} \sum_{n_\mu=0}^{n_{\alpha\gamma}} \sum_{n_\nu=0}^{n_{\beta\delta}} \sum_{n_{z\mu}=|n_{z\alpha}-n_{z\gamma}|, 2}^{n_{z\alpha}+n_{z\gamma}} \sum_{n_{z\nu}=|n_{z\beta}-n_{z\delta}|, 2}^{n_{z\beta}+n_{z\delta}}$$

$$\begin{aligned} & \times T^{(1)n_{z\nu}}_{n_{z\beta}n_{z\delta}} T^{(1)n_{z\mu}}_{n_{z\alpha}n_{z\gamma}} T^{(2)n_\nu}_{m_\beta n_\beta m_\delta n_\delta} T^{(2)n_\mu}_{m_\alpha n_\alpha m_\gamma n_\gamma} \mathcal{M}_{n_{z\mu} n_{z\nu}}^{(1)\text{red}} \mathcal{M}_{m_\gamma - m_\alpha n_\mu n_\nu}^{(2)\text{red}} \\ & \times I_{\text{coul}}(n_\mu + n_\nu + |m_\gamma - m_\alpha|, n_{z\mu} + n_{z\nu}) , \end{aligned} \quad (\text{G.12})$$

with

$$I_{\text{coul}}(n, n_z) \equiv \psi_{n_z}^{(1)}(0; 1) \frac{1}{b_z} \left(\frac{b_r}{b_z} \right)^{2n} \int_0^1 \frac{x^{2n+n_z}}{(1+\gamma x^2)^{n+1}} dx , \quad (\text{G.13})$$

and

$$\gamma \equiv \left(\frac{b_r}{b_z} \right)^2 - 1 . \quad (\text{G.14})$$

Numerical implementation of Coulomb fields

Defining

$$f_{m_\alpha m_\gamma}^{n_\mu n_\nu} = \frac{q_{\text{proton}}^2}{\pi^{1/4} \sqrt{2}} \frac{1}{b_z} \left(\frac{b_r}{b_z} \right)^{2(n_\mu + n_\nu + |m_\alpha - m_\gamma|)} , \quad (\text{G.15})$$

and breaking Coulomb field in direct and exchange part

$$h_{\alpha\gamma}^{\text{coul } qq'\theta\mu} = h_{\alpha\gamma}^{\text{coul di } qq'\theta\mu} - h_{\alpha\gamma}^{\text{coul ex } qq'\theta\mu} , \quad (\text{G.16})$$

one has

$$\begin{aligned} h_{\alpha\gamma}^{\text{coul di } qq'\theta\mu} &= \sum_{n_{z\mu} n_\mu} T^{(1)n_{z\mu}}_{n_{z\alpha} n_{z\gamma}} T^{(2)n_\mu}_{m_\alpha n_\alpha m_\gamma n_\gamma} \sum_{m_\beta m_\delta} \delta(m_\delta + m_\gamma = m_\alpha + m_\beta) \\ & \sum_{s_\beta s_\delta} \delta(s_\beta = s_\delta) \int_0^1 dx \sum_{n_{z\nu} n_{z\beta} n_{z\delta} n_\beta n_\delta n_\nu} \rho_{\delta\beta}^{qq'\theta\mu}(\text{proton}, s_\delta, s_\beta) \\ & \times f_{m_\alpha m_\gamma}^{n_\mu n_\nu} \psi_{n_{z\mu} + n_{z\nu}}^{(1)}(0; 1) \mathcal{M}_{n_{z\mu} n_{z\nu}}^{(1)\text{red}} \mathcal{M}_{|m_\gamma - m_\alpha| n_\mu n_\nu}^{(2)} \frac{x^{2(n_\mu + n_\nu + |m_\gamma - m_\alpha| + n_{z\mu} + n_{z\nu})}}{(1+\gamma x^2)^{n_\mu + n_\nu + |m_\gamma - m_\alpha|}} T^{(1)n_{z\nu}}_{n_{z\beta} n_{z\delta}} T^{(2)n_\nu}_{m_\beta n_\beta m_\delta n_\delta} \end{aligned} \quad (\text{G.17a})$$

$$\begin{aligned} h_{\alpha\gamma}^{\text{coul ex } qq'\theta\mu} &= \sum_{s_\beta s_\delta} \sum_{m_\beta m_\delta} \delta(m_\delta + m_\gamma = m_\alpha + m_\beta) \\ & \int_0^1 dx \sum_{n_\beta n_\delta} \sum_{n_{z\beta} n_{z\delta}} \left(\sum_{n_{z\mu} n_{z\nu}} \psi_{n_{z\mu} + n_{z\nu}}^{(1)}(0; 1) T^{(1)n_{z\mu}}_{n_{z\alpha} n_{z\delta}} T^{(1)n_{z\nu}}_{n_{z\beta} n_\gamma} \mathcal{M}_{n_{z\mu} n_{z\nu}}^{(1)\text{red}} x^{n_{z\mu} + n_{z\nu}} \right) \\ & \times \left(\sum_{n_\mu n_\nu} f_{m_\alpha m_\delta}^{n_\mu n_\nu} T^{(2)n_\mu}_{m_\alpha n_\alpha m_\delta n_\delta} T^{(2)n_\nu}_{m_\beta n_\beta m_\gamma n_\gamma} \mathcal{M}_{|m_\alpha - m_\delta| n_\mu n_\nu}^{(2)\text{red}} \frac{x^{2(n_\mu + n_\nu + |m_\alpha - m_\delta|)}}{(1+\gamma x^2)^{n_\mu + n_\nu + |m_\alpha - m_\delta| + 1}} \right) \\ & \times \rho_{\delta\beta}^{qq'\theta\mu}(\text{proton}, s_\delta, s_\beta) \end{aligned} \quad (\text{G.18a})$$

$$\begin{aligned} \Delta_{\alpha\gamma}^{\text{coul } qq'\theta\mu} &= \sum_{s_\beta s_\delta} \sum_{m_\beta m_\delta} \delta(m_\delta + m_\beta = m_\alpha + m_\gamma) \int_0^1 dx \sum_{n_\beta n_\delta} \sum_{n_{z\beta} n_{z\delta}} \\ & \left(\sum_{n_{z\mu} n_{z\nu}} \frac{1}{b_z} \psi_{n_{z\mu} + n_{z\nu}}^{(1)}(0; 1) T^{(1)n_{z\mu}}_{n_{z\alpha} n_{z\beta}} T^{(1)n_{z\nu}}_{n_{z\gamma} n_{z\delta}} \mathcal{M}_{n_{z\mu} n_{z\nu}}^{(1)\text{red}} x^{n_{z\mu} + n_{z\nu}} \right) \end{aligned}$$

$$\begin{aligned}
& \times \left(\sum_{n_\mu n_\nu} \left(\frac{b_r^2}{b_z^2} \right)^{n_\mu + n_\nu + |m_\alpha - m_\beta|} T_{m_\alpha n_\alpha m_\beta n_\beta}^{(2)n_\mu} T_{m_\gamma n_\gamma m_\delta n_\delta}^{(2)n_\nu} \mathcal{M}_{|m_\alpha - m_\beta| n_\mu n_\nu}^{(2)\text{red}} \frac{x^{2(n_\mu + n_\nu + |m_\alpha - m_\beta|)}}{(1 + \gamma x^2)^{n_\mu + n_\nu + |m_\alpha - m_\beta| + 1}} \right) \\
& \times \kappa_{\gamma\delta}^{qq'\theta\mu}(\text{proton}, s_\gamma, s_\delta) \tag{G.19a}
\end{aligned}$$

The interversion between the integral and the summation on n and n_z quantum numbers in the calculation of the fields is instrumental to exploit the separability of the interaction, significantly reducing the numerical complexity.

G.3 Center of mass term

Using Eq. (E.2), the spatial part can be written

$$\begin{aligned}
\langle \psi_\alpha \psi_\beta | \mathbf{p}_1 \cdot \mathbf{p}_2 | \psi_\gamma \psi_\delta \rangle &= \langle \psi_\alpha \psi_\beta | -p_1^+ p_2^- - p_1^- p_2^+ + p_1^3 p_2^3 | \psi_\gamma \psi_\delta \rangle \\
&= -\langle \psi_\alpha | p_1^+ | \psi_\gamma \rangle \langle \psi_\beta | p_2^- | \psi_\delta \rangle \\
&\quad - \langle \psi_\alpha | p_1^- | \psi_\gamma \rangle \langle \psi_\beta | p_2^+ | \psi_\delta \rangle \\
&\quad + \langle \psi_\alpha | p_1^3 | \psi_\gamma \rangle \langle \psi_\beta | p_2^3 | \psi_\delta \rangle . \tag{G.20}
\end{aligned}$$

Defining

$$C_{\alpha\beta}^+ \equiv \langle \psi_\alpha | \nabla^+ | \psi_\beta \rangle = \int d^3\mathbf{r} \psi_\alpha^*(\mathbf{r}) \nabla^+ \psi_\beta(\mathbf{r}) , \tag{G.21a}$$

$$C_{\alpha\beta}^- \equiv \langle \psi_\alpha | \nabla^- | \psi_\beta \rangle = \int d^3\mathbf{r} \psi_\alpha^*(\mathbf{r}) \nabla^- \psi_\beta(\mathbf{r}) , \tag{G.21b}$$

$$C_{\alpha\beta}^3 \equiv \langle \psi_\alpha | \nabla^3 | \psi_\beta \rangle = \int d^3\mathbf{r} \psi_\alpha^*(\mathbf{r}) \nabla^3 \psi_\beta(\mathbf{r}) , \tag{G.21c}$$

using Thm. (F.3.5), Eqs (G.21) are simplified into

$$C_{\alpha\beta}^+ = \delta_{n_{z\alpha} n_{z\beta}} \delta_{m_\alpha, m_\beta + 1} \frac{(-1)^{\delta(m_\beta \leq -1)}}{b_r \sqrt{2}} \left[\sqrt{n_\beta + \delta(m_\beta \leq -1)} \delta_{n_\alpha, n_\beta + (-1)^{\delta(m_\beta \geq 0)}} + \sqrt{n_\beta + |m_\beta| + \delta(m_\beta \geq 0)} \delta_{n_\alpha, n_\beta} \right] , \tag{G.22}$$

$$C_{\alpha\beta}^- = \delta_{n_{z\alpha} n_{z\beta}} \delta_{m_\alpha, m_\beta - 1} \frac{(-1)^{\delta(m_\beta \leq 0)}}{b_r \sqrt{2}} \left[\sqrt{n_\beta + \delta(m_\beta \geq 1)} \delta_{n_\alpha, n_\beta + (-1)^{\delta(m_\beta \leq 0)}} + \sqrt{n_\beta + |m_\beta| + \delta(m_\beta \leq 0)} \delta_{n_\alpha, n_\beta} \right] , \tag{G.23}$$

$$C_{\alpha\beta}^3 = \delta_{m_\alpha m_\beta} \delta_{n_\alpha n_\beta} \frac{1}{b_z \sqrt{2}} \left[\sqrt{n_{z\beta}} \delta_{n_{z\alpha}, n_{z\beta} - 1} - \sqrt{n_{z\beta} + 1} \delta_{n_{z\alpha}, n_{z\beta} + 1} \right] . \tag{G.24}$$

Finally

$$\langle \psi_\alpha \psi_\beta | \mathbf{p}_1 \cdot \mathbf{p}_2 | \psi_\gamma \psi_\delta \rangle = -\hbar^2 \left(-C_{\alpha\gamma}^+ C_{\beta\delta}^- - C_{\alpha\gamma}^- C_{\beta\delta}^+ + C_{\alpha\gamma}^3 C_{\beta\delta}^3 \right) . \tag{G.25}$$

Numerical implementation of 2-body COM correction fields

In the numerical code, matrices C^+ , C^- and C^3 are precomputed, and the fields are implemented according to

$$h_{\alpha\gamma}^{\text{com2 } qq'\theta\mu} = \frac{\hbar^2}{2m\langle A \rangle} \delta_{t_\alpha t_\gamma}$$

$$\begin{aligned} & \times \left[\delta_{s_\alpha s_\gamma} \sum_{s_\beta t_\beta} \left\{ -C_{\alpha\gamma}^+ \text{Tr} \left(C^- \rho^{qq'\theta\mu}(t_\beta, s_\beta, s_\beta) \right) - C_{\alpha\gamma}^- \text{Tr} \left(C^+ \rho^{qq'\theta\mu}(t_\beta, s_\beta, s_\beta) \right) + C_{\alpha\gamma}^3 \text{Tr} \left(C^3 \rho^{qq'\theta\mu}(t_\beta, s_\beta, s_\beta) \right) \right\} \right. \\ & \left. + \left(C^+ \rho^{qq'\theta\mu}(t_\alpha, s_\alpha, s_\gamma) C^- \right)_{\alpha\gamma} + \left(C^- \rho^{qq'\theta\mu}(t_\alpha, s_\alpha, s_\gamma) C^+ \right)_{\alpha\gamma} - \left(C^3 \rho^{qq'\theta\mu}(t_\alpha, s_\alpha, s_\gamma) C^3 \right)_{\alpha\gamma} \right] \end{aligned} \quad (\text{G.26a})$$

$$\begin{aligned} \Delta_{\alpha\gamma}^{\text{com2 } qq'\theta\mu} &= \frac{\hbar^2}{2m\langle A \rangle} \delta_{t_\alpha t_\gamma} \\ & \times \left[\left(C^+ \kappa^{qq'\theta\mu}(t_\alpha, s_\alpha, s_\gamma) (C^-)^T \right)_{\alpha\gamma} + \left(C^- \kappa^{qq'\theta\mu}(t_\alpha, s_\alpha, s_\gamma) (C^+)^T \right)_{\alpha\gamma} - \left(C^3 \kappa^{qq'\theta\mu}(t_\alpha, s_\alpha, s_\gamma) (C^3)^T \right)_{\alpha\gamma} \right] \end{aligned} \quad (\text{G.26b})$$

G.4 Density term

G.4.1 Density field

Introducing following intermediary quantity

$$\tilde{\rho}(r, z, \varphi)(m, s_\alpha, s_\gamma, t_\alpha) \equiv \sum_{m_\beta n_\beta n_{z\beta}} \sum_{m_\delta n_\delta n_{z\delta}} e^{i(m+m_\delta-m_\beta)\varphi} \tilde{\psi}_\delta \tilde{\psi}_\beta \left(\sum_{s_\beta s_\delta t_\beta} V_{\alpha\beta\gamma\delta}^{D_{st}} \rho_{\beta\delta} \right), \quad (\text{G.27})$$

where parenthesis indicates chosen summation order, recalling $\tilde{\psi}$ is defined with (3.5c), and $V_{\alpha\beta\gamma\delta}^{D_{st}}$ is given by (3.42). Then density field can be expressed as

$$h_{\alpha\gamma}^D = \delta_{t_\alpha t_\gamma} \int r dr \int dz \tilde{\psi}_\alpha \tilde{\psi}_\gamma \left(\int d\varphi \rho^{\alpha_G}(r, z, \varphi) \tilde{\rho}(r, z, \varphi)(m_\gamma - m_\alpha, s_\alpha, s_\gamma, t_\alpha) \right). \quad (\text{G.28})$$

In practice, constructing an intermediate resulting from a sole integration on φ allows to significantly reduce the computational cost of this calculation.

G.4.2 Rearrangment field

The rearrangment field initially expressed as

$$h_{\mu\nu}^{DR} = \frac{1}{2} \sum_{\alpha\beta\gamma\delta} \frac{\delta \bar{v}_{\alpha\beta\gamma\delta}(\rho)}{\delta \rho_{\nu\mu}} \rho_{\delta\beta} \rho_{\gamma\alpha}, \quad (\text{G.29})$$

is transformed into

$$h_{\mu\nu}^{DR} = \frac{1}{2} \delta_{s_\mu s_\nu} \delta_{t_\mu t_\nu} \sum_{\alpha\beta\gamma\delta} \int d^3\mathbf{r} (\alpha_G \rho^{\alpha_G-1}) \psi_\nu(\mathbf{r}) \psi_\mu^*(\mathbf{r}) V_{\alpha\beta\gamma\delta}^{D_{st}} \psi_\alpha^*(\mathbf{r}) \psi_\beta^*(\mathbf{r}) \psi_\gamma(\mathbf{r}) \psi_\delta(\mathbf{r}) \rho_{\delta\beta} \rho_{\gamma\alpha}. \quad (\text{G.30})$$

In order to compute the field, intermediary quantity

$$\tilde{\rho}(r, z, \varphi)(m, s_\alpha, s_\gamma, t_\alpha) \equiv \sum_{m_\alpha n_\alpha n_{z\alpha}} \sum_{m_\gamma n_\gamma n_{z\gamma}} \tilde{\psi}_\alpha \tilde{\psi}_\gamma \rho_{\gamma\alpha} \tilde{\rho}(r, z, \varphi)(m - m_\alpha + m_\gamma, s_\alpha, s_\gamma, t_\alpha), \quad (\text{G.31})$$

is precomputed, then rearrangment field becomes

$$h_{\mu\nu}^{DR} = \delta_{t_\alpha t_\gamma} \int r dr \int dz \tilde{\psi}_\nu \tilde{\psi}_\mu \left(\int d\varphi (\alpha_G \rho^{\alpha_G-1}(r, z, \varphi)) \tilde{\rho}(r, z, \varphi)(m_\nu - m_\mu, s_\alpha, s_\gamma, t_\alpha) \right). \quad (\text{G.32})$$

As before an intermediate resulting from a sole integration on φ significantly reduce computational cost. Eventually, total density field is given by

$$h_{\alpha\gamma}^{D_{\text{total}}} = h_{\alpha\gamma}^D + h_{\alpha\gamma}^{DR} . \quad (\text{G.33})$$

G.5 Spin-orbit term

By definition the spin-orbit term is

$$V^{\text{SO}}(\mathbf{r}_1, \mathbf{r}_2) = \frac{i}{4} W_{\text{LS}} \left(\overleftarrow{\nabla}_1 - \overleftarrow{\nabla}_2 \right) \times \delta^{(3)}(\mathbf{r}_1 - \mathbf{r}_2) \left(\overrightarrow{\nabla}_1 - \overrightarrow{\nabla}_2 \right) \cdot (\boldsymbol{\sigma}_1 + \boldsymbol{\sigma}_2) . \quad (\text{G.34})$$

Defining

$$\mathbf{A} \equiv \left(\overleftarrow{\nabla}_1 - \overleftarrow{\nabla}_2 \right) \times \delta^{(3)}(\mathbf{r}_1 - \mathbf{r}_2) \left(\overrightarrow{\nabla}_1 - \overrightarrow{\nabla}_2 \right) , \quad (\text{G.35})$$

$$\boldsymbol{\sigma} \equiv \boldsymbol{\sigma}_1 + \boldsymbol{\sigma}_2 , \quad (\text{G.36})$$

one has, using the cylindrical coordinates described in App. E

$$\begin{aligned} V^{\text{SO}} &= \frac{i}{4} W_{\text{LS}} \mathbf{A} \cdot \boldsymbol{\sigma} \\ &= \frac{i}{4} W_{\text{LS}} \left(-A^+ \sigma^- - A^- \sigma^+ + A^3 \sigma^3 \right) . \end{aligned} \quad (\text{G.37})$$

From Eq. (E.3)

$$A^+ = i \left[\overleftarrow{\nabla}_{12}^3 \delta_{12} \overrightarrow{\nabla}_{12}^+ - \overleftarrow{\nabla}_{12}^+ \delta_{12} \overrightarrow{\nabla}_{12}^3 \right] , \quad (\text{G.38})$$

$$A^- = i \left[\overleftarrow{\nabla}_{12}^- \delta_{12} \overrightarrow{\nabla}_{12}^3 - \overleftarrow{\nabla}_{12}^3 \delta_{12} \overrightarrow{\nabla}_{12}^- \right] , \quad (\text{G.39})$$

$$A^3 = i \left[\overleftarrow{\nabla}_{12}^- \delta_{12} \overrightarrow{\nabla}_{12}^+ - \overleftarrow{\nabla}_{12}^+ \delta_{12} \overrightarrow{\nabla}_{12}^- \right] , \quad (\text{G.40})$$

with

$$\nabla_{12} \equiv \nabla_1 - \nabla_2 , \quad (\text{G.41})$$

$$\delta_{12} \equiv \delta^{(3)}(\mathbf{r}_1 - \mathbf{r}_2) . \quad (\text{G.42})$$

The antisymmetrized spin-orbit matrix element can be expressed as

$$\bar{V}_{\alpha\beta\gamma\delta}^{\text{SO}} \equiv V_{\alpha\beta\gamma\delta}^{\text{SO}} - V_{\alpha\beta\delta\gamma}^{\text{SO}} = \frac{i}{4} W_{\text{LS}} \langle \alpha\beta | \mathbf{A} \cdot \boldsymbol{\sigma} (|\gamma\delta\rangle - |\delta\gamma\rangle) \rangle \quad (\text{G.43})$$

$$= \frac{i}{4} W_{\text{LS}} \left\{ \langle \psi_\alpha \psi_\beta | \mathbf{A} | \psi_\gamma \psi_\delta \rangle \cdot \langle s_\alpha t_\alpha s_\beta t_\beta | \boldsymbol{\sigma} | s_\gamma t_\gamma s_\delta t_\delta \rangle \right. \quad (\text{G.44})$$

$$\left. - \langle \psi_\alpha \psi_\beta | \mathbf{A} | \psi_\delta \psi_\gamma \rangle \cdot \langle s_\alpha t_\alpha s_\beta t_\beta | \boldsymbol{\sigma} | s_\delta t_\delta s_\gamma t_\gamma \rangle \right\} , \quad (\text{G.45})$$

where $|\alpha\rangle = |\psi_\alpha\rangle \otimes |s_\alpha t_\alpha\rangle$ has been used. The antisymmetry of $\langle \psi_\alpha \psi_\beta | \mathbf{A} | \psi_\gamma \psi_\delta \rangle$ with respect to its last two indices implies

$$\bar{V}_{\alpha\beta\gamma\delta}^{\text{SO}} = \frac{i W_{\text{LS}}}{4} \langle \psi_\alpha \psi_\beta | \mathbf{A} | \psi_\gamma \psi_\delta \rangle \cdot \left\{ \langle s_\alpha s_\beta | \boldsymbol{\sigma} | s_\gamma s_\delta \rangle \delta_{t_\alpha t_\gamma} \delta_{t_\beta t_\delta} + \langle s_\alpha s_\beta | \boldsymbol{\sigma} | s_\delta s_\gamma \rangle \delta_{t_\alpha t_\delta} \delta_{t_\beta t_\gamma} \right\} \quad (\text{G.46})$$

Using the formulas (E.4) the terms $\langle s_\alpha s_\beta | \sigma | s_\gamma s_\delta \rangle$ are given by

$$\begin{aligned} \langle s_\alpha s_\beta | \sigma^+ | s_\gamma s_\delta \rangle &= -\sqrt{2} (\delta_{s_\alpha+} \delta_{s_\gamma-} \delta_{s_\beta s_\delta} + \delta_{s_\beta+} \delta_{s_\delta-} \delta_{s_\alpha s_\gamma}) \\ &= \langle s_\alpha s_\beta | \sigma^+ | s_\delta s_\gamma \rangle , \end{aligned}$$

$$\begin{aligned} \langle s_\alpha s_\beta | \sigma^- | s_\gamma s_\delta \rangle &= \sqrt{2} (\delta_{s_\alpha-} \delta_{s_\gamma+} \delta_{s_\beta s_\delta} + \delta_{s_\beta-} \delta_{s_\delta+} \delta_{s_\alpha s_\gamma}) \\ &= \langle s_\alpha s_\beta | \sigma^- | s_\delta s_\gamma \rangle \end{aligned}$$

$$\begin{aligned} \langle s_\alpha s_\beta | \sigma^3 | s_\gamma s_\delta \rangle &= (\delta_{s_\alpha+} \delta_{s_\gamma+} - \delta_{s_\alpha-} \delta_{s_\gamma-}) (\delta_{s_\beta+} \delta_{s_\delta+} + \delta_{s_\beta-} \delta_{s_\delta-}) \\ &\quad + (\delta_{s_\beta+} \delta_{s_\delta+} - \delta_{s_\beta-} \delta_{s_\delta-}) (\delta_{s_\alpha+} \delta_{s_\gamma+} + \delta_{s_\alpha-} \delta_{s_\gamma-}) \\ &= \langle s_\alpha s_\beta | \sigma^3 | s_\delta s_\gamma \rangle \end{aligned}$$

As seen in Eqs. (G.47), (G.47) and (G.47) the quantity $\langle s_\alpha s_\beta | \sigma | s_\gamma s_\delta \rangle$ is symmetric with respect to s_γ, s_δ . Thus one have

$$\bar{V}_{\alpha\beta\gamma\delta}^{\text{SO}} = \frac{iW_{\text{LS}}}{4} \langle \psi_\alpha \psi_\beta | \mathbf{A} | \psi_\gamma \psi_\delta \rangle \cdot \langle \alpha \beta | \sigma | \gamma \delta \rangle \langle t_\alpha t_\beta | T | t_\gamma t_\delta \rangle , \quad (\text{G.47})$$

where, by definition

$$\langle t_\alpha t_\beta | T | t_\gamma t_\delta \rangle \equiv \delta_{t_\alpha t_\gamma} \delta_{t_\beta t_\delta} + \delta_{t_\alpha t_\delta} \delta_{t_\beta t_\gamma} . \quad (\text{G.48})$$

The last equation can be recast (using Eq.(E.2)) as

$$\begin{aligned} \bar{V}_{\alpha\beta\gamma\delta}^{\text{SO}} &= \frac{iW_{\text{LS}}}{4} \left\{ -\langle \psi_\alpha \psi_\beta | A^+ | \psi_\gamma \psi_\delta \rangle \langle s_\alpha s_\beta | \sigma^- | s_\gamma s_\delta \rangle \right. \\ &\quad - \langle \psi_\alpha \psi_\beta | A^- | \psi_\gamma \psi_\delta \rangle \langle s_\alpha s_\beta | \sigma^+ | s_\gamma s_\delta \rangle \\ &\quad \left. + \langle \psi_\alpha \psi_\beta | A^3 | \psi_\gamma \psi_\delta \rangle \langle s_\alpha s_\beta | \sigma^3 | s_\gamma s_\delta \rangle \right\} \langle t_\alpha t_\beta | T | t_\gamma t_\delta \rangle . \quad (\text{G.49}) \end{aligned}$$

The spatial factor $\langle \psi_\alpha \psi_\beta | \mathbf{A} | \psi_\gamma \psi_\delta \rangle$ can be written in term of spatial integrals

$$\langle \psi_\alpha \psi_\beta | \mathbf{A} | \psi_\gamma \psi_\delta \rangle = \int d^3 \mathbf{r} (\psi_\beta^* \nabla \psi_\alpha^* - \psi_\alpha^* \nabla \psi_\beta^*) \times (\psi_\delta \nabla \psi_\gamma - \psi_\gamma \nabla \psi_\delta) \quad (\text{G.50a})$$

$$= 2 \int d^3 \mathbf{r} (\nabla \psi_\alpha^* \times \nabla \psi_\gamma) \psi_\beta^* \psi_\delta + 2 \int d^3 \mathbf{r} (\nabla \psi_\beta^* \times \nabla \psi_\delta) \psi_\alpha^* \psi_\gamma . \quad (\text{G.50b})$$

Defining

$$\mathbf{I}_{\alpha\beta\gamma\delta} \equiv \int d^3 \mathbf{r} (\nabla \psi_\alpha^* \times \nabla \psi_\gamma) \psi_\beta^* \psi_\delta . \quad (\text{G.51})$$

One has

$$\begin{aligned} I_{\alpha\beta\gamma\delta}^+ &= \int d^3 \mathbf{r} (\nabla \psi_\alpha^* \times \nabla \psi_\gamma)^+ \psi_\beta^* \psi_\delta \\ &= i \int dz \nabla^3 \psi_\alpha^{(1)*} \psi_\gamma^{(1)} \psi_\beta^{(1)*} \psi_\delta^{(1)} \int d^2 r \nabla^+ \psi_\gamma^{(2)} \psi_\alpha^{(2)*} \psi_\beta^{(2)*} \psi_\delta^{(2)} \\ &\quad - i \int dz \nabla^3 \psi_\gamma^{(1)} \psi_\alpha^{(1)*} \psi_\beta^{(1)*} \psi_\delta^{(1)} \int d^2 r \nabla^+ \psi_\alpha^{(2)*} \psi_\gamma^{(2)} \psi_\beta^{(2)*} \psi_\delta^{(2)} , \quad (\text{G.52}) \end{aligned}$$

$$\begin{aligned}
I_{\alpha\beta\gamma\delta}^- &= \int d^3\mathbf{r}(\nabla\psi_\alpha^* \times \nabla\psi_\gamma)^- \psi_\beta^* \psi_\delta \\
&= i \int dz \nabla^3 \psi_\gamma^{(1)} \psi_\alpha^{(1)*} \psi_\beta^{(1)*} \psi_\delta^{(1)} \int d^2r \nabla^- \psi_\alpha^{(2)*} \psi_\gamma^{(2)} \psi_\beta^{(2)*} \psi_\delta^{(2)} \\
&\quad - i \int dz \nabla^3 \psi_\alpha^{(1)*} \psi_\gamma^{(1)} \psi_\beta^{(1)*} \psi_\delta^{(1)} \int d^2r \nabla^- \psi_\gamma^{(2)} \psi_\alpha^{(2)*} \psi_\beta^{(2)*} \psi_\delta^{(2)} , \tag{G.53}
\end{aligned}$$

$$\begin{aligned}
I_{\alpha\beta\gamma\delta}^3 &= \int d^3\mathbf{r}(\nabla\psi_\alpha^* \times \nabla\psi_\gamma)^3 \psi_\beta^* \psi_\delta \\
&= i \int dz \psi_\alpha^{(1)*} \psi_\gamma^{(1)} \psi_\beta^{(1)*} \psi_\delta^{(1)} \times \int d^2r \nabla^- \psi_\alpha^{(2)*} \nabla^+ \psi_\gamma^{(2)} \psi_\beta^{(2)*} \psi_\delta^{(2)} \\
&\quad - i \int dz \psi_\alpha^{(1)*} \psi_\gamma^{(1)} \psi_\beta^{(1)*} \psi_\delta^{(1)} \int d^2r \nabla^+ \psi_\alpha^{(2)*} \nabla^- \psi_\gamma^{(2)} \psi_\beta^{(2)*} \psi_\delta^{(2)} \Big] . \tag{G.54}
\end{aligned}$$

By defining

$$K_{\alpha\beta\gamma\delta} \equiv \int dz \psi_\alpha^{(1)} \psi_\beta^{(1)} \psi_\gamma^{(1)} \psi_\delta^{(1)} , \tag{G.55}$$

$$L_{\alpha\beta\gamma\delta} \equiv \int d^2r \psi_\alpha^{(2)} \psi_\beta^{(2)} \psi_\gamma^{(2)} \psi_\delta^{(2)} , \tag{G.56}$$

$$M_{\alpha\beta\gamma\delta} \equiv \int dz \nabla^3 \psi_\alpha^{(1)} \psi_\beta^{(1)} \psi_\gamma^{(1)} \psi_\delta^{(1)} , \tag{G.57}$$

$$N_{\alpha\beta\gamma\delta}^+ \equiv \int d^2r \nabla^+ \psi_\alpha^{(2)} \psi_\beta^{(2)} \psi_\gamma^{(2)} \psi_\delta^{(2)} , \tag{G.58}$$

$$N_{\alpha\beta\gamma\delta}^- \equiv \int d^2r \nabla^- \psi_\alpha^{(2)} \psi_\beta^{(2)} \psi_\gamma^{(2)} \psi_\delta^{(2)} , \tag{G.59}$$

$$N_{\alpha\beta\gamma\delta}^{+-} \equiv \int d^2r \nabla^+ \psi_\alpha^{(2)} \nabla^- \psi_\beta^{(2)} \psi_\gamma^{(2)} \psi_\delta^{(2)} , \tag{G.60}$$

one can write

$$I_{\alpha\beta\gamma\delta}^+ = i \left(M_{\alpha\beta\gamma\delta} N_{\underline{\gamma}\underline{\alpha}\underline{\beta}\underline{\delta}}^+ - M_{\gamma\alpha\beta\delta} N_{\underline{\alpha}\underline{\beta}\underline{\gamma}\underline{\delta}}^+ \right) , \tag{G.61}$$

$$I_{\alpha\beta\gamma\delta}^- = i \left(M_{\gamma\alpha\beta\delta} N_{\underline{\alpha}\underline{\gamma}\underline{\beta}\underline{\delta}}^- - M_{\alpha\beta\gamma\delta} N_{\underline{\gamma}\underline{\alpha}\underline{\beta}\underline{\delta}}^- \right) , \tag{G.62}$$

$$I_{\alpha\beta\gamma\delta}^3 = -i K_{\alpha\beta\gamma\delta} \left(N_{\underline{\alpha}\underline{\gamma}\underline{\beta}\underline{\delta}}^{+-} - N_{\underline{\gamma}\underline{\alpha}\underline{\beta}\underline{\delta}}^{+-} \right) , \tag{G.63}$$

where the underline indicates complex conjugation, more precisely, if $\alpha = (m_\alpha, n_\alpha, n_{z\alpha})$ then $\underline{\alpha} \equiv (-m_\alpha, n_\alpha, n_{z\alpha})$. From the recurrence relations developed in App. F, one can express M, N^+, N^- and N^{+-} in terms of K and L

$$\begin{aligned}
M_{\alpha\beta\gamma\delta} &= \int dz \nabla^3 \psi_\alpha^{(1)} \psi_\beta^{(1)} \psi_\gamma^{(1)} \psi_\delta^{(1)} \\
&= \frac{1}{b_z \sqrt{2}} \int dz \left(\sqrt{n_{z\alpha}} \psi_{n_{z\alpha}-1} - \sqrt{n_{z\alpha}+1} \right) \psi_\beta^{(1)} \psi_\gamma^{(1)} \psi_\delta^{(1)} \\
&= \frac{1}{b_z \sqrt{2}} \left(\sqrt{n_{z\alpha}} K(n_{z\alpha}-1, n_{z\beta}, n_{z\gamma}, n_{z\delta}) - \sqrt{n_{z\alpha}+1} K(n_{z\alpha}+1, n_{z\beta}, n_{z\gamma}, n_{z\delta}) \right) ,
\end{aligned}$$

(G.64)

$$\begin{aligned}
N_{\alpha\beta\gamma\delta}^+ &= \int d^2r \nabla^+ \psi_\alpha^{(2)} \psi_\beta^{(2)} \psi_\gamma^{(2)} \psi_\delta^{(2)} \\
&= \frac{(-1)^{\delta(m_\alpha \leq -1)}}{b_r \sqrt{2}} \left[\sqrt{n_\alpha + \delta(m_\alpha \leq -1)} L(m_\alpha + 1, n_\alpha + (-1)^{\delta(m_\alpha \geq 0)}, m_\beta, n_\beta, m_\gamma, n_\gamma, m_\delta, n_\delta) \right. \\
&\quad \left. + \sqrt{n_\alpha + |m_\alpha| + \delta(m_\alpha \geq 0)} L(m_\alpha + 1, n_\alpha, m_\beta, n_\beta, m_\gamma, n_\gamma, m_\delta, n_\delta) \right], \tag{G.65}
\end{aligned}$$

$$\begin{aligned}
N_{\alpha\beta\gamma\delta}^- &= \int d^2r \nabla^- \psi_\alpha^{(2)} \psi_\beta^{(2)} \psi_\gamma^{(2)} \psi_\delta^{(2)} \\
&= \frac{(-1)^{\delta(m_\alpha \leq 0)}}{b_r \sqrt{2}} \left[\sqrt{n_\alpha + \delta(m_\alpha \geq 1)} L(m_\alpha - 1, n_\alpha + (-1)^{\delta(m_\alpha \leq 0)}, m_\beta, n_\beta, m_\gamma, n_\gamma, m_\delta, n_\delta) \right. \\
&\quad \left. + \sqrt{n_\alpha + |m_\alpha| + \delta(m_\alpha \leq 0)} L(m_\alpha - 1, n_\alpha, m_\beta, n_\beta, m_\gamma, n_\gamma, m_\delta, n_\delta) \right], \tag{G.66}
\end{aligned}$$

$$\begin{aligned}
N_{\alpha\beta\gamma\delta}^{+-} &= \int d^2r \nabla^+ \psi_\alpha^{(2)} \nabla^- \psi_\beta^{(2)} \psi_\gamma^{(2)} \psi_\delta^{(2)} \\
&= \frac{(-1)^{\delta(m_\beta \leq 0)}}{b_r \sqrt{2}} \left[\sqrt{n_\beta + \delta(m_\beta \geq 1)} N^+(m_\alpha, n_\alpha, m_\beta - 1, n_\beta + (-1)^{\delta(m_\beta \leq 0)}, m_\gamma, n_\gamma, m_\delta, n_\delta) \right. \\
&\quad \left. + \sqrt{n_\beta + |m_\beta| + \delta(m_\beta \leq 0)} N^+(m_\alpha, n_\alpha, m_\beta - 1, n_\beta, m_\beta, n_\gamma, m_\delta, n_\delta) \right]. \tag{G.67}
\end{aligned}$$

It remains to develop expressions for K and L , for K (using Eqs. (C.15b) and (C.16b))

$$\begin{aligned}
K_{\alpha\beta\gamma\delta} &= \int dz \psi_\alpha^{(1)} \psi_\beta^{(1)} \psi_\gamma^{(1)} \psi_\delta^{(1)} \\
&= \frac{1}{\sqrt{b_z} \sqrt{\pi}} \sum_n T_{\gamma\delta}^{(1)n} \int dz e^{-\frac{1}{2} \frac{z^2}{b_z^2}} \psi_\alpha^{(1)} \psi_\beta^{(1)} \psi_n^{(1)} \\
&= \frac{1}{b_z \pi^{1/4}} \sum_n T_{\gamma\delta}^{(1)n} \delta(2n_{z\alpha} + n_{z\beta} + n) \frac{1}{\sqrt{2\pi^{7/2}}} \frac{\Gamma(\xi - n_{z\alpha}) \Gamma(\xi - n_{z\beta}) \Gamma(\xi - n)}{\sqrt{n_{z\alpha}! n_{z\beta}! n!}} \\
&= \frac{1}{b_z \pi^2 \sqrt{2}} \delta(2n_{z\alpha} + n_{z\beta} + n_{z\gamma} + n_{z\delta}) \sum_n T_{\gamma\delta}^{(1)n} \frac{\Gamma(\xi - n_{z\alpha}) \Gamma(\xi - n_{z\beta}) \Gamma(\xi - n)}{\sqrt{n_{z\alpha}! n_{z\beta}! n!}}, \tag{G.68}
\end{aligned}$$

and (using Eqs. (C.15c) and (C.16c))

$$\begin{aligned}
L_{\alpha\beta\gamma\delta} &= \int d^2r \psi_\alpha^{(2)} \psi_\beta^{(2)} \psi_\gamma^{(2)} \psi_\delta^{(2)} \\
&= \frac{1}{b_r^2 \pi} \sum_{\mu\nu} T_{\underline{\alpha}\gamma}^{(2)\mu} T_{\underline{\beta}\delta}^{(2)\nu} \int d^2r e^{-\frac{r^2}{b_r^2}} \psi_\mu^{(2)} \psi_\nu^{(2)} \\
&= \frac{1}{b_r^2 \pi} \sum_{\mu\nu} T_{\underline{\alpha}\gamma}^{(2)\mu} T_{\underline{\beta}\delta}^{(2)\nu} I(m_\mu, n_\mu; m_\nu, n_\nu; b_r, b_r). \tag{G.69}
\end{aligned}$$

Thus one can write

$$\begin{aligned} \overline{V}_{\alpha\beta\gamma\delta}^{\text{SO}} = & \frac{iW_{\text{LS}}}{2} \left[-\left(I_{\alpha\beta\gamma\delta}^+ + I_{\beta\alpha\delta\gamma}^+\right) \langle s_\alpha s_\beta | \sigma^- | s_\gamma s_\delta \rangle \right. \\ & - \left. \left(I_{\alpha\beta\gamma\delta}^- + I_{\beta\alpha\delta\gamma}^-\right) \langle s_\alpha s_\beta | \sigma^+ | s_\gamma s_\delta \rangle \right. \\ & \left. + \left(I_{\alpha\beta\gamma\delta}^3 + I_{\beta\alpha\delta\gamma}^3\right) \langle s_\alpha s_\beta | \sigma^3 | s_\gamma s_\delta \rangle \right] \langle t_\alpha t_\beta | T | t_\gamma t_\delta \rangle \end{aligned} \quad (\text{G.70})$$

Spin-orbit fields

For the computation of spin-orbit fields, introducing the intermediary quantities

$$Y_{\text{L}}^1(m_\alpha, m_\gamma)(n_\alpha, n_\gamma, n_\mu) \equiv T_{(-m_\alpha, n_\alpha)(m_\gamma, n_\gamma)}^{(2)n_\mu} \quad , \quad (\text{G.71a})$$

$$Y_{\text{L}}^2(m_\beta, m_\delta)(n_\beta, n_\delta, n_\mu) \equiv \sum_{n_\nu} T_{(-m_\beta, n_\beta)(m_\delta, n_\delta)}^{(2)n_\nu} I(-m_\delta - m_\beta, n_\mu; m_\delta + m_\beta, n_\nu) \quad , \quad (\text{G.71b})$$

such that

$$L_{\alpha\beta\gamma\delta} = \frac{1}{b_r^2 \pi} \sum_{n_\mu} \delta(m_\alpha + m_\beta + m_\gamma + m_\delta = 0) Y_{\text{L}}^1(m_\alpha, m_\gamma)(n_\alpha, n_\gamma, n_\mu) Y_{\text{L}}^2(m_\beta, m_\delta)(n_\beta, n_\delta, n_\mu) \quad . \quad (\text{G.72})$$

Similarly introducing

$$X_{\text{K}}^1(n_{z\alpha}, n_{z\gamma}, n_z) \equiv T_{n_{z\alpha} n_{z\gamma}}^{n_z} \quad (\text{G.73a})$$

$$X_{\text{K}}^2(n_{z\beta}, n_{z\delta}, n_z) \equiv \delta(2|n_{z\beta} + n_{z\delta} + n_z) \frac{\Gamma(\xi - n_{z\beta})\Gamma(\xi - n_{z\delta})\Gamma(\xi - n_z)}{\sqrt{n_{z\beta}! n_{z\delta}! n_z!}} \quad (\text{G.73b})$$

with $\xi = \frac{n_{z\beta} + n_{z\delta} + n_z}{2} + \frac{1}{2}$. Such that

$$K_{\alpha\beta\gamma\delta} = \frac{1}{b_z \pi^2 \sqrt{2}} \sum_{n_z} X_{\text{K}}^1(n_{z\alpha}, n_{z\gamma}, n_z) X_{\text{K}}^2(n_{z\beta}, n_{z\delta}, n_z) \quad . \quad (\text{G.74})$$

Introducing

$$X_{\text{M}}^1(n_{z\alpha}, n_{z\gamma}, n_z) \equiv \sqrt{n_{z\alpha}} X_{\text{K}}^1(n_{z\alpha} - 1, n_{z\gamma}, n_z) - \sqrt{n_{z\alpha} + 1} X_{\text{K}}^1(n_{z\alpha} + 1, n_{z\gamma}, n_z) \quad , \quad (\text{G.75a})$$

$$X_{\text{M}}^2(n_{z\beta}, n_{z\delta}, n_z) \equiv X_{\text{K}}^2(n_{z\beta}, n_{z\delta}, n_z) \quad , \quad (\text{G.75b})$$

such that

$$M_{\alpha\beta\gamma\delta} = \frac{1}{2b_z^2 \pi^2} \sum_{n_z} X_{\text{M}}^1(n_{z\alpha}, n_{z\gamma}, n_z) X_{\text{M}}^2(n_{z\beta}, n_{z\delta}, n_z) \quad . \quad (\text{G.76})$$

Introducing

$$\begin{aligned} Y_{\text{N}}^1(m_\alpha, m_\gamma)(n_\alpha, n_\gamma, n_\mu) \equiv & (-1)^{\delta(m_\alpha \leq 0)} \\ & \times \left[\sqrt{n_\alpha + \delta(m_\alpha \geq 1)} Y_{\text{L}}^1(m_\alpha - 1, m_\gamma)(n_\alpha + (-1)^{\delta(m_\alpha \leq 0)}, n_\gamma, n_\mu) \right. \\ & \left. + \sqrt{n_\alpha + |m_\alpha| + \delta(m_\alpha \leq 0)} Y_{\text{L}}^1(m_\alpha - 1, m_\gamma)(n_\alpha, n_\gamma, n_\mu) \right] \quad , \quad (\text{G.77a}) \end{aligned}$$

$$Y_{N^-}^2(m_\beta, m_\delta)(n_\beta, n_\delta, n_\mu) \equiv Y_L^2(m_\beta, m_\delta)(n_\beta, n_\delta, n_\mu) , \quad (\text{G.77b})$$

such that

$$N_{\alpha\beta\gamma\delta}^- = \frac{1}{b_r^3 \pi \sqrt{2}} \sum_{n_\mu} \delta(m_\alpha + m_\beta + m_\gamma + m_\delta = 1) Y_{N^-}^1(m_\alpha, m_\gamma)(n_\alpha, n_\gamma, n_\mu) Y_{N^-}^2(m_\beta, m_\delta)(n_\beta, n_\delta, n_\mu) . \quad (\text{G.78})$$

Introducing

$$\begin{aligned} Y_{N^+}^1(m_\alpha, m_\gamma)(n_\alpha, n_\gamma, n_\mu) &\equiv (-1)^{\delta(m_\alpha \leq -1)} \\ &\times \left[\sqrt{n_\alpha + \delta(m_\alpha \leq -1)} Y_L^1(m_\alpha + 1, m_\gamma)(n_\alpha + (-1)^{\delta(m_\alpha \geq 0)}, n_\gamma, n_\mu) \right. \\ &\left. + \sqrt{n_\alpha + |m_\alpha| + \delta(m_\alpha \geq 0)} Y_L^1(m_\alpha + 1, m_\gamma)(n_\alpha, n_\gamma, n_\mu) \right] , \end{aligned} \quad (\text{G.79a})$$

$$Y_{N^+}^2(m_\beta, m_\delta)(n_\beta, n_\delta, n_\mu) \equiv Y_L^2(m_\beta, m_\delta)(n_\beta, n_\delta, n_\mu) , \quad (\text{G.79b})$$

such that

$$N_{\alpha\beta\gamma\delta}^+ = \frac{1}{b_r^3 \pi \sqrt{2}} \sum_{n_\mu} \delta(m_\alpha + m_\beta + m_\gamma + m_\delta = -1) Y_{N^+}^1(m_\alpha, m_\gamma)(n_\alpha, n_\gamma, n_\mu) Y_{N^+}^2(m_\beta, m_\delta)(n_\beta, n_\delta, n_\mu) . \quad (\text{G.80})$$

Introducing

$$Y_{N^{+-}}^1(m_\alpha, m_\gamma)(n_\alpha, n_\gamma, n_\mu) \equiv Y_{N^+}^1(m_\alpha, m_\gamma)(n_\alpha, n_\gamma, n_\mu) , \quad (\text{G.81a})$$

$$Y_{N^{+-}}^2(m_\beta, m_\delta)(n_\beta, n_\delta, n_\mu) \equiv Y_{N^+}^2(m_\beta, m_\delta)(n_\beta, n_\delta, n_\mu) , \quad (\text{G.81b})$$

such that

$$N_{\alpha\beta\gamma\delta}^{+-} = \frac{1}{2\pi b_r^4} \sum_{n_\mu} \delta(m_\alpha + m_\beta + m_\gamma + m_\delta = 0) Y_{N^{+-}}^1(m_\alpha, m_\gamma)(n_\alpha, n_\gamma, n_\mu) Y_{N^{+-}}^2(m_\beta, m_\delta)(n_\beta, n_\delta, n_\mu) . \quad (\text{G.82})$$

Introducing

$$\begin{aligned} \hat{Y}_{N^{+-}}^1(m_\alpha, m_\beta)(n_\alpha, n_\beta, n_\mu) &\equiv (-1)^{\delta(m_\beta \leq 0)} (-1)^{\delta(m_\alpha \leq -1)} \\ &\times \left(\sqrt{n_\alpha + \delta(m_\alpha \leq -1)} \sqrt{n_\beta + \delta(m_\beta \geq 1)} \right. \\ &\quad \times Y_L^1(m_\alpha + 1, m_\beta - 1)(n_\alpha + (-1)^{\delta(m_\alpha \geq 0)}, n_\beta + (-1)^{\delta(m_\beta \leq 0)}, n_\mu) \\ &\quad + \sqrt{n_\alpha + \delta(m_\alpha \leq -1)} \sqrt{n_\beta + |m_\beta| + \delta(m_\beta \leq 0)} \\ &\quad \times Y_L^1(m_\alpha + 1, m_\beta - 1)(n_\alpha + (-1)^{\delta(m_\alpha \geq 0)}, n_\beta, n_\mu) \\ &\quad + \sqrt{n_\alpha + |m_\alpha| + \delta(m_\alpha \geq 0)} \sqrt{n_\beta + \delta(m_\beta \geq 1)} \\ &\quad \times Y_L^1(m_\alpha + 1, m_\beta - 1)(n_\alpha, n_\beta + (-1)^{\delta(m_\beta \leq 0)}, n_\mu) \\ &\quad \left. + \sqrt{n_\alpha + |m_\alpha| + \delta(m_\alpha \geq 0)} \sqrt{n_\beta + |m_\beta| + \delta(m_\beta \leq 0)} \right. \\ &\quad \left. \times Y_L^1(m_\alpha + 1, m_\beta - 1)(n_\alpha, n_\beta, n_\mu) \right) , \end{aligned} \quad (\text{G.83a})$$

$$\hat{Y}_{N^{+-}}^2(m_\gamma, m_\delta)(n_\gamma, n_\delta, n_\mu) \equiv Y_L^2(m_\gamma, m_\delta)(n_\gamma, n_\delta, n_\mu) , \quad (\text{G.83b})$$

such that

$$N_{\alpha\beta\gamma\delta}^{+-} = \frac{1}{2\pi b_r^4} \sum_{n_\mu} \delta(m_\alpha + m_\beta + m_\gamma + m_\delta = 0) \hat{Y}_{N^{+-}}^1(m_\alpha, m_\beta)(n_\alpha, n_\beta, n_\mu) \hat{Y}_{N^{+-}}^2(m_\gamma, m_\delta)(n_\gamma, n_\delta, n_\mu) . \quad (\text{G.84})$$

Using above developed formulas, the calculation of spin-orbit fields involves to compute the following intermediary quantities

$$\begin{aligned} A_1(m, s_\beta, s_\delta, t_\beta)(n_z, n_\mu) &\equiv \sum_{m_\beta m_\delta} \sum_{n_\beta n_\delta} \sum_{n_z \beta n_{z\delta}} \delta(m_\beta - m_\delta = m) \\ &\times X_K^2(n_{z\beta}, n_{z\delta}, n_z) \rho_{db} Y_{N^-}^2(-m_\beta, m_\delta)(n_\beta, n_\delta, n_\mu) , \end{aligned} \quad (\text{G.85})$$

$$\begin{aligned} B_1(m, s_\beta, s_\delta, t_\beta)(n_z, n_\mu) &\equiv \sum_{m_\beta m_\delta} \sum_{n_\beta n_\delta} \sum_{n_z \beta n_{z\delta}} \delta(m_\beta - m_\delta = m) \\ &\left[X_M^1(n_{z\beta}, n_{z\delta}, n_z) \rho_{db} Y_{N^+}^1(m_\delta, -m_\beta)(n_\delta, n_\beta, n_\mu) \right. \\ &\left. - X_M^1(n_{z\delta}, n_{z\beta}, n_z) \rho_{db} Y_{N^+}^1(-m_\beta, m_\delta)(n_\beta, n_\delta, n_\mu) \right] , \end{aligned} \quad (\text{G.86})$$

$$\begin{aligned} D_1(m, s_\beta, s_\delta, t_\beta)(n_z, n_\mu) &\equiv \sum_{m_\beta m_\delta} \sum_{n_\beta n_\delta} \sum_{n_z \beta n_{z\delta}} \delta(m_\beta - m_\delta = m) \\ &\left[-X_M^1(n_{z\beta}, n_{z\delta}, n_z) \rho_{db} Y_{N^-}^1(m_\delta, -m_\beta)(n_\delta, n_\beta, n_\mu) \right. \\ &\left. + X_M^1(n_{z\delta}, n_{z\beta}, n_z) \rho_{db} Y_{N^-}^1(-m_\beta, m_\delta)(n_\beta, n_\delta, n_\mu) \right] , \end{aligned} \quad (\text{G.87})$$

$$\begin{aligned} F_1(m, s_\beta, s_\delta, t_\beta)(n_z, n_\mu) &\equiv \sum_{m_\beta m_\delta} \sum_{n_\beta n_\delta} \sum_{n_z \beta n_{z\delta}} \delta(m_\beta - m_\delta = m) \\ &\left[X_K^2(n_{z\beta}, n_{z\delta}, n_z) \rho_{db} \hat{Y}_{N^{+-}}^1(-m_\beta, m_\delta)(n_\beta, n_\delta, n_\mu) \right. \\ &\left. - X_K^2(n_{z\beta}, n_{z\delta}, n_z) \rho_{db} \hat{Y}_{N^{+-}}^1(m_\delta, -m_\beta)(n_\delta, n_\beta, n_\mu) \right] , \end{aligned} \quad (\text{G.88})$$

$$\begin{aligned} \tilde{A}_1(m, s_\gamma, s_\delta, t_\gamma)(n_z, n_\mu) &\equiv \sum_{m_\gamma m_\delta} \sum_{n_\gamma n_\delta} \sum_{n_z \gamma n_{z\delta}} \delta(m_\gamma + m_\delta = m) \\ &\times X_K^2(n_{z\gamma}, n_{z\delta}, n_z) \kappa_{\gamma\delta} Y_{N^+}^1(m_\gamma, m_\delta)(n_\gamma, n_\delta, n_\mu) , \end{aligned} \quad (\text{G.89})$$

$$\begin{aligned} \tilde{B}_1(m, s_\gamma, s_\delta, t_\gamma)(n_z, n_\mu) &\equiv \sum_{m_\gamma m_\delta} \sum_{n_\gamma n_\delta} \sum_{n_z \gamma n_{z\delta}} \delta(m_\gamma + m_\delta = m) \\ &\times X_M^1(n_{z\gamma}, n_{z\delta}, n_z) \kappa_{\gamma\delta} Y_{N^-}^2(m_\gamma, m_\delta)(n_\gamma, n_\delta, n_\mu) , \end{aligned} \quad (\text{G.90})$$

$$\begin{aligned} \tilde{D}_1(m, s_\gamma, s_\delta, t_\gamma)(n_z, n_\mu) &\equiv \sum_{m_\gamma, m_\delta} \sum_{n_\gamma, n_\delta} \sum_{n_{z\gamma}, n_{z\delta}} \delta(m_\gamma + m_\delta = m) \\ &\quad \times X_K^2(n_{z\gamma}, n_{z\delta}, n_z) \kappa_{\gamma\delta} Y_{N^-}^1(m_\gamma, m_\delta)(n_\gamma, n_\delta, n_\mu) , \end{aligned} \quad (\text{G.91})$$

where intermediate quantities X_K^2 , $Y_{N^-}^2$, X_M^1 , $Y_{N^+}^1$, $Y_{N^-}^1$, $\hat{Y}_{N^+}^1$ have been defined by respectively Eqs. (G.73), (G.77), (G.75), (G.79), (G.77), (G.83). Next spin and isospin indices are contracted into new intermediate quantities

$$A_2(m, s_\alpha, s_\gamma, t_\alpha)(n_z, n_\mu) \equiv \sum_{s_\beta s_\delta} \sum_{t_\beta} \langle s_\alpha s_\beta | \sigma_1^- + \sigma_2^- | s_\gamma s_\delta \rangle \langle t_\alpha t_\beta | T | t_\gamma t_\delta \rangle A_1(m, s_\beta, s_\delta, t_\beta)(n_z, n_\mu) , \quad (\text{G.92a})$$

$$B_2(m, s_\alpha, s_\gamma, t_\alpha)(n_z, n_\mu) \equiv \sum_{s_\beta s_\delta} \sum_{t_\beta} \langle s_\alpha s_\beta | \sigma_1^- + \sigma_2^- | s_\gamma s_\delta \rangle \langle t_\alpha t_\beta | T | t_\gamma t_\delta \rangle B_1(m, s_\beta, s_\delta, t_\beta)(n_z, n_\mu) , \quad (\text{G.92b})$$

$$C_2(m, s_\alpha, s_\gamma, t_\alpha)(n_z, n_\mu) \equiv \sum_{s_\beta s_\delta} \sum_{t_\beta} \langle s_\alpha s_\beta | \sigma_1^+ + \sigma_2^+ | s_\gamma s_\delta \rangle \langle t_\alpha t_\beta | T | t_\gamma t_\delta \rangle A_1(m, s_\beta, s_\delta, t_\beta)(n_z, n_\mu) , \quad (\text{G.92c})$$

$$D_2(m, s_\alpha, s_\gamma, t_\alpha)(n_z, n_\mu) \equiv \sum_{s_\beta s_\delta} \sum_{t_\beta} \langle s_\alpha s_\beta | \sigma_1^+ + \sigma_2^+ | s_\gamma s_\delta \rangle \langle t_\alpha t_\beta | T | t_\gamma t_\delta \rangle D_1(m, s_\beta, s_\delta, t_\beta)(n_z, n_\mu) , \quad (\text{G.92d})$$

$$E_2(m, s_\alpha, s_\gamma, t_\alpha)(n_z, n_\mu) \equiv \sum_{s_\beta s_\delta} \sum_{t_\beta} \langle s_\alpha s_\beta | \sigma_1^3 + \sigma_2^3 | s_\gamma s_\delta \rangle \langle t_\alpha t_\beta | T | t_\gamma t_\delta \rangle A_1(m, s_\beta, s_\delta, t_\beta)(n_z, n_\mu) , \quad (\text{G.92e})$$

$$F_2(m, s_\alpha, s_\gamma, t_\alpha)(n_z, n_\mu) \equiv \sum_{s_\beta s_\delta} \sum_{t_\beta} \langle s_\alpha s_\beta | \sigma_1^3 + \sigma_2^3 | s_\gamma s_\delta \rangle \langle t_\alpha t_\beta | T | t_\gamma t_\delta \rangle F_1(m, s_\beta, s_\delta, t_\beta)(n_z, n_\mu) , \quad (\text{G.92f})$$

$$\tilde{A}_2(m, s_\alpha, s_\beta, t_\alpha)(n_z, n_\mu) \equiv \sum_{s_\gamma s_\delta} \sum_{t_\gamma} \langle s_\alpha s_\beta | \sigma_1^- + \sigma_2^- | s_\gamma s_\delta \rangle \langle t_\alpha t_\beta | t_\gamma t_\delta \rangle \tilde{A}_1(m, s_\gamma, s_\delta, t_\gamma)(n_z, n_\mu) , \quad (\text{G.92g})$$

$$\tilde{B}_2(m, s_\alpha, s_\beta, t_\alpha)(n_z, n_\mu) \equiv \sum_{s_\gamma s_\delta} \sum_{t_\gamma} \langle s_\alpha s_\beta | \sigma_1^- + \sigma_2^- | s_\gamma s_\delta \rangle \langle t_\alpha t_\beta | t_\gamma t_\delta \rangle \tilde{B}_1(m, s_\gamma, s_\delta, t_\gamma)(n_z, n_\mu) , \quad (\text{G.92h})$$

$$\tilde{C}_2(m, s_\alpha, s_\beta, t_\alpha)(n_z, n_\mu) \equiv \sum_{s_\gamma s_\delta} \sum_{t_\gamma} \langle s_\alpha s_\beta | \sigma_1^+ + \sigma_2^+ | s_\gamma s_\delta \rangle \langle t_\alpha t_\beta | t_\gamma t_\delta \rangle \tilde{B}_1(m, s_\gamma, s_\delta, t_\gamma)(n_z, n_\mu) , \quad (\text{G.92i})$$

$$\tilde{D}_2(m, s_\alpha, s_\beta, t_\alpha)(n_z, n_\mu) \equiv \sum_{s_\gamma s_\delta} \sum_{t_\gamma} \langle s_\alpha s_\beta | \sigma_1^+ + \sigma_2^+ | s_\gamma s_\delta \rangle \langle t_\alpha t_\beta | t_\gamma t_\delta \rangle \tilde{D}_1(m, s_\gamma, s_\delta, t_\gamma)(n_z, n_\mu) , \quad (\text{G.92j})$$

$$\tilde{E}_2(m, s_\alpha, s_\beta, t_\alpha)(n_z, n_\mu) \equiv \sum_{s_\gamma s_\delta} \sum_{t_\gamma} \langle s_\alpha s_\beta | \sigma_1^3 + \sigma_2^3 | s_\gamma s_\delta \rangle \langle t_\alpha t_\beta | t_\gamma t_\delta \rangle \tilde{D}_1(m, s_\gamma, s_\delta, t_\gamma)(n_z, n_\mu) , \quad (\text{G.92k})$$

$$\tilde{F}_2(m, s_\alpha, s_\beta, t_\alpha)(n_z, n_\mu) \equiv \sum_{s_\gamma s_\delta} \sum_{t_\gamma} \langle s_\alpha s_\beta | \sigma_1^3 + \sigma_2^3 | s_\gamma s_\delta \rangle \langle t_\alpha t_\beta | t_\gamma t_\delta \rangle \tilde{A}_1(m, s_\gamma, s_\delta, t_\gamma)(n_z, n_\mu) . \quad (\text{G.92l})$$

Spin-orbit fields can then be expressed as

$$\begin{aligned} h_{\alpha\gamma} &= \frac{W_{\text{LS}}}{4} \delta_{t_\alpha t_\gamma} \sum_{n_z n_\mu} \sum_m \left[f_1 X_M^1(n_{z\alpha}, n_{z\gamma}, n_z) Y_{N^+}^1(m_\gamma, -m_\alpha)(n_\alpha, n_\gamma, n_\mu) A_2(m, s_\alpha, s_\gamma, t_\alpha)(n_z, n_\mu) \delta(m = m_\gamma - m_\alpha + 1) \right. \\ &\quad - f_1 X_M^1(n_{z\gamma}, n_{z\alpha}, n_z) Y_{N^+}^1(-m_\alpha, m_\gamma)(n_\alpha, n_\gamma, n_\mu) A_2(m, s_\alpha, s_\gamma, t_\alpha)(n_z, n_\mu) \delta(m = m_\gamma - m_\alpha + 1) \\ &\quad + f_1 X_K^2(n_{z\alpha}, n_{z\gamma}, n_z) Y_{N^-}^2(-m_\alpha, m_\gamma)(n_\alpha, n_\gamma, n_\mu) B_2(m, s_\alpha, s_\gamma, t_\alpha)(n_z, n_\mu) \delta(m = m_\gamma - m_\alpha + 1) \\ &\quad \left. + f_1 X_M^1(n_{z\gamma}, n_{z\alpha}, n_z) Y_{N^-}^1(-m_\alpha, m_\gamma)(n_\alpha, n_\gamma, n_\mu) C_2(m, s_\alpha, s_\gamma, t_\alpha)(n_z, n_\mu) \delta(m = m_\gamma - m_\alpha - 1) \right] \end{aligned}$$

$$\begin{aligned}
& -f_1 X_M^1(n_{z\alpha}, n_{z\gamma}, n_z) Y_{N^-}^1(m_\gamma, -m_\alpha)(n_\gamma, n_\alpha, n_\mu) C_2(m, s_\alpha, s_\gamma, t_\alpha)(n_z, n_\mu) \delta(m = m_\gamma - m_\alpha - 1) \\
& + f_1 X_K^2(n_{z\alpha}, n_{z\gamma}, n_z) Y_{N^-}^2(-m_\alpha, m_\gamma)(n_\alpha, n_\gamma, n_\mu) D_2(m, s_\alpha, s_\gamma, t_\alpha)(n_z, n_\mu) \delta(m = m_\gamma - m_\alpha - 1) \\
& + f_2 X_K^1(n_{z\gamma}, n_{z\alpha}, n_z) \hat{Y}_{N^+}^1(-m_\alpha, m_\gamma)(n_\alpha, n_\gamma, n_\mu) E_2(m, s_\alpha, s_\gamma, t_\alpha)(n_z, n_\mu) \delta(m = m_\gamma - m_\alpha) \\
& - f_2 X_K^1(n_{z\gamma}, n_{z\alpha}, n_z) \hat{Y}_{N^+}^1(m_\gamma, -m_\alpha)(n_\gamma, n_\alpha, n_\mu) E_2(m, s_\alpha, s_\gamma, t_\alpha)(n_z, n_\mu) \delta(m = m_\gamma - m_\alpha) \\
& + f_2 X_K^1(n_{z\gamma}, n_{z\alpha}, n_z) \hat{Y}_{N^+}^2(-m_\alpha, m_\gamma)(n_\alpha, n_\gamma, n_\mu) F_2(m, s_\alpha, s_\gamma, t_\alpha)(n_z, n_\mu) \delta(m = m_\gamma - m_\alpha) \Big] , \tag{G.93}
\end{aligned}$$

and

$$\begin{aligned}
\tilde{\Delta}_{\alpha\beta} = & \delta_{t_\alpha t_\beta} \sum_{n_z n_\mu} \sum_m \left[f_1 X_M^1(n_{z\alpha}, n_{z\beta}, n_z) Y_{N^-}^2(-m_\alpha, -m_\beta)(n_\alpha, n_\beta, n_\mu) \tilde{A}_2(m, s_\alpha, s_\beta, t_\alpha)(n_z, n_\mu) \delta(m = m_\alpha + m_\beta - 1) \right. \\
& - f_1 X_M^2(n_{z\alpha}, n_{z\beta}, n_z) Y_{N^-}^2(-m_\alpha, -m_\beta)(n_\alpha, n_\beta, n_\mu) \tilde{B}_2(m, s_\alpha, s_\beta, t_\alpha)(n_z, n_\mu) \delta(m = m_\alpha + m_\beta - 1) \\
& + f_1 X_M^2(n_{z\alpha}, n_{z\beta}, n_z) Y_{N^-}^1(-m_\alpha, -m_\beta)(n_\alpha, n_\beta, n_\mu) \tilde{C}_2(m, s_\alpha, s_\beta, t_\alpha)(n_z, n_\mu) \delta(m = m_\alpha + m_\beta + 1) \\
& - f_1 X_M^1(n_{z\alpha}, n_{z\beta}, n_z) Y_{N^-}^2(-m_\alpha, -m_\beta)(n_\alpha, n_\beta, n_\mu) \tilde{D}_2(m, s_\alpha, s_\beta, t_\alpha)(n_z, n_\mu) \delta(m = m_\alpha + m_\beta + 1) \\
& + f_2 X_K^1(n_{z\alpha}, n_{z\beta}, n_z) Y_{N^+}^1(-m_\alpha, -m_\beta)(n_\alpha, n_\beta, n_\mu) \tilde{E}_2(m, s_\alpha, s_\beta, t_\alpha)(n_z, n_\mu) \delta(m = m_\alpha + m_\beta) \\
& \left. - f_2 X_K^1(n_{z\alpha}, n_{z\beta}, n_z) Y_{N^-}^1(-m_\alpha, -m_\beta)(n_\alpha, n_\beta, n_\mu) \tilde{E}_2(m, s_\alpha, s_\beta, t_\alpha)(n_z, n_\mu) \delta(m = m_\alpha + m_\beta) \right] , \tag{G.94}
\end{aligned}$$

eventually, pairing field is expressed as

$$\Delta_{\alpha\beta} = \frac{W_{LS}}{4} (\tilde{\Delta}_{\alpha\beta} - \tilde{\Delta}_{\beta\alpha}) . \tag{G.95}$$

With

$$f_1 \equiv (2\pi^3 \sqrt{2} b_z^2 b_r^3)^{-1} , \tag{G.96a}$$

$$f_2 \equiv (2\pi^3 \sqrt{2} b_z b_r^4)^{-1} . \tag{G.96b}$$

Bibliography

- [1] S. K. Bogner, R. J. Furnstahl, and A. Schwenk, “From low-momentum interactions to nuclear structure,” *Prog. Part. Nucl. Phys.*, vol. 65, p. 94, 2010.
- [2] H. Hergert, “A Guided Tour of ab initio Nuclear Many-Body Theory,” *Front. Phys.*, vol. 8, p. 379, 2020.
- [3] W. H. Dickhoff and C. Barbieri, “Self-consistent Green’s function method for nuclei and nuclear matter,” *Prog. Part. Nucl. Phys.*, vol. 52, p. 377, 2004.
- [4] V. Somà, T. Duguet, and C. Barbieri, “Ab initio self-consistent Gorkov-Green’s function calculations of semi-magic nuclei: Formalism at second order with a two-nucleon interaction,” *Phys. Rev. C*, vol. 84, p. 064317, 2011.
- [5] V. Somà, A. Cipollone, C. Barbieri, P. Navrátil, and T. Duguet, “Chiral two- and three-nucleon forces along medium-mass isotope chains,” *Phys. Rev. C*, vol. 89, p. 061301(R), 2014.
- [6] V. Somà, P. Navrátil, F. Raimondi, C. Barbieri, and T. Duguet, “Novel chiral Hamiltonian and observables in light and medium-mass nuclei,” *Phys. Rev. C*, vol. 101, p. 014318, 2020.
- [7] G. Hagen, T. Papenbrock, M. Hjorth-Jensen, and D. J. Dean, “Coupled-cluster computations of atomic nuclei,” *Rep. Prog. Phys.*, vol. 77, no. 9, p. 096302, 2014.
- [8] S. Binder, J. Langhammer, A. Calci, and R. Roth, “Ab initio path to heavy nuclei,” *Phys. Lett. B*, vol. 736, p. 119, 2014.
- [9] A. Signoracci, T. Duguet, G. Hagen, and G. Jansen, “Ab initio Bogoliubov coupled cluster theory for open-shell nuclei,” *Phys. Rev. C*, vol. 91, no. 6, p. 064320, 2015.
- [10] S. J. Novario, G. Hagen, G. R. Jansen, and T. Papenbrock, “Charge radii of exotic neon and magnesium isotopes,” *Phys. Rev. C*, vol. 102, p. 051303(R), Nov 2020.
- [11] G. Hagen, S. J. Novario, Z. H. Sun, T. Papenbrock, G. R. Jansen, J. G. Lietz, T. Duguet, and A. Tichai, “Angular-momentum projection in coupled-cluster theory: Structure of ^{34}Mg ,” *Phys. Rev. C*, vol. 105, p. 064311, Jun 2022.
- [12] A. Tichai, P. Demol, and T. Duguet, “Towards heavy-mass ab initio nuclear structure: Open-shell Ca, Ni and Sn isotopes from Bogoliubov coupled-cluster theory,” *Phys. Lett. B*, vol. 851, p. 138571, 2024.
- [13] J. D. Holt, J. Menéndez, J. Simonis, and A. Schwenk, “Three-nucleon forces and spectroscopy of neutron-rich calcium isotopes,” *Phys. Rev. C*, vol. 90, p. 024312, 2014.
- [14] A. Tichai, J. Langhammer, S. Binder, and R. Roth, “Hartree-Fock many-body perturbation theory for nuclear ground-states,” *Phys. Lett. B*, vol. 756, p. 283, 2016.

- [15] B. S. Hu, F. R. Xu, Z. H. Sun, J. P. Vary, and T. Li, “Ab initio nuclear many-body perturbation calculations in the hartree-fock basis,” *Phys. Rev. C*, vol. 94, p. 014303, Jul 2016.
- [16] A. Tichai, E. Gebrerufael, K. Vobig, and R. Roth, “Open-shell nuclei from no-core shell model with perturbative improvement,” *Phys. Lett. B*, vol. 786, pp. 448–452, 2018.
- [17] A. Tichai, P. Arthuis, T. Duguet, H. Hergert, V. Somà, and R. Roth, “Bogoliubov many-body perturbation theory for open-shell nuclei,” *Phys. Lett. B*, vol. 786, p. 195, 2018.
- [18] P. Arthuis, T. Duguet, A. Tichai, R. D. Lasserri, and J. P. Ebran, “ADG: Automated generation and evaluation of many-body diagrams I. Bogoliubov many-body perturbation theory,” *Comput. Phys. Commun.*, vol. 240, pp. 202–227, 2019.
- [19] P. Demol, M. Frosini, A. Tichai, V. Somà, and T. Duguet, “Bogoliubov many-body perturbation theory under constraint,” *Ann Phys (N Y)*, vol. 424, p. 168358, 2021.
- [20] A. Tichai, R. Roth, and T. Duguet, “Many-Body Perturbation Theories for Finite Nuclei,” *Front. Phys.*, vol. 8, p. 164, 2020.
- [21] M. Frosini, T. Duguet, J. P. Ebran, and V. Somà, “Multi-reference many-body perturbation theory for nuclei,” *Eur. Phys. J. A*, vol. 58, no. 4, p. 62, 2022.
- [22] P. Demol, T. Duguet, and A. Tichai, “Ab initio Bogoliubov many-body perturbation theory: closed-form constraint on the average particle number,” 7 2024.
- [23] K. Tsukiyama, S. K. Bogner, and A. Schwenk, “In-medium Similarity Renormalization Group for Nuclei,” *Phys. Rev. Lett.*, vol. 106, p. 222502, 2011.
- [24] K. Tsukiyama, S. K. Bogner, and A. Schwenk, “In-medium similarity renormalization group for open-shell nuclei,” *Phys. Rev. C*, vol. 85, p. 061304(R), 2012.
- [25] H. Hergert, S. Binder, A. Calci, J. Langhammer, and R. Roth, “Ab Initio Calculations of Even Oxygen Isotopes with Chiral Two-Plus-Three-Nucleon Interactions,” *Phys. Rev. Lett.*, vol. 110, p. 242501, 2013.
- [26] H. Hergert, S. K. Bogner, T. D. Morris, A. Schwenk, and K. Tsukiyama, “The In-Medium Similarity Renormalization Group: A Novel Ab Initio Method for Nuclei,” *Phys. Rep.*, vol. 621, p. 165, 2016.
- [27] S. R. Stroberg, H. Hergert, S. K. Bogner, and J. D. Holt, “Nonempirical Interactions for the Nuclear Shell Model: An Update,” *Annu. Rev. Nucl. Part. Sci.*, vol. 69, no. 1, p. 307, 2019.
- [28] M. Heinz, A. Tichai, J. Hoppe, K. Hebeler, and A. Schwenk, “In-medium similarity renormalization group with three-body operators,” *Phys. Rev. C*, vol. 103, p. 044318, Apr 2021.
- [29] S. R. Stroberg, J. D. Holt, A. Schwenk, and J. Simonis, “Ab initio limits of atomic nuclei,” *Phys. Rev. Lett.*, vol. 126, p. 022501, Jan 2021.
- [30] A. Tichai, P. Arthuis, H. Hergert, and T. Duguet, “Adg: automated generation and evaluation of many-body diagrams - iii. bogoliubov in-medium similarity renormalization group formalism,” *Eur. Phys. J. A*, vol. 58, no. 1, p. 2, 2022.
- [31] M. Frosini, T. Duguet, J.-P. Ebran, B. Bally, T. Mongelli, T. R. Rodríguez, R. Roth, and V. Somà, “Multi-reference many-body perturbation theory for nuclei: II. Ab initio study of neon isotopes via PGCM and IM-NCSM calculations,” *Eur. Phys. J. A*, vol. 58, no. 4, p. 63, 2022.

- [32] M. Frosini, T. Duguet, J.-P. Ebran, B. Bally, H. Hergert, T. R. Rodríguez, R. Roth, J. Yao, and V. Somà, “Multi-reference many-body perturbation theory for nuclei: III. Ab initio calculations at second order in PGCM-PT,” *Eur. Phys. J. A*, vol. 58, no. 4, p. 64, 2022.
- [33] P. Ring and P. Schuck, *The Nuclear Many-Body Problems*, vol. 103. Springer Verlag, 01 1980.
- [34] M. Bender, P.-H. Heenen, and P.-G. Reinhard, “Self-consistent mean-field models for nuclear structure,” *Rev. Mod. Phys.*, vol. 75, pp. 121–180, 2003.
- [35] T. Nikšić, D. Vretenar, and P. Ring, “Relativistic Nuclear Energy Density Functionals: Mean-Field and Beyond,” *Prog. Part. Nucl. Phys.*, vol. 66, pp. 519–548, 2011.
- [36] L. Robledo, T. Rodríguez, and R. Rodríguez-Guzmán, “Mean field and beyond description of nuclear structure with the Gogny force: A review,” *J. Phys. G*, vol. 46, no. 1, p. 013001, 2019.
- [37] Z.-C. Gao, M. Horoi, and Y. Chen, “Variation after projection with a triaxially deformed nuclear mean field,” *Phys. Rev. C*, vol. 92, no. 6, p. 064310, 2015.
- [38] C. Jiao, J. Engel, and J. Holt, “Neutrinoless double-beta decay matrix elements in large shell-model spaces with the generator-coordinate method,” *Phys. Rev. C*, vol. 96, no. 5, p. 054310, 2017.
- [39] B. Bally, A. Sánchez-Fernández, and T. Rodríguez, “Variational approximations to exact solutions in shell-model valence spaces: calcium isotopes in the pf-shell,” *Phys. Rev. C*, vol. 100, no. 4, p. 044308, 2019.
- [40] N. Shimizu, T. Mizusaki, K. Kaneko, and Y. Tsunoda, “Generator-coordinate methods with symmetry-restored Hartree-Fock-Bogoliubov wave functions for large-scale shell-model calculations,” *Phys. Rev. C*, vol. 103, no. 6, p. 064302, 2021.
- [41] A. Sánchez-Fernández, B. Bally, and T. R. Rodríguez, “Variational approximations to exact solutions in shell-model valence spaces: Systematic calculations in the sd shell,” *Phys. Rev. C*, vol. 104, no. 5, p. 054306, 2021.
- [42] J. M. Yao, B. Bally, J. Engel, R. Wirth, T. R. Rodríguez, and H. Hergert, “AbInitio Treatment of Collective Correlations and the Neutrinoless Double Beta Decay of ^{48}Ca ,” *Phys. Rev. Lett.*, vol. 124, no. 23, p. 232501, 2020.
- [43] A. Belley *et al.*, “Ab initio Uncertainty Quantification of Neutrinoless Double-Beta Decay in $\text{Ge}76$,” *Phys. Rev. Lett.*, vol. 132, no. 18, p. 182502, 2024.
- [44] A. Porro, T. Duguet, J.-P. Ebran, M. Frosini, R. Roth, and V. Somà, “Ab initio description of monopole resonances in light- and medium-mass nuclei: I. Technical aspects and uncertainties of ab initio PGCM calculations,” *Eur. Phys. J. A*, vol. 60, no. 6, p. 133, 2024.
- [45] A. Porro, T. Duguet, J.-P. Ebran, M. Frosini, R. Roth, and V. Somà, “Ab initio description of monopole resonances in light- and medium-mass nuclei: II. Ab initio PGCM calculations in ^{46}Ti , ^{28}Si and ^{24}Mg ,” *Eur. Phys. J. A*, vol. 60, no. 6, p. 134, 2024.
- [46] A. Porro, T. Duguet, J.-P. Ebran, M. Frosini, R. Roth, and V. Somà, “Ab initio description of monopole resonances in light- and medium-mass nuclei: III. Moments evaluation in ab initio PGCM calculations,” 4 2024.
- [47] M. Frosini, T. Duguet, J.-P. Ebran, and V. Somà, “Multi-reference many-body perturbation theory for nuclei: I. novel pgcm-pt formalism,” *The European Physical Journal A*, vol. 58, no. 4, p. 62, 2022.

- [48] M. Frosini, T. Duguet, J.-P. Ebran, B. Bally, H. Hergert, T. R. Rodríguez, R. Roth, J. Yao, and V. Soma, “Multi-reference many-body perturbation theory for nuclei: Iii. ab initio calculations at second order in pgcm-pt,” *The European Physical Journal A*, vol. 58, no. 4, p. 64, 2022.
- [49] M. Frosini, T. Duguet, J.-P. Ebran, B. Bally, T. Mongelli, T. R. Rodríguez, R. Roth, and V. Somà, “Multi-reference many-body perturbation theory for nuclei,” *The European Physical Journal A*, vol. 58, apr 2022.
- [50] A. Sarkar and D. Lee, “Convergence of eigenvector continuation,” *Physical Review Letters*, vol. 126, 2020.
- [51] D. Frame, *Ab Initio simulation of light nuclear systems using Eigenvector Continuation and auxiliary field Monte Carlo*. PhD thesis, Michigan State University, 2019.
- [52] T. Duguet, A. Ekström, R. J. Furnstahl, S. König, and D. Lee, “Colloquium: Eigenvector continuation and projection-based emulators,” *Reviews of Modern Physics*, vol. 96, Aug. 2024.
- [53] A. Ekström and G. Hagen, “Global sensitivity analysis of bulk properties of an atomic nucleus,” *Phys. Rev. Lett.*, vol. 123, no. 25, p. 252501, 2019.
- [54] P. Demol, T. Duguet, A. Ekström, M. Frosini, K. Hebeler, S. König, D. Lee, A. Schwenk, V. Somà, and A. Tichai, “Improved many-body expansions from eigenvector continuation,” *Phys. Rev. C*, vol. 101, no. 4, p. 041302, 2020.
- [55] S. König, A. Ekström, K. Hebeler, D. Lee, and A. Schwenk, “Eigenvector Continuation as an Efficient and Accurate Emulator for Uncertainty Quantification,” *Phys. Lett. B*, vol. 810, p. 135814, 2020.
- [56] C. Drischler, M. Quinonez, P. G. Giuliani, A. E. Lovell, and F. M. Nunes, “Toward emulating nuclear reactions using eigenvector continuation,” *Phys. Lett. B*, vol. 823, p. 136777, 2021.
- [57] J. A. Melendez, C. Drischler, A. J. Garcia, R. J. Furnstahl, and X. Zhang, “Fast & accurate emulation of two-body scattering observables without wave functions,” *Phys. Lett. B*, vol. 821, p. 136608, 2021.
- [58] X. Zhang and R. J. Furnstahl, “Fast emulation of quantum three-body scattering,” *Phys. Rev. C*, vol. 105, no. 6, p. 064004, 2022.
- [59] M. C. Franzke, A. Tichai, K. Hebeler, and A. Schwenk, “Excited states from eigenvector continuation: The anharmonic oscillator,” *Phys. Lett. B*, vol. 830, p. 137101, 2022.
- [60] N. Yapa and S. König, “Volume extrapolation via eigenvector continuation,” *Phys. Rev. C*, vol. 106, no. 1, p. 014309, 2022.
- [61] N. Yapa, K. Fosse, and S. König, “Eigenvector continuation for emulating and extrapolating two-body resonances,” *Phys. Rev. C*, vol. 107, no. 6, p. 064316, 2023.
- [62] Q. Y. Luo, X. Zhang, L. H. Chen, and J. M. Yao, “Emulating the generator coordinate method with extended eigenvector continuation for the Lipkin-Meshkov-Glick model,” *Phys. Rev. C*, vol. 110, no. 1, p. 014309, 2024.
- [63] X. Zhang, C. C. Wang, C. R. Ding, and J. M. Yao, “Subspace-projected multireference covariant density functional theory,” 2024.
- [64] D. J. Thouless *Annals of Physics*, vol. 10, no. 4, pp. 553–588, 1960.

- [65] L. M. Robledo, “The sign of the overlap of HFB wave functions,” *Phys. Rev.*, vol. C79, p. 021302, 2009.
- [66] B. Bally and T. Duguet, “Norm overlap between many-body states: Uncorrelated overlap between arbitrary Bogoliubov product states,” *Phys. Rev. C*, vol. 97, no. 2, p. 024304, 2018.
- [67] R. Balian and E. Brezin, “Nonunitary bogoliubov transformations and extension of wick’s theorem,” *Il Nuovo Cimento B (1965-1970)*, vol. 64, no. 1, pp. 37–55, 1969.
- [68] A. Porro and T. Duguet, “On the off-diagonal wick’s theorem and onishi formula: Alternative and consistent approach to off-diagonal operator and norm kernels,” *The European Physical Journal A*, vol. 58, no. 10, p. 197, 2022.
- [69] A. Sarkar, *Eigenvector Continuation: convergence and emulators*. PhD thesis, Michigan State University, 2022.
- [70] Y. Lafranche, “Documentation of the fig4tex macro package.” <https://perso.univ-rennes1.fr/yvon.lafranche/fig4tex/>.
- [71] M. Beiner and al, “Nuclear ground-state properties and self-consistent calculations with the skyrme interaction (i),” *Nucl. Phys. A*, vol. 238.1, p. 29, 1975.
- [72] J. Dechargé and G. D., “Hartree-fock-bogolyubov calculations with the dl effective interaction on spherical nuclei,” *Phys. Rev. C*, vol. 21, pp. 1568–1593, 1980.
- [73] D. Lacroix, T. Duguet, and M. Bender, “Configuration Mixing within the Energy Density Functional Formalism: Removing Spurious Contributions from Non-Diagonal Energy Kernels,” *Phys. Rev. C*, vol. 79, p. 044318, 2009.
- [74] M. Bender, T. Duguet, and D. Lacroix, “Particle-Number Restoration within the Energy Density Functional Formalism,” *Phys. Rev. C*, vol. 79, p. 044319, 2009.
- [75] T. Duguet, M. Bender, K. Bennaceur, D. Lacroix, and T. Lesinski, “Particle-Number Restoration within the Energy Density Functional formalism: Are terms depending on non-integer powers of the density matrices viable?,” *Phys. Rev. C*, vol. 79, p. 044320, 2009.
- [76] D. Brink and E. Boeker, “Effective interaction for hartree-fock calculations,” *Nuclear Physics*, vol. A91, 1967.
- [77] N. Schunck *et al.*, *Energy density functional methods for atomic nuclei*. IOP, 2019.
- [78] W. Younes, D. Gogny, and J.-F. Berger, *A Microscopic Theory of Fission Dynamics Based on the Generator Coordinates Methods*. Springer, 2019.
- [79] W. Younes, “Gaussian matrix elements in a cylindrical harmonic oscillator basis,” *Computer Physics Communications*, vol. 180, pp. 1013–1040, 2009.
- [80] P. Descourt and S. Peru, “Calcul des éléments de matrices de la force de gogny dans la base de l’oscillateur harmonique en symétrie axiale.” private communication.
- [81] J. Talman, “Some properties of three-dimensional hamonic oscillator wave functions,” *Nuclear Physics A*, vol. 141, pp. 273–288, 1970.
- [82] W.-L. Loh, “On latin hypercube sampling,” *The annals of statistics*, vol. 24, pp. 2058–2080, 1996.

- [83] J. Helton and F. Davies, "Latin hypercube sampling and the propagation of uncertainty in analyses of complex system," *Sandia report*, 2002.
- [84] A. Sarkar and D. Lee, "Self-learning emulators and eigenvector continuation," *Phys. Rev. Res.*, vol. 4, no. 2, p. 023214, 2022.
- [85] M. C. Franzke, A. Tichai, K. Hebler, and A. Schwenk, "Eigenvector continuation for the pairing Hamiltonian," *Phys. Rev. C*, vol. 109, no. 2, p. 024311, 2024.
- [86] J. Dieudonné, *Eléments d'analyse I, fondements de l'analyse moderne*. Gauthier-Villars, 1990.
- [87] T. Bendokat, R. Zimmermann, and P. Absil, "A grassmann manifold handbook: basic geometry and computational aspects," *Advances in Computational Mathematics*, vol. 50, no. 6, 2024.
- [88] J. Dieudonné, *Eléments d'analyse III*. Gauthier-Villars, 1980.
- [89] K. Ye and L.-H. Lim, "Schubert varieties and distances between subspaces of different dimensions," *SIAM Journal on Matrix Analysis and Applications*, vol. 37, no. 3, pp. 1176–1197, 2016.
- [90] Y.-C. Wong, "Differential geometry of grassmann manifolds," *Proceedings of the National Academy of Sciences (PNAS)*, vol. 57, no. 3, 1967.
- [91] J. Pearson, "Computation of hypergeometric functions," Master's thesis, University of Oxford, 2009.
- [92] J. Egido, L. Robledo, and R. Chasman, "Nuclear shapes in ^{176}w with density dependent forces: from ground state to fission," *Physics Letters B*, vol. 393, p. 13, 1997.
- [93] R. Navarro Perez, N. Schunck, R.-D. Lasserri, C. Zhang, and J. Sarich, "Axially deformed solution of the skyrme-hartree-fock-bogolyubov equations using the transformed harmonic oscillator basis (iii)," *Computer Physics Communications*, vol. 220, pp. 363–375, 2017.